ALMA MATER STUDIORUM
UNIVERSITÀ DI BOLOGNA

DEPARTMENT OF INDUSTRIAL ENGINEERING - DIN

Second Cycle Master's Degree in
AEROSPACE ENGINEERING (LM-20)
Curriculum Space

# Analytical tool development for sound directivity simulation and control in a multicopter configuration

Dissertation in APPLIED AERODYNAMICS

DEFENDED BY:
**ALDO CHELLA**

SUPERVISOR:
**PROF. GABRIELE BELLANI**

CO-SUPERVISORS:
**DR. ING. THORSTEN SCHWARZ**

**DR. ING. JURRIEN OLSMAN**

---

**Graduation Session of March 2025**
**Academic Year 2023/24**

In collaboration with:


**DLR - German Aerospace Center**

*Institute of Aerodynamics and Flow Technology - Helicopter Department*

Braunschweig, Germany

*A mamma e papà*

# Acknowledgments

I would like to express my gratitude to the Helicopter Department at DLR in Braunschweig for the incredible opportunity to complete my internship and thesis with their team. In particular, I would like to thank Dr. Thorsten Schwarz and Dr. Jurrien Olsman for their constant support throughout the six months I spent there.

I am deeply grateful to my colleagues and friends, Francesco Sessini and Diego Donnini, for sharing this experience with me and for their help and motivation during this period. I would also like to thank my supervisor, Professor Gabriele Bellani, for his support with the project and the thesis writing. A very special thank you goes to the Templari and all my friends in Forlì, who shared every day of the last seven years with me. These years will always be cherished as the best memories of my life.

Of course, I must thank my friends from Torre. We have shared our entire lives together, and even though we are now far apart, I know I can always count on them.

The most special thank you goes to my family: my parents, who have always supported me in every decision I have made and who have always believed in me; and my brother, cousins, and uncles, who have always been there for me. Everything I do is to make them proud.

# Abstract

This thesis explores the development of fast simulation software for predicting the sound directivity of multirotor aircraft in hover. The software utilizes simplified analytical formulations derived from the Ffowcs-Williams-Hawkings (FW-H) aeroacoustic equations. A key simplification involves representing each rotor blade's sound emission as a single point source rather than a distributed source. This approach enables rapid predictions of sound directivity for various multirotor configurations and rotor phase shifts. The software is validated against results from a NASA publication and simulations conducted by APSIM (software to predict rotor and propeller noise by DLR).

In the final stage of the research, the simulation software is combined with a genetic algorithm to optimize rotor phasing. Rotor phasing refers to the relative timing of each rotor's rotation, which affects the resulting sound field. The objective is to determine the optimal phase relationship between rotors to minimize noise in a specific target direction, such as downward noise toward people or away from sensitive equipment. A genetic algorithm, inspired by the principles of natural selection, is used to explore potential phasing configurations. By using the simulation's rapid predictions, the algorithm efficiently identifies the rotor configuration that achieves the desired noise reduction.

# Contents

# List of Figures

# 1 Introduction

## 1.1 Overview of Urban Air Mobility and eVTOL

There has been increasing interest in the concept of Urban Air Mobility in the last few years. This futuristic new paradigm of transportation within cities promises to be an alternative to classical transport systems and a solution to traffic congestion. In particular, the design that has gathered the most attention for these purposes is the eVTOL (electric vertical take-off and landing), an electric vehicle that, in most of the cases, employs a variable number of rotors to generate lift. One of the most famous eVTOLs is the one developed by the German company Volocopter, which was also selected for experimental use during the Winter Olympic Games of Milano-Cortina in 2026. The Urban Air Mobility (UAM) market, though still in its early stages, is forecasted to experience unprecedented growth. According to a study by South Korea's Ministry of Land, Infrastructure and Transport, the global UAM sector is projected to surge from $10.9 billion in 2025 to $250.6 billion by 2035, with further expansion reaching $609 billion by 2040. The UAM market extends far beyond aircraft manufacturing, encompassing essential infrastructure such as air traffic control systems, landing hubs, and passenger boarding facilities. Aircraft themselves represent just 15% of the UAM value chain. The real growth lies in infrastructure and traffic management systems, not merely building vehicles. This highlights a strategic industry shift, with companies increasingly investing in the digital and physical frameworks required to enable safe, efficient urban air transportation rather than focusing exclusively on vehicle production.

## 1.2 UAM and eVTOL Aircraft Designs

In recent years, a multitude of new companies have conceptualized their own versions of eVTOLs, particularly for the purpose of intercity connections. One of the major difficulties is obtaining certification for these types of vehicles, especially given that they are intended to fly over crowded and residential areas. Notable is the design choice for the Volocopter eVTOL, which has 18 rotors, primarily for efficiency reasons but also for redundancy.

The UAM landscape is diverse, featuring various eVTOL aircraft designs categorized by propulsion and flight mechanics. The main design cathegories nowadays are:

- **Multicopters**: These designs feature multiple rotors, typically four or more, and are known for their vertical take-off and landing capabilities. Multicopters prioritize vertical flight, offering simplicity and redundancy but face challenges in transitioning to horizontal flight.
- **Lift + Cruise**: These designs combine vertical and horizontal flight capabilities, with lift rotors for vertical take-off and landing and cruise propellers for forward flight. This configuration balances

efficiency and performance, enabling longer flight ranges and higher speeds.

- **Rotorcraft**: These designs are based on traditional helicopter configurations, with one or more rotors providing lift and propulsion. Rotorcraft designs offer simplicity and stability but face challenges in efficiency and noise reduction.
- **Vectored Thrust**: These designs feature rotors or propellers that can tilt or rotate to provide vertical and horizontal thrust. Vectored thrust configurations offer efficiency but face design and certification complexities.

**(a)** LIFT Hexa (multicopter)[1]

**(b)** Beta Alia (Lift + Cruise)[2]

**(c)** Jaunt (rotorcraft)[3]


**(d)** Vertical VX4 (vectored thrust)[4]

**Figure 1.1.** Examples of common eVTOL aircraft designs for UAM applications

Despite this diversity, a consensus on optimal designs and business models is lacking, highlighting ongoing challenges in battery technology, regulation, and market validation.

Aircraft technology research is heavily invested in propulsion systems, particularly electric propulsion, due to its noise and emission reduction potential. Other key areas include battery technology, electric propulsion architectures, and hybrid systems. Aerodynamic optimization for eVTOLs in urban environments and noise reduction design are also critical. Autonomy and flight control systems are also being developed to ensure safe and reliable UAM operations, even though research in these fields and in acoustics is comparatively less extensive than in propulsion and aircraft design.

Market and operations research focuses on the practical viability of UAM. Air traffic management studies address integrating UAM into existing airspace, while vertiport infrastructure research explores optimal locations and designs. Demand modeling and market analysis seek to understand user preferences and economic viability, drawing parallels with helicopter taxi services and ground transportation.

## 1.3 Urban Air Mobility Infrastructure Integration

Urban Air Mobility (UAM) systems necessitate comprehensive and strategic infrastructure integration across multiple interdependent domains, which presents both opportunities and challenges for successful implementation within existing urban environments. The strategic positioning of vertiports constitutes a fundamental decision point in UAM network design, requiring sophisticated optimization methodologies that simultaneously account for population density distributions, established commuter patterns, and various operational constraints that may limit viable locations. These crucial facilities must effectively balance public accessibility with community acceptance concerns, particularly regarding noise emissions, while maintaining strict adherence to complex airspace regulations and restrictions.

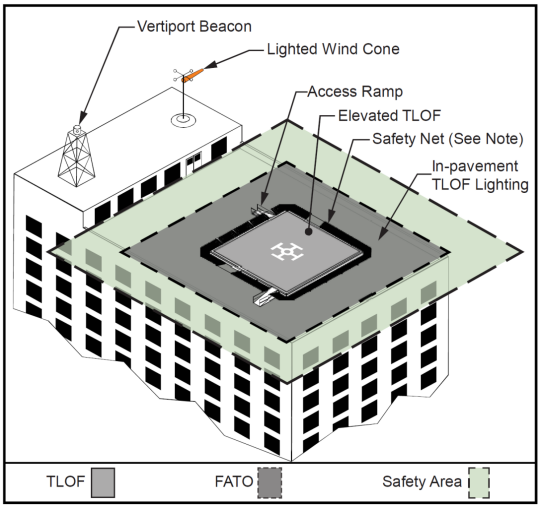


**Figure 1.2.** Vertiport design concept

The structural and operational configurations of vertiports—whether implemented as linear, satellite, or pier arrangements—directly influence the overall operational capacity and efficiency of the UAM network through their impact on aircraft throughput and passenger processing capabilities. Although existing heliport design guidelines provide valuable foundational principles for approach paths and obstacle clearance requirements, the unique operational characteristics of UAM present novel challenges that may necessitate the development of segregated airspace corridors to ensure safe integration with conventional air traffic systems, particularly in proximity to major airport facilities.

Energy infrastructure represents perhaps the most significant technical challenge for electric Vertical Take-Off and Landing (eVTOL) aircraft deployment, as these advanced aerial vehicles face substantial operational constraints stemming from current battery technology limitations. These constraints manifest through multiple interrelated factors: the fundamental trade-offs between range capability and aircraft weight/cost considerations; the significant implications of charging duration on overall fleet utilization rates, especially during peak demand periods; and the potentially overwhelming collective power demands

that a fully operational UAM fleet would impose on existing urban electrical grid infrastructure, which may require substantial capacity upgrades at considerable expense.

Valuable insights can be derived from examining parallels in electric and autonomous vehicle research, where extensive studies have demonstrated that strategic charging infrastructure placement and seamless grid integration represent critical success factors for widespread adoption. The competitive advantage of UAM transportation may prove most pronounced in densely developed urban centers characterized by limited parking availability and high associated costs, precisely the environments where conventional transportation modes face their greatest efficiency challenges.

A comprehensive systems-engineering approach employing high-fidelity simulation models represents an essential methodology for optimizing the complex interdependencies between vertiport infrastructure deployment, airspace integration protocols, energy distribution systems, and user behavior patterns, thereby ensuring that UAM development aligns harmoniously with broader transportation planning objectives while addressing sustainability considerations and regulatory requirements.

## 1.4 Urban Air Mobility Noise

A significant problem of this new kind of transport system is the sound emitted by swarms of aircraft flying over the skies of a city. Noise is a significant impediment to UAM adoption considering that community acceptance of aircraft noise is a critical constraint, necessitating research into noise mitigation. Key areas of noise research include developing appropriate noise metrics, identifying and reducing eVTOL noise sources, designing noise-optimized operational procedures, and integrating noise considerations into urban planning. Addressing these research directions is vital for UAM's public acceptance and operational success.

### 1.4.1 Sources

The principal noise sources in VTOLs are related to the rotors. While studying the noise emitted by this kind of vehicles in fact we consider only the noise emitted by the rotation of the blades because all the other possible sources of noise will be overwhelmed by these.

Rotor harmonic noise, primarily from the main and tail rotors, is the dominant component of a helicopter's external acoustic signature. This noise is categorized into lower harmonic noise, which occurs continuously across flight regimes, and impulsive noise, which manifests under specific conditions but overshadows other sources when present.

#### 1.4.1.1 Lower Harmonic Noise

Lower harmonic noise arises from two key mechanisms: loading noise and thickness noise.

- Loading noise results from the lift forces on the blades, creating pressure fluctuations at the blade passing frequency and its harmonics. For many helicopters, the first few harmonics may be below 20 Hz, contributing more to vibrations than audible noise, while higher harmonics are less intense and noticeable only without dominant impulsive noise. It propagates mainly downwards, affecting ground-level observers.
- Thickness noise is caused by air displacement as rotor blades move, peaking near the blade tips where the speed is highest. It produces low-frequency pulses at the blade passing frequency and is

more noticeable to observers at the same height as the rotor, spreading horizontally. When blade tip speeds enter the transonic range, it can intensify into high-speed impulsive (HSI) noise, but modern designs with lower tip speeds and thinner blades help reduce this.

#### 1.4.1.2 Impulsive Noise

Impulsive noise, marked by its abrupt intensity, includes high-speed impulsive (HSI) noise and blade-vortex interaction (BVI) noise:

- HSI noise emerges from thickness noise in transonic conditions, with local shocks forming near blade tips. It is directional and depends on blade geometry and flow. Optimized blade profiles and reduced tip speeds in modern helicopters mitigate its impact.
- BVI noise occurs when blades encounter tip vortices from preceding blades, common during shallow descents like landing approaches. These interactions cause rapid airload changes, producing intense, impulsive sound. Its prominence in approach paths makes it critical for noise abatement near heliports.

#### 1.4.1.3 Tail Rotor Harmonic Noise

Tail rotor noise, similar to main rotor noise, features higher frequencies due to rotational speeds six to seven times greater than the main rotor. As we can see from a frequency spectrum of helicopter noise, the main rotor noise has the loudest components at lower frequencies while the main rotor impulsive noise and the tail rotor noise are peaking at higher frequencies but with lower intensity compared to the former.

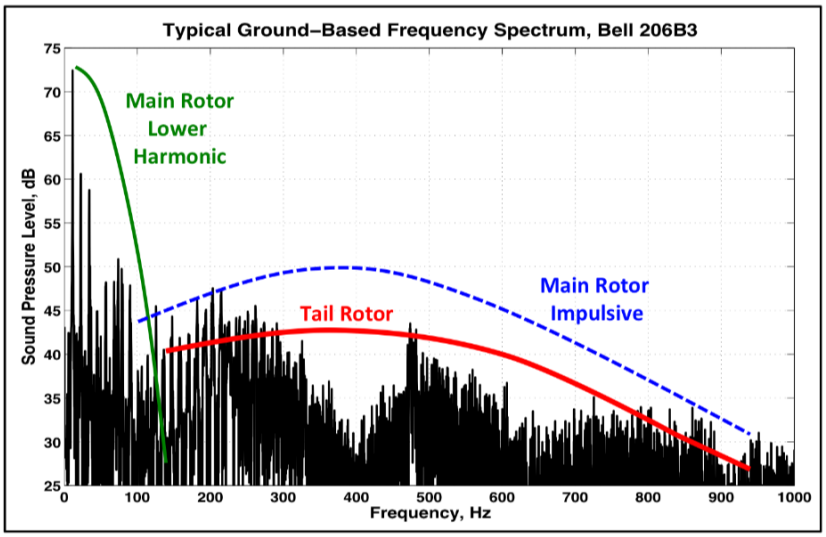


**Figure 1.3.** Typical ground-based frequency spectrum of the Bell 206B3 helicopter, showing sound pressure level (dB) versus frequency (Hz). The green line denotes the main rotor lower harmonic, the red line the tail rotor, and the blue dashed line the main rotor impulsive noise.[5]

But, while the main rotor's lower harmonic noise has the highest sound pressure levels, its low frequency (below 100 Hz) may be less perceptible to the human ear compared to the mid-frequency peaks (400–500 Hz) from the tail rotor and impulsive noise. Human hearing is most sensitive between 1,000 and 4,000 Hz, but within this graph's range (up to 1,000 Hz), the 400–500 Hz range is still significant for perceived loudness and annoyance.

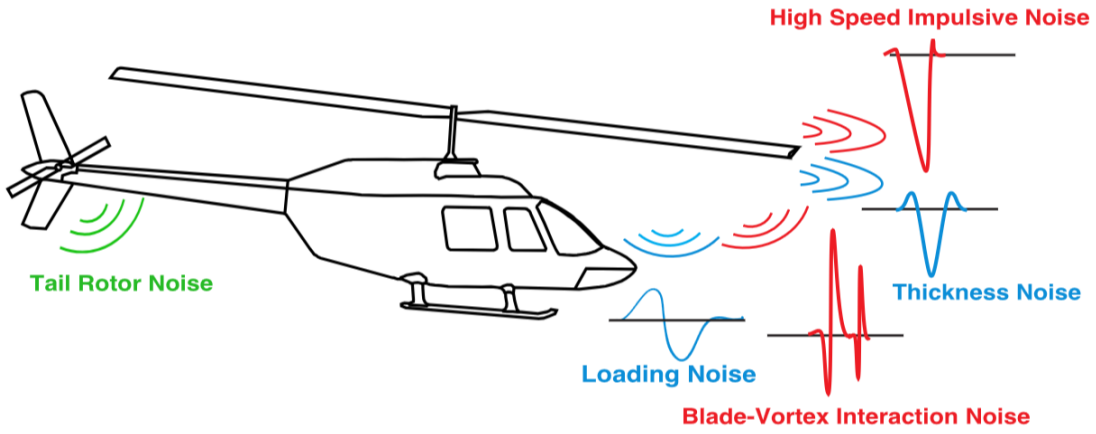


**Figure 1.4.** Helicopter noise sources. It highlights the distinct shapes of pressure fluctuations for thickness and loading noise, as well as their different propagation directions: in the rotor plane for thickness noise and out-of-plane, primarily below the rotor, for loading noise.[5]

#### 1.4.1.4 Rotor Broadband Noise

Beyond the primary rotor harmonic noise, several significant non-harmonic noise sources exist in rotorcraft systems. These sources produce acoustic signatures that do not correlate with the blade passage frequency. The rotor generates broadband noise across mid to high frequencies due to random aerodynamic interactions with the blades. These interactions stem from:

- Boundary layer turbulence
- Vortex shedding phenomena
- Flow separation events
- Re-ingestion of rotor wake
- Atmospheric turbulence

Though this noise source is ever-present, it typically becomes noticeable only in operating regions where the other rotor noise sources are not dominant. While generally not dominant in conventional helicopter operations, rotor broadband noise becomes particularly significant in specialized configurations with high thrust and low tip speeds—characteristic of small unmanned vehicles and wind turbines.

### 1.4.2 Noise Sources Mathematical Modeling

Usually, when it's needed to study the sound emission from an helicopter or a multirotor, we are going to model only the rotor harmonic noise sources, since they are the dominant noise sources. One common way to model rotor harmonic noise sources is with the Ffowcs Williams – Hawkings (FW-H) equation, which describes exactly how noise is generated by arbitrary surfaces in motion through a medium. An in-depth discussion about that will be done later in this work but here we can give a short overview. The Ffowcs Williams-Hawkings (FW-H) equation is a cornerstone of aeroacoustics, enabling the prediction of noise generated by moving bodies such as helicopter rotors. This equation decomposes the acoustic

pressure perturbation into three physically distinct terms: monopole, dipole, and quadrupole. Each term corresponds to a specific noise generation mechanism. The FW-H equation is expressed as:

$$
\begin{aligned}
p'(x,t) = & \underbrace{\frac{1}{4\pi}\frac{\partial}{\partial t}\int_S \left[\frac{\rho_0 v_n}{r|1-M_r|}\right]_\tau dS}_{\text{monopole}} \\
& \underbrace{-\frac{1}{4\pi}\frac{\partial}{\partial x_i}\int_S \left[\frac{P_{ij}n_j}{r|1-M_r|}\right]_\tau dS}_{\text{dipole}} \\
& \underbrace{+\frac{1}{4\pi}\frac{\partial^2}{\partial x_i \partial x_j}\int_V \left[\frac{Q_{ij}}{r|1-M_r|}\right]_\tau dV}_{\text{quadrupole}},
\end{aligned}
\tag{1.1}
$$

These terms model distinct noise sources:

- The monopole term represents thickness noise. It can be interpreted as a distribution of mass sources and sinks across the blade surface, capturing the volume displacement effect.
- The dipole term accounts for loading noise, including blade-vortex interaction (BVI). This is represented as dipole sources distributed over the blade surface.
- The quadrupole term captures the effects of complex noise sources within the fluid volume surrounding the rotor, such as those in transonic flow fields responsible for high-speed impulsive (HSI) noise.

HSI noise is not a significant factor due to the absence of transonic flow effects typically associated with high-speed rotor tips. Consequently, the quadrupole term is neglected, and the analysis focuses solely on the monopole and dipole terms, which adequately describe thickness and loading noise, respectively.

By retaining only the monopole and dipole terms, we can ensure an efficient yet accurate representation of the primary noise generation mechanisms.

### 1.4.3 Propagation

The sound propagation of UAM vechicles is not different from other kind of noise sources. However we should consider that these kind of vehicles are going to operate inside cities and at low altitudes, so it will important also to consider the refelctions of acoustic waves on buildings and on the ground. In the picture below the paths of the sound waves are represented as straight lines. This is an approximation because they will be curved in a real atmosphere and other factors also will contribute to make the problem even more complex. In fact local wind and atmospheric conditions in an urban setting affect not only UAM flight performance, but also sound propagation. But even with the approximations mentioned before the problem is still very complex due to phenomena of refraction, diffraction, and multiple reflections by building facades which represent complications in accurately predicting aircraft noise propagation. We can find in the literaure several studies that try to model the sound propagation, from wave based models to deep learning based methods. Given the complexity of the problem, this aspect will not be addressed in this work.

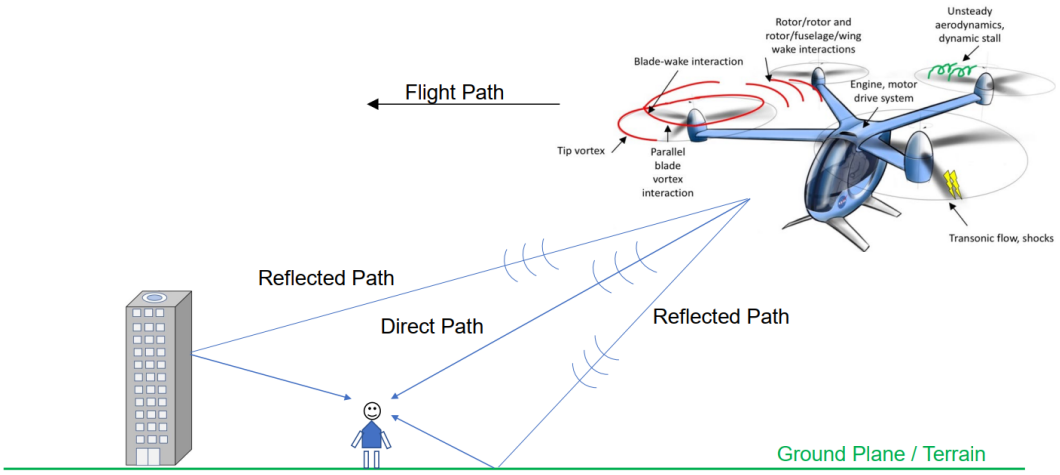


**Figure 1.5.** Noise sources in a multirotor configuration and simplified sound waves propagation diagram in a typical urban environment [6]

### 1.4.4 Solutions for Noise Reduction

The majority of studies regarding the sound footprint mitigation of these vehicles in urban environments focus particularly on designing routes for them to follow in order to avoid crowded areas and, in general, to minimize the total noise impact in the city. Other studies, unlike the previous ones, focus instead on reducing the sound emitted by the aircraft. This type of approach is proving to be very complex. In fact, rotor-powered aircraft are, by definition, very noisy—just consider the noise generated by a helicopter—primarily due to the complex aerodynamic phenomena caused by the rotation of the blades. Current solutions rely particularly on the use of sound-absorbing materials, optimized blade designs (such as the ERATO blade developed by ONERA), or design studies involving multiple smaller rotors or shrouded rotors.

**(a)** Example of use of shrouded rotors[7]

**(b)** ERATO blades on a helicopter[8]

**(c)** Multiple smaller rotors solution[9]

**Figure 1.6.** Confrontation between Analytical Tool, Fast Tool, and Complete Chain (Unsynchronized case and Phase Shift Control case) for the Exarotor configuration

An interesting methodology for reducing sound emission leverages the wave nature of sound. Since sound is a wave generated by pressure fluctuations propagating through air, we can use the property of interference to reduce the intensity of sound perceived by people near the vehicle. Specifically, each rotor can be considered as emitting a distinct sound wave, the properties of which depend on blade characteristics, angular velocity, and the blade's position at a specific moment. This last parameter is fundamentally important for this purpose, as it directly relates to the phase of the sound wave emitted by a particular rotor. Therefore, if we can control the position of the blades of one rotor relative to those of the others, we can control the phases of the sound waves emitted by each rotor and thus manage the interference between them. If we can control this "phase shift" among the rotors, we can reduce the overall emitted sound intensity or adjust the sound directionality, thereby making it possible to direct most of the sound away from crowded regions along the vehicle's trajectory over the city.

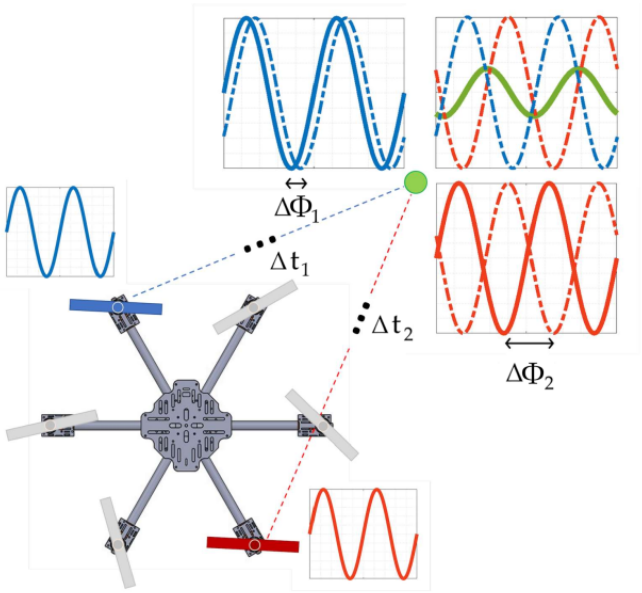


**Figure 1.7.** Interference between sound waves emitted from different rotors in a mulicopter[10]

To achieve this, it is important to recognize that, unlike most VTOLs that use fixed-pitch blades, variable-pitch blades are required here. This is because the pitch of the blades is typically fixed, allowing thrust control only through adjustments to the rotors' angular velocity. However, in this case, controlling the phase shift of the rotors necessitates adjusting the blade pitch to maintain lift while altering their relative angles. Designing and testing this technology will require extensive use of experimental setups and numerical simulations.

## 1.5 Goals of the thesis

The purpose of this work is to develop a fast simulation tool capable of modeling the sound emitted by a multirotor configuration in hover, based on a reformulation of the Ffowcs Williams-Hawkings (FW-H) equations by Farassat. Here, the sound emitted by a rotating blade is considered to consist of two principal types of noise: loading noise and thickness noise. The former is generated by the lift distribution along the blade, while the latter arises from the pressure distribution along the blade. The blade is modeled as a distribution of point sources—in this case, monopoles and dipoles. Monopoles are used to calculate the

loading noise, and dipoles are employed to compute the thickness noise. To further enhance computational efficiency, we can model the entire blade with a single monopole and a single dipole, which together describe the blade's overall properties. As demonstrated in this work, even with these simplifications, we achieve results very similar to those obtained from numerical simulations and experimental data, but with a computational time that is orders of magnitude lower. This tool is valuable for the preliminary design of the vehicle and can also be integrated into a control system to determine the optimal phase shift for each rotor, thereby minimizing the sound emitted by the vehicle in a specific direction. Thanks to this fast simulation software, this task can be performed in a very short amount of time, and with further optimization, it could also be used in real time.

# 2 | Theoretical Background

This chapter provides a brief introduction to acoustics and aeroacoustics. Acoustics can be simply defined as the study of small pressure waves in air that can be perceived by the human ear—in other words, what we commonly call sound. From this definition, we can see that acoustics can be considered a specialized branch of fluid dynamics. One of the major challenges in fluid dynamics is that the equations of motion are nonlinear, making exact general solutions unavailable. In acoustics, however, we use a linearized version of the fluid dynamics equations, where nonlinear effects are neglected, simplifying the analysis.

Aeroacoustics, on the other hand, is a relatively young field of study. Its origins can be traced back to 1952, when Lighthill formulated his aeroacoustic wave equations. These equations enabled, for the first time, a physical understanding of the sound generated by free turbulence. The key aspect of Lighthill's theory of sound generation by turbulence is the use of an integral equation, which is far more suitable for introducing approximations than a differential equation.

## 2.1 Fluid Dynamics

We begin with the Navier-Stokes equations, fundamental for describing compressible fluid dynamics. These nonlinear PDEs are derived from conservation laws:

$$\begin{cases} \dfrac{\partial \rho}{\partial t} + \nabla \cdot (\rho\, \mathbf{v}) = \dot{m}, & \text{(2.1a)} \\ \dfrac{\partial (\rho\, \mathbf{v})}{\partial t} + \nabla \cdot \Big(\rho\, \mathbf{v} \otimes \mathbf{v}\Big) + \nabla p = \nabla \cdot \boldsymbol{\tau} + \mathbf{f} + \dot{m}_{\mathbf{v}}, & \text{(2.1b)} \\ \dfrac{\partial (\rho\, e_t)}{\partial t} + \nabla \cdot (\rho\, e_t\, \mathbf{v}) + \nabla \cdot (p\, \mathbf{v}) = -\nabla \cdot \mathbf{q} + \nabla \cdot (\boldsymbol{\tau} \cdot \mathbf{v}) + \dot{\vartheta} + \mathbf{f} \cdot \mathbf{v} + \dot{m}_{e_t}. & \text{(2.1c)} \end{cases}$$

These equations represent conservation of mass, momentum, and total energy, respectively, for a compressible fluid with density $\rho$, velocity $\mathbf{v}$, and pressure $p$. The specific total energy is $e_t = e + \frac{1}{2}|\mathbf{v}|^2$, comprising internal energy $e$ and kinetic energy. Viscous effects are captured by the stress tensor $\boldsymbol{\tau}(\mathbf{v}, \mu)$, and heat flux by $\mathbf{q}(T, k)$. Source terms $\dot{m}$, $\dot{m}_{\mathbf{v}}$, $\dot{m}_{e_t}$, $\mathbf{f}$, and $\dot{\vartheta}$ account for mass, momentum, energy sources, external forces, and heat sources. Source terms like $\dot{m}$ can model mass injection, external forces, heat addition, or represent unresolved processes in simulations.

For closure, we require the thermal equation of state, $\rho = \rho(T, p)$, and the caloric equation of state, $e = e(T, p)$, relating density and internal energy to temperature and pressure, assuming thermodynamic equilibrium. This conservative form is useful as it reflects conservation balance integrals and simplifies source term inclusion.

The primitive form is derived for alternative formulations. The material derivative is $D/Dt = \partial/\partial t + \mathbf{v} \cdot \nabla$, representing change along a fluid element's path. The primitive Navier-Stokes equations become:

$$\begin{cases} \dfrac{D\rho}{Dt} = -\rho\nabla\cdot\mathbf{v} + \dot{m} & \text{(2.2a)} \\ \rho\dfrac{D\mathbf{v}}{Dt} = -\nabla p + \nabla\cdot\tau + \mathbf{f} & \text{(2.2b)} \\ \rho\dfrac{De}{Dt} = -p\nabla\cdot\mathbf{v} + \tau : \nabla\mathbf{v} - \nabla\cdot\mathbf{q} + \dot{\theta} & \text{(2.2c)} \end{cases}$$

To express energy in terms of entropy $s$, we use Gibbs' relation $T\delta s = \delta e - \frac{p}{\rho^2}\delta\rho$. Replacing internal energy, the entropy equation is:

$$\rho\frac{Ds}{Dt} = \frac{1}{T}\left(\tau : \nabla\mathbf{v} - \nabla\cdot\mathbf{q} + \dot{\theta} - \dot{m}\frac{p}{\rho}\right) \tag{2.3}$$

Viscous dissipation $\Phi = \tau : \nabla\mathbf{v} \geq 0$ increases entropy, making the process irreversible, while heat and mass sources can alter entropy in either direction.

Using $\rho = \rho(p,s)$, we have $\delta\rho = \frac{\partial\rho}{\partial p}_s \delta p + \frac{\partial\rho}{\partial s}_p \delta s = \frac{1}{a^2}\delta p - \rho\sigma\delta s$, with $a^2 = (\frac{\partial\rho}{\partial p}_s)^{-1}$ and $\sigma = -\frac{1}{\rho}\frac{\partial\rho}{\partial s}_p$. The pressure evolution equation is:

$$\frac{1}{a^2}\frac{Dp}{Dt} = \frac{D\rho}{Dt} + \sigma\rho\frac{Ds}{Dt} \tag{2.4}$$

For isentropic flows ($\frac{Ds}{Dt} = 0$), pressure and density are linked by $a^2$. Substituting entropy and density equations yields:

$$\frac{1}{a^2}\frac{Dp}{Dt} = -\rho\nabla\cdot\mathbf{v} + T\sigma(\tau : \nabla\mathbf{v} - \nabla\cdot\mathbf{q} + \dot{\theta}) + \dot{m}\left(1 - \frac{T\sigma\rho}{p}\right) \tag{2.5}$$

For perfect gases, $\rho = \frac{p}{RT}$, $de = c_v dT$, $a^2 = \gamma RT = \gamma p/\rho$, and $\sigma = 1/c_p$, closing the system in its final form:

$$\begin{cases} \dfrac{D\rho}{Dt} + \rho\nabla\cdot\mathbf{v} = \dot{m} & \text{(2.6a)} \\ \rho\dfrac{D\mathbf{v}}{Dt} + \nabla p - \nabla\cdot\tau = \mathbf{f} & \text{(2.6b)} \\ \dfrac{1}{a^2}\dfrac{Dp}{Dt} + \rho\nabla\cdot\mathbf{v} - T\sigma(\tau : \nabla\mathbf{v} - \nabla\cdot\mathbf{q}) = T\sigma\dot{\theta} + \left(1 - \sigma\dfrac{\rho T}{p}\right)\dot{m} & \text{(2.6c)} \end{cases}$$

Compressibility becomes important when flow acceleration is significant relative to the square of the sound speed, as seen in high-speed aerodynamics and acoustics, especially with high temporal gradients.

## 2.2 Acoustics

### 2.2.1 Wave Equation

Linear acoustics simplifies the complex fluid dynamics equations by considering small perturbations to a quiescent, isentropic fluid. Assuming pressure is solely a function of density, we have the constitutive relation for acoustic pressure $p_a$ and density $\rho_a$:

$$p_a = c_0^2\rho_a, \tag{2.7}$$

where $c_0$ is the constant speed of sound. The acoustic field is treated as a perturbation of the mean flow:

$$p = p_0 + p_a, \qquad p_a \ll p_0, \tag{2.8}$$

$$\rho = \rho_0 + \rho_a, \qquad \rho_a \ll \rho_0, \tag{2.9}$$

$$\mathbf{v} = \mathbf{v}_0 + \mathbf{v}_a. \tag{2.10}$$

For a quiescent fluid, $\mathbf{v}_0 = 0$, and we assume constant mean density $\rho_0$ and pressure $p_0$. Substituting this perturbation ansatz and neglecting second-order terms in the conservation equations yields the linearized mass and momentum equations:

$$\frac{\partial \rho_a}{\partial t} + \rho_0 \nabla \cdot \mathbf{v}_a = 0, \tag{2.11}$$

$$\rho_0 \frac{\partial \mathbf{v}_a}{\partial t} + \nabla p_a = 0. \tag{2.12}$$

From the momentum equation, $\nabla \times \frac{\partial \mathbf{v}_a}{\partial t} = 0$, implying irrotational acoustic velocity, and allowing us to define a scalar acoustic potential $\phi_a$ such that $\mathbf{v}_a = -\nabla \phi_a$. Substituting this into the momentum equation gives $p_a = \rho_0 \frac{\partial \phi_a}{\partial t}$. Finally, substituting this pressure-potential relation and the density-pressure relation into the mass conservation equation results in the acoustic wave equations for both the scalar potential and acoustic pressure:

$$\frac{1}{c_0^2} \frac{\partial^2 \phi_a}{\partial t^2} - \Delta \phi_a = 0, \tag{2.13}$$

$$\frac{1}{c_0^2} \frac{\partial^2 p_a}{\partial t^2} - \Delta p_a = 0. \tag{2.14}$$

### 2.2.2 Plane and Spherical Waves

To understand acoustic wave propagation, we examine plane and spherical waves.

#### 2.2.2.1 Plane Waves

For plane waves propagating in the x-direction, pressure and velocity are functions of $x$ and $t$ only: $p_a = p_a(x,t)$ and $\mathbf{v}_a = v_a(x,t)\mathbf{e}_x$. The 1D wave equation becomes:

$$\frac{\partial^2 p_a}{\partial x^2} - \frac{1}{c_0^2} \frac{\partial^2 p_a}{\partial t^2} = 0, \tag{2.15}$$

which has a general solution as a superposition of forward and backward traveling waves:

$$p_a(x,t) = f(t - x/c_0) + g(t + x/c_0). \tag{2.16}$$

Considering a forward propagating wave $p_a = f(t - x/c_0)$ and substituting into the 1D momentum equation $\rho_0 \frac{\partial v_a}{\partial t} + \frac{\partial p_a}{\partial x} = 0$, we find the particle velocity:

$$v_a = \frac{p_a}{\rho_0 c_0}. \tag{2.17}$$

Thus, for plane waves, acoustic pressure and particle velocity are proportional. For a plane wave propagating in an arbitrary direction $\mathbf{n}$, we generalize this to:

$$p_a(\mathbf{x},t) = f(\mathbf{n}\cdot\mathbf{x} - c_0 t), \tag{2.18}$$

$$\mathbf{v}_a(\mathbf{x},t) = \mathbf{n}\frac{p_a}{\rho_0 c_0} = \mathbf{n}\frac{1}{\rho_0 c_0} f(\mathbf{n}\cdot\mathbf{x} - c_0 t). \tag{2.19}$$

Time-harmonic plane waves are represented as:

$$p_a, \mathbf{v}_a \sim e^{j(\omega t - \mathbf{k}\cdot\mathbf{x})}, \tag{2.20}$$

where the wave vector is $\mathbf{k} = \frac{\omega}{c_0}\mathbf{n}$.

#### 2.2.2.2 Spherical Waves

For spherical waves from a point source, pressure depends only on radial distance $r$: $p_a = p_a(r,t)$. The wave equation in spherical coordinates simplifies to:

$$\frac{1}{r}\frac{\partial^2 (r p_a)}{\partial r^2} - \frac{1}{c_0^2}\frac{\partial^2 p_a}{\partial t^2} = 0. \tag{2.21}$$

The solution is:

$$p_a(r,t) = \frac{1}{r}\left(f(t - r/c_0) + g(t + r/c_0)\right), \tag{2.22}$$

showing pressure amplitude decays as $1/r$. For outgoing waves ($g = 0$), $p_a(r,t) = \frac{1}{r} f(t - r/c_0)$. Using the momentum equation, the radial particle velocity for spherical waves is found to be:

$$v_a(r,t) = \frac{p_a}{\rho_0 c_0} + \frac{F(t - r/c_0)}{\rho_0 r^2}, \tag{2.23}$$

where $f(t) = \frac{\partial F(t)}{\partial t}$. In the far-field ($r \to \infty$), the second term becomes negligible, and spherical waves behave locally like plane waves, with $v_a \approx \frac{p_a}{\rho_0 c_0}$.

The acoustic intensity for spherical waves is radial, and its time-averaged value $I_{av,r}$ relates to the source power $P_{av,a}$ by the spherical spreading law:

$$I_{av,r} = \frac{P_{av,a}}{4\pi r^2}. \tag{2.24}$$

The time-averaged intensity can also be expressed in terms of the rms pressure:

$$I_{av,r} = \frac{\langle p_a^2 \rangle}{\rho_0 c_0} = \frac{p_{a,rms}^2}{\rho_0 c_0}. \tag{2.25}$$

### 2.2.3 Acoustic Quantities

Key acoustic quantities include wavelength, sound pressure level, intensity level, and sound power level. Wavelength $\lambda$ is related to frequency $f$ and speed of sound $c_0$ by $\lambda = c_0/f$. Sound pressure level $L_{p_a}$

(SPL) is measured in decibels (dB) relative to a reference pressure $p_{a,ref} = 20\ \mu$Pa:

$$L_{p_a} = 20\log_{10}\left(\frac{p_{a,rms}}{p_{a,ref}}\right). \tag{2.26}$$

Acoustic intensity $\mathbf{I}_a = p_a\mathbf{v}_a$, and its level $L_{I_a}$ is relative to $I_{a,ref} = 10^{-12}$ W/m$^2$:

$$L_{I_a} = 10\log_{10}\left(\frac{I_{av,a}}{I_{a,ref}}\right), \quad I_{av,a} = \langle|\mathbf{I}_a|\rangle = \frac{1}{T}\int_{t_0}^{t_0+T}\mathbf{v}_a p_a dt. \tag{2.27}$$

Acoustic power $P_a$ is the integral of intensity over a closed surface $\Gamma$:

$$P_a = \oint_\Gamma \mathbf{I}_a \cdot d\mathbf{s}. \tag{2.28}$$

Sound power level $L_{P_a}$ is relative to $P_{a,ref} = 10^{-12}$ W:

$$L_{P_a} = 10\log_{10}\left(\frac{P_{av,a}}{P_{a,ref}}\right). \tag{2.29}$$

Specific acoustic impedance $\hat{Z}_a$ relates acoustic pressure and particle velocity in the frequency domain:

$$\hat{Z}_a(\mathbf{x},\omega) = \frac{\hat{p}_a(\mathbf{x},\omega)}{\hat{\mathbf{v}}_a(\mathbf{x},\omega)\cdot\mathbf{n}(\mathbf{x})}. \tag{2.30}$$

For plane waves, $\hat{Z}_a = \rho_0 c_0$. Average acoustic power can be expressed using impedance:

$$P_{av,a} = \frac{1}{2}\oint_\Gamma \Re\left\{\hat{Z}_a\right\}|\hat{\mathbf{v}}_a\cdot\mathbf{n}|^2 ds. \tag{2.31}$$

The real part of impedance, resistance, dictates energy flow direction: positive for passive (absorbing) surfaces, negative for active (energy-injecting) surfaces.

### 2.2.4 Impulsive Sound Sources and Free Space Green's Functions

The acoustic potential $\phi_a$ generated by a unit impulsive point source $\delta(\mathbf{x})\delta(t)$ satisfies:

$$\frac{1}{c_0^2}\frac{\partial^2\phi_a}{\partial t^2} - \Delta\phi_a = \delta(\mathbf{x})\delta(t). \tag{2.32}$$

Due to causality and radial symmetry, the solution is an outgoing spherical pulse:

$$\phi_a(\mathbf{x},t) = \frac{1}{4\pi|\mathbf{x}|}\delta(t-|\mathbf{x}|/c_0). \tag{2.33}$$

The free-space Green's function $G(\mathbf{x},\mathbf{y},t-\tau)$, representing the response to a point source at $\mathbf{y}$ and time $\tau$, is obtained by shifting the source:

$$G(\mathbf{x},\mathbf{y},t-\tau) = \frac{1}{4\pi|\mathbf{x}-\mathbf{y}|}\delta\left(t-\tau-\frac{|\mathbf{x}-\mathbf{y}|}{c_0}\right). \tag{2.34}$$

For an arbitrary source distribution $F(\mathbf{x},t)$, the acoustic pressure can be found by superposition using the retarded potential formula:

$$p_a(\mathbf{x},t) = \frac{1}{4\pi}\int_{-\infty}^{\infty} \frac{F\left(\mathbf{y}, t - \frac{|\mathbf{x}-\mathbf{y}|}{c_0}\right)}{|\mathbf{x}-\mathbf{y}|} d\mathbf{y}. \tag{2.35}$$

In the frequency domain, the free-field Green's function becomes:

$$\hat{G}(\mathbf{x},\omega) = \frac{e^{-jkr}}{4\pi r}, \tag{2.36}$$

where $r = |\mathbf{x}-\mathbf{y}|$ and $k = \omega/c_0$.

### 2.2.5 Monopoles, Dipoles and Quadrupoles

A monopole point source, representing a pulsating sphere, is modeled by a volume point source $q(t)\delta(\mathbf{x})$. The wave equation becomes $(\frac{1}{c_0^2}\frac{\partial^2}{\partial t^2} - \nabla^2)\psi_a = q(t)\delta(\mathbf{x})$, and its solution, using the retarded potential formula, is:

$$\psi_a(\mathbf{x},t) = \frac{q(t-|\mathbf{x}|/c_0)}{4\pi|\mathbf{x}|} = \frac{q(t-r/c_0)}{4\pi r}. \tag{2.37}$$

This solution incorporates the retarded time $t - r/c_0$, reflecting the finite speed of sound propagation.

A point dipole source at the origin is represented by $\mathbf{F}(\mathbf{x},t) = \nabla\cdot(\mathbf{f}(t)\delta(\mathbf{x}))$. The acoustic pressure generated by this dipole is given by:

$$p_a(\mathbf{x},t) = \nabla\cdot\left(\frac{\mathbf{f}(t-|\mathbf{x}|/c_0)}{4\pi|\mathbf{x}|}\right) = \frac{\partial}{\partial x_j}\left(\frac{f_j(t-|\mathbf{x}|/c_0)}{4\pi|\mathbf{x}|}\right). \tag{2.38}$$

This is derived using integration by parts and exploiting properties of the delta function, showing that the dipole field is the spatial derivative of the monopole field.

Similarly, a quadrupole source is characterized by a second spatial derivative, $\mathbf{F}(\mathbf{x},t) = \frac{\partial^2 L_{ij}}{\partial x_i \partial x_j}$, where $L_{ij}$ are the components of an arbitrary tensor. In the context of aeroacoustics, [L] will denote the Lighthill tensor (more on taht later). The resulting acoustic pressure is:

$$p_a(\mathbf{x},t) = \frac{1}{4\pi}\frac{\partial^2}{\partial x_i \partial x_j}\int_{-\infty}^{\infty} \frac{L_{ij}(\mathbf{y}, t-|\mathbf{x}-\mathbf{y}|/c_0)}{|\mathbf{x}-\mathbf{y}|} d\mathbf{y}. \tag{2.39}$$

For a point quadrupole at the origin, this simplifies to:

$$p_a(\mathbf{x},t) = \frac{\partial^2}{\partial x_i \partial x_j}\left(\frac{L_{ij}(t-|\mathbf{x}|/c_0)}{4\pi|\mathbf{x}|}\right). \tag{2.40}$$

### 2.2.6 Calculation of Acoustic Far Field (Fraunhofer Approximation)

For far-field calculations ($|\mathbf{x}| \gg |\mathbf{y}|$), we approximate $|\mathbf{x}-\mathbf{y}| \approx |\mathbf{x}| - \frac{\mathbf{x}\cdot\mathbf{y}}{|\mathbf{x}|}$. Using this in the retarded potential formula, and approximating $\frac{1}{|\mathbf{x}-\mathbf{y}|} \approx \frac{1}{|\mathbf{x}|}$, we obtain the Fraunhofer approximation for the acoustic pressure:

$$p_a(\mathbf{x},t) \approx \frac{1}{4\pi|\mathbf{x}|}\int_{-\infty}^{\infty} F\left(\mathbf{y}, t - \frac{|\mathbf{x}|}{c_0} + \frac{\mathbf{x}\cdot\mathbf{y}}{c_0|\mathbf{x}|}\right) d\mathbf{y}, \quad |\mathbf{x}| \to \infty. \tag{2.41}$$

This approximation retains phase differences due to source distribution within the retarded time argument, crucial for interference effects in the far field.

Applying this to a dipole source $\mathbf{F}(\mathbf{x},t) = \nabla \cdot \mathbf{f}(\mathbf{x},t)$, we get the far-field dipole pressure:

$$p_a(\mathbf{x},t) \approx -\frac{x_j}{4\pi c_0 |\mathbf{x}|^2} \frac{\partial}{\partial t} \left[ \int_{-\infty}^{\infty} f_j \left( \mathbf{y}, t - \frac{|\mathbf{x}|}{c_0} + \frac{\mathbf{x}\cdot\mathbf{y}}{c_0|\mathbf{x}|} \right) d\mathbf{y} \right]. \tag{2.42}$$

The spatial derivative is approximated by a time derivative using $\frac{\partial}{\partial x_j} \approx -\frac{1}{c_0}\frac{x_j}{|\mathbf{x}|}\frac{\partial}{\partial t}$ in the far field. The directivity pattern of a dipole is proportional to $\cos^2\varphi$, where $\varphi$ is the angle with the dipole axis.

### 2.2.7 Compactness and Incompressible Limit

Consider an oscillating sphere as a dipole source. The acoustic potential can be decomposed into near-field and far-field terms:

$$\phi_a(\mathbf{x},t) = -\frac{a^3 \cos\Theta}{2|\mathbf{x}|^2} U(t - |\mathbf{x}|/c_0) - \frac{a^3 \cos\Theta}{2c_0|\mathbf{x}|} \frac{\partial U(t - |\mathbf{x}|/c_0)}{\partial t}. \tag{2.43}$$

The near-field term dominates for distances $r \ll \lambda$ (wavelength), exhibiting incompressible behavior and decaying as $1/r^2$. In the incompressible limit ($c_0 \to \infty$), only the near-field term remains, and the retarded time becomes negligible.

Compactness is defined by the Helmholtz number $He = \frac{\omega l}{c_0} = \frac{2\pi l}{\lambda}$, where $l$ is a characteristic length scale. For $He \ll 1$, the wave equation reduces to the Laplace equation $\nabla^2 \phi_a = 0$. In compact regions ($l \ll \lambda$), the acoustic field can be approximated by incompressible potential flow theory.

### 2.2.8 Solution of Wave Equation using Green's Function

Green's function $G(\mathbf{x},t|\mathbf{y},\tau)$ solves the inhomogeneous wave equation $(\frac{1}{c_0^2}\frac{\partial^2}{\partial \tau^2} - \nabla_{\mathbf{y}}^2)G = \delta(\mathbf{x}-\mathbf{y})\delta(t-\tau)$. Using Green's theorem and properties of the delta function, the acoustic pressure $p_a(\mathbf{x},t)$ can be represented by the surface integral:

$$p_a(\mathbf{x},t) = \oint_\Gamma \int_0^T \left[ p_a(\mathbf{y},\tau) \frac{\partial G(\mathbf{x},t|\mathbf{y},\tau)}{\partial y_i} - G(\mathbf{x},t|\mathbf{y},\tau) \frac{\partial p_a(\mathbf{y},\tau)}{\partial y_i} \right] n_i ds(\mathbf{y}) d\tau. \tag{2.44}$$

For radiating surfaces, using the momentum equation to express the pressure gradient in terms of normal velocity $v_n$, we get:

$$p_a(\mathbf{x},t) = \oint_\Gamma \int_0^T \left[ p_a(\mathbf{y},\tau) \frac{\partial G(\mathbf{x},t|\mathbf{y},\tau)}{\partial y_i} + \rho_0 \frac{\partial v_n(\mathbf{y},\tau)}{\partial \tau} G(\mathbf{x},t|\mathbf{y},\tau) \right] n_i ds(\mathbf{y}) d\tau. \tag{2.45}$$

In the frequency domain, this becomes:

$$\hat{p}_a(\mathbf{x},\omega) = \oint_\Gamma \left[ \hat{p}_a(\mathbf{y},\omega) \frac{\partial \hat{G}(\mathbf{x}|\mathbf{y})}{\partial y_i} + j\omega\rho_0 \hat{v}_n(\mathbf{y},\omega) \hat{G}(\mathbf{x}|\mathbf{y}) \right] n_i ds(\mathbf{y}). \tag{2.46}$$

For a pulsating sphere, assuming small radius, and using free-field Green's function $\hat{G}(\mathbf{x}|\mathbf{y}) = \frac{e^{-jk|\mathbf{x}-\mathbf{y}|}}{4\pi|\mathbf{x}-\mathbf{y}|} \approx \frac{e^{-jk|\mathbf{x}|}}{4\pi|\mathbf{x}|}$, the far-field pressure simplifies to:

$$\hat{p}_a(\mathbf{x},\omega) = j\omega\rho_0 \hat{v}_n \frac{e^{-jk|\mathbf{x}|}}{|\mathbf{x}|} a^2. \tag{2.47}$$

For general cases, numerical methods like the Boundary Element Method (BEM) are needed. Tailored Green's functions can simplify problems with rigid scatterers by enforcing specific boundary conditions on the Green's function itself.

## 2.3 Aeroacoustics

Among the most influential theoretical frameworks in aeroacoustics are Lighthill's acoustic analogy and the Ffowcs Williams–Hawkings (FW-H) equation. Lighthill's analogy, introduced in the 1950s, revolutionized our understanding of aerodynamic noise generation by recasting the fundamental problem of sound production by turbulent flows. It's simply a reformulation of the complete equations of fluid motion into a wave equation with an equivalent source term representing turbulence-generated noise. This mathematical transformation highlights how turbulent fluctuations in a flow field act as quadrupole acoustic sources. The approach proves especially powerful for analyzing free turbulence noise, such as jet noise, where sound generation occurs primarily through fluid mixing in the absence of solid boundaries.

The FW-H equation represents a significant advancement by extending Lighthill's foundation to account for solid boundaries and moving surfaces in the flow field. Its framework introduces two additional source terms beyond Lighthill's quadrupoles: monopoles representing thickness effects (mass displacement) and dipoles capturing surface forces. This more comprehensive formulation enables accurate prediction of noise from complex aerodynamic systems such as aircraft propellers, helicopter rotors, and wind turbine blades. The equation's particular strength lies in its ability to capture the intricate interplay between fluid dynamics and solid structures, making it indispensable in practical aeroacoustic applications where surface-flow interactions dominate noise generation mechanisms.

Finally, Formulations 1 and 1A are solutions of the Ffowcs Williams-Hawkings (FW-H) equation that account for surface sources when the surface moves at subsonic speeds. Both have been widely used for helicopter rotor and propeller noise predictions for many years. However, nowadays it's recommended the use of Formulation 1A, as it offers improved accuracy and efficiency. Formulation 1 requires a numerical observer time derivative, which increases computational time and reduces result accuracy.

### 2.3.1 Lighthill's Acoustic Analogy

Aerodynamic sound is produced by unsteady fluid motion, particularly in turbulent flows such as those encountered in jet engines or around airfoils. This section presents the theoretical framework for modeling such sound, emphasizing Lighthill's theory for turbulence-induced noise and Curle's extension to include solid boundaries.

Lighthill reformulated the conservation equations of mass and momentum into an inhomogeneous wave equation to describe sound generated by turbulence in unbounded flows. The governing equation is:

$$\left(\frac{1}{c_0^2}\frac{\partial^2}{\partial t^2} - \nabla^2\right) c_0^2(\rho - \rho_0) = \frac{\partial^2 L_{ij}}{\partial x_i \partial x_j}$$

where $c_0$ represents the speed of sound, $\rho$ is the fluid density, $\rho_0$ is the mean density, and $L_{ij} = \rho v_i v_j + [(p - p_0) - c_0^2(\rho - \rho_0)]\delta_{ij} - \tau_{ij}$ is the Lighthill stress tensor. In this tensor, $v_i$ denotes velocity components, $p$ is pressure, $p_0$ is mean pressure, $\delta_{ij}$ is the Kronecker delta, and $\tau_{ij}$ is the viscous stress tensor.

The right-hand side, $\frac{\partial^2 L_{ij}}{\partial x_i \partial x_j}$, acts as a source term representing quadrupole sound sources. Due to the double spatial derivatives, quadrupoles are weak radiators. At low Mach numbers ($\mathrm{Ma} = v/c_0 \ll 1$), the acoustic power scales with $v^8$, indicating that free-field turbulence is an inefficient sound generator unless flow speeds are high.

The far-field solution for density fluctuations is given by:

$$c_0^2(\rho - \rho_0)(\mathbf{x},t) = \frac{1}{4\pi}\frac{\partial^2}{\partial x_i \partial x_j}\int_{-\infty}^{\infty}\frac{L_{ij}(\mathbf{y}, t-|\mathbf{x}-\mathbf{y}|/c_0)}{|\mathbf{x}-\mathbf{y}|}d\mathbf{y}$$

This integral shows that turbulence behaves as a distribution of quadrupole sources, radiating sound weakly in unbounded domains.

#### 2.3.1.1 Curle's Extension: Including Solid Boundaries

When solid bodies, such as airfoils, are present in the flow, sound radiation is enhanced through dipole sources. Curle extended Lighthill's theory by incorporating a surface $\Gamma_s$, defined by $f(\mathbf{x}) = 0$ (with $f < 0$ inside and $f > 0$ outside). For a rigid body with zero normal velocity, the modified solution becomes:

$$c_0^2(\rho - \rho_0)H(f) = \frac{\partial^2}{\partial x_i \partial x_j}\int_\Omega \frac{[L_{ij}]}{4\pi|\mathbf{x}-\mathbf{y}|}d\mathbf{y} - \frac{\partial}{\partial x_i}\int_{\Gamma_s}\frac{[(p-p_0)\delta_{ij} - \tau_{ij}]}{4\pi|\mathbf{x}-\mathbf{y}|}ds_j(\mathbf{y})$$

Here, $H(f)$ is the Heaviside function, and $[\cdot]$ indicates evaluation at the retarded time $t - |\mathbf{x}-\mathbf{y}|/c_0$. The first term preserves the quadrupole contribution from turbulence, while the second term introduces dipole sources arising from unsteady forces on the surface.

Dipole sources, captured by the surface integral, are more efficient than quadrupoles, with acoustic power scaling as $v^6$. At low Mach numbers, dipoles can dominate by a factor of $1/\mathrm{Ma}^2$, making them significant in practical scenarios.

Lighthill's theory establishes that sound from free turbulence arises from weak quadrupole sources, while Curle's extension demonstrates that solid boundaries introduce stronger dipole sources, amplifying sound radiation. In applications such as airfoil noise or jet-surface interactions, dipoles often overshadow quadrupoles, rendering this framework critical for predicting and mitigating aerodynamic noise. Finally, starting from Lighthill's inhomogeneous wave equation, one can derive an internal formulation that accounts for both stationary scattering objects and moving surfaces—as encountered in propeller and helicopter rotor noise. This extended formulation is known as the Ffowcs Williams–Hawkings (FW–H) equation.

### 2.3.2 Ffowcs Williams-Hawkings Equation and Farassat 1A

#### 2.3.2.1 Fwocs Williams-Hawkings Equation

The Ffowcs Williams-Hawkings (FW-H) equation is a generalized form of the inhomogeneous wave equation, capable of describing sound generation by moving surfaces and fluid motion. It is derived from the fundamental equations of fluid dynamics rearranged into an acoustically convenient form.

Starting from the inhomogeneous wave equation for the acoustic pressure $p'$:

$$\Box^2 p' = \frac{\partial}{\partial t}[\rho_0 v_n \delta(f)] - \frac{\partial}{\partial x_i}[p n_i \delta(f)] + \frac{\partial^2}{\partial x_i \partial x_j}[H(f) T_{ij}] \tag{2.48}$$

where $\Box^2 = \frac{1}{c^2}\frac{\partial^2}{\partial t^2} - \nabla^2$ is the d'Alembertian operator, $c$ is the speed of sound, $\rho_0$ is the ambient density, and $p'$ is the acoustic pressure (defined as $p' = p - p_0$, with $p_0$ being the ambient pressure). The equation incorporates source terms that represent the generation of sound. These source terms are mathematically expressed using the Dirac delta function $\delta(f)$ and the Heaviside function $H(f)$, which are defined with respect to a moving surface described by $f(\mathbf{x},t) = 0$. The vector $\mathbf{n} = \nabla f/|\nabla f|$ is the unit normal vector pointing outwards from the surface.

The terms in equation (2.48) are interpreted as follows:

- The first term on the right-hand side, $\frac{\partial}{\partial t}[\rho_0 v_n \delta(f)]$, represents the *thickness noise* source. Here, $v_n = \mathbf{v}\cdot\mathbf{n}$ is the local normal velocity of the moving surface, where $\mathbf{v}$ is the velocity of the surface. This term arises from the displacement of fluid by the moving surface, effectively acting as a monopole source distribution on the surface.

- The second term, $-\frac{\partial}{\partial x_i}[p n_i \delta(f)]$, represents the *loading noise* source. Here, $p$ is the pressure on the surface. This term arises from the forces exerted by the surface on the fluid, acting as a dipole source distribution on the surface.

- The third term, $\frac{\partial^2}{\partial x_i \partial x_j}[H(f)T_{ij}]$, represents the *quadrupole noise* source, where $T_{ij}$ is the Lighthill stress tensor (previously referred as $L_{ij}$) defined as $T_{ij} = \rho u_i u_j + (p - c^2\rho)\delta_{ij} - \tau_{ij}$. Here, $\rho$ is the fluid density, $u_i$ and $u_j$ are fluid velocity components, and $\tau_{ij}$ is the viscous stress tensor. This term accounts for sound generated by nonlinearities in the fluid flow, such as turbulence and shock waves.

In many aeroacoustic applications, especially when dealing with subsonic flows and for initial approximations, the quadrupole term is often neglected or treated as a secondary effect compared to the thickness and loading noise. This simplification is particularly relevant when focusing on noise generated directly by the moving surface itself.

The functions $\delta(f)$ and $H(f)$ are crucial for defining the sources on the moving surface. The Dirac delta function $\delta(f)$ is zero everywhere except on the surface $f(\mathbf{x},t) = 0$, where it is singular in such a way that its integral over any volume containing the surface is unity. It effectively confines the surface sources to the moving boundary. The Heaviside function $H(f)$ is 1 when $f(\mathbf{x},t) > 0$ (outside the surface) and 0 when $f(\mathbf{x},t) < 0$ (inside the surface).

For the purpose of deriving Formulations 1 and 1A, we will focus on the surface source terms, specifically the thickness and loading noise components. The FW-H equation, in this context, becomes a powerful tool for predicting noise radiated directly from the moving surface, providing a basis for further analytical and numerical developments.

#### 2.3.2.2 Farassat Formulation 1

To obtain Farassat Formulation 1, we start by considering the solution to the inhomogeneous wave equation using the free-space Green's function $G(\mathbf{x},t;\mathbf{y},\tau)$. The Green's function represents the acoustic pressure at the observer position $\mathbf{x}$ and time $t$ due to a point source at position $\mathbf{y}$ and time $\tau$. For a three-dimensional unbounded space, the Green's function is given by:

$$G(\mathbf{x},t;\mathbf{y},\tau) = \frac{\delta(g)}{4\pi r} \tag{2.49}$$

where $r = |\mathbf{x} - \mathbf{y}|$ is the distance between the source and observer, and $g = t - \tau - r/c$ is the retarded time variable.

The solution for the acoustic pressure $p'(\mathbf{x},t)$ due to the surface sources in the FW-H equation can be expressed as an integral involving the Green's function and the source terms. For Formulation 1, we consider the thickness and loading noise contributions separately.

The thickness noise component $p'_T$ is obtained from the first term of the FW-H equation:

$$\Box^2 p'_T = \frac{\partial}{\partial t}[\rho_0 v_n \delta(f)] \tag{2.50}$$

Using the Green's function solution, we get:

$$4\pi p'_T(\mathbf{x},t) = \int_{-\infty}^{t} \int_{\mathbb{R}^3} \frac{\partial}{\partial \tau}[\rho_0 v_n \delta(f)] G(\mathbf{x},t;\mathbf{y},\tau) d\mathbf{y} d\tau \tag{2.51}$$

Integrating by parts with respect to $\tau$, and noting that the Green's function depends on $t - \tau$, we can move the time derivative outside the integral:

$$4\pi p'_T(\mathbf{x},t) = \frac{\partial}{\partial t}\left\{ \int_{-\infty}^{t} \int_{\mathbb{R}^3} [\rho_0 v_n \delta(f)] G(\mathbf{x},t;\mathbf{y},\tau) d\mathbf{y} d\tau \right\} \tag{2.52}$$

Substituting the Green's function and performing the integration over the surface $f(\mathbf{y},\tau) = 0$, we arrive at the thickness noise component of Formulation 1:

$$4\pi p'_T(\mathbf{x},t) = \frac{\partial}{\partial t}\left\{ \int_{f=0} \left[ \frac{\rho_0 v_n}{r(1-M_r)} \right]_{ret} dS \right\} \tag{2.53}$$

where the subscript 'ret' indicates that the quantities within the brackets are evaluated at the retarded time $\tau = t - r/c$, and $M_r = \mathbf{M} \cdot \hat{\mathbf{r}} = (\mathbf{v}/c) \cdot \hat{\mathbf{r}}$ is the momentary Mach number component in the direction of the observer $\hat{\mathbf{r}} = (\mathbf{x} - \mathbf{y})/r$, which can be also be expressed as $M_r = M\cos(\theta)$, where $\theta$ is the angle between the source velocity vector ($\mathbf{M}$) and the observer position.

Similarly, the loading noise component $p'_L$ is obtained from the second term of the FW-H equation:

$$\Box^2 p'_L = -\frac{\partial}{\partial x_i}[p n_i \delta(f)] \tag{2.54}$$

Using the Green's function solution and applying differentiation under the integral sign, along with the approximation $\frac{\partial}{\partial x_i} \approx -\frac{\hat{r}_i}{c}\frac{\partial}{\partial t}$ for far-field observers, we obtain the loading noise component of Formulation 1:

$$4\pi p'_L(\mathbf{x},t) = \frac{1}{c}\frac{\partial}{\partial t}\left\{ \int_{f=0} \left[ \frac{p\cos\theta}{r(1-M_r)} \right]_{ret} dS \right\} + \int_{f=0} \left[ \frac{p\cos\theta}{r^2(1-M_r)} \right]_{ret} dS \tag{2.55}$$

Formulation 1 of Farassat is the sum of the thickness and loading noise components:

$$\begin{aligned} 4\pi p'(\mathbf{x},t) = 4\pi(p'_T + p'_L) = \frac{\partial}{\partial t}\left\{ \int_{f=0} \left[ \frac{\rho_0 v_n}{r(1-M_r)} + \frac{p\cos\theta}{cr(1-M_r)} \right]_{ret} dS \right\} \\ + \int_{f=0} \left[ \frac{p\cos\theta}{r^2(1-M_r)} \right]_{ret} dS \end{aligned} \tag{2.56}$$

This formulation involves an observer time derivative taken numerically, which can increase computational cost and reduce accuracy. This limitation motivates the derivation of Formulation 1A, which analytically

performs this time derivative.

#### 2.3.2.3 Farassat Formulation 1A

Formulation 1A is derived from Formulation 1 by analytically evaluating the observer time derivative. To achieve this, we need to consider how the retarded time quantities change with respect to the observer time $t$. We use the chain rule and the relationship between observer time and source time derivatives.

Let $q(\mathbf{x},\mathbf{y},\tau)$ be a quantity evaluated at the retarded time $\tau_e = t - |\mathbf{x}-\mathbf{y}(\eta,\tau_e)|/c$, where $\mathbf{y}(\eta,\tau)$ describes the motion of the surface point parameterized by $\eta$. The observer time derivative of $q$ is given by:

$$\frac{\partial}{\partial t}[q(\mathbf{x},\mathbf{y},\tau)]_{ret} = \left[\frac{1}{1-M_r}\frac{\partial q(\mathbf{x},\mathbf{y},\tau)}{\partial \tau}\right]_{\tau=\tau_e} \tag{2.57}$$

where $(1-M_r)^{-1}$ is the Doppler factor.

Applying this formula to the thickness and loading noise integrals in Formulation 1, we need to differentiate the terms $\rho_0 v_n$, $p\cos\theta$, and $r(1-M_r)$ with respect to the source time $\tau$. The time derivative of $v_n$ can be expressed as $\dot{v}_n = \frac{\partial v_n}{\partial \tau}$. Similarly, $\dot{p} = \frac{\partial p}{\partial \tau}$ represents the source time derivative of the pressure.

After performing the analytical time differentiation and some algebraic manipulation, we arrive at the thickness noise component of Formulation 1A:

$$4\pi p'_T(\mathbf{x},t) = \int_{f=0}\left[\frac{\rho_0\dot{v}_n}{r(1-M_r)^2} + \frac{\rho_0 v_n \dot{r}_i M_i}{r(1-M_r)^3}\right]_{ret} dS + \int_{f=0}\left[\frac{\rho_0 c v_n (M_r - M^2)}{r^2(1-M_r)^3}\right]_{ret} dS \tag{2.58}$$

and the loading noise component of Formulation 1A:

$$\begin{aligned} 4\pi p'_L(\mathbf{x},t) = &\int_{f=0}\left[\frac{\dot{p}\cos\theta}{cr(1-M_r)^2} + \frac{\hat{r}_i\dot{M}_i p\cos\theta}{cr(1-M_r)^3}\right]_{ret} dS \\ &+ \int_{f=0}\left[\frac{p(\cos\theta - M_i n_i)}{r^2(1-M_r)^2} + \frac{(M_r - M^2)p\cos\theta}{r^2(1-M_r)^3}\right]_{ret} dS \end{aligned} \tag{2.59}$$

Formulation 1A is the sum of these thickness and loading noise components. Here it's rewritten by separating the near-field terms ($\propto 1/r^2$) from the far-fiels terms ($\propto 1/r$). It eliminates the need for numerical differentiation of the integral, making it computationally more efficient and accurate than Formulation 1. It directly computes the acoustic pressure using surface integrals evaluated at the retarded time, with all time derivatives performed analytically.

To recap, the FW-H equation is a more general equation, applicable to both subsonic and supersonic motions, and can include surface and volume sources. Farassat 1A, however, is specifically tailored for subsonic moving surfaces with surface sources, making it particularly suitable for noise prediction in scenarios like helicopter rotors and marine propellers under non-cavitating conditions. Another significant distinction lies in how the observer time derivative is handled. Both FW-H and Farassat 1, another solution method, require numerical computation of the observer time derivative, which can increase execution time and reduce accuracy. Farassat 1A improves upon this by taking the derivative analytically, enhancing both efficiency and precision. This analytical approach is a notable advantage, especially for complex computations in aeroacoustic simulations. The choice between different formulations of the FW-H equation, including Farassat 1A, depends on the specific application. For instance, permeable surface formulations, which include both surface and volume sources, are used in scenarios where the

noise sources are enclosed by a permeable surface, such as in jet noise predictions. Farassat 1A, being for impermeable surfaces, is less applicable in such cases but excels in scenarios with clear surface definitions, like rotor blades.

### 2.3.3 Alternative formulation of thickness noise component for rigid bodies

An alternative approach exists for calculating the thickness noise, particularly in the far-field and for rigid bodies. This formulation, derived conceptually from a volume integral representation and leveraging far-field approximations, offers a different perspective on thickness noise prediction under specific conditions. While thickness noise originates from the surface, this alternative derivation explores a volume integral approach for analytical tractability in the far-field. Before the thickness noise was defined in term of surface integral, which can be rewritten in an equivalent way:

$$a_\infty^2 \rho_T'(\mathbf{x},t) = \frac{1}{4\pi}\frac{\partial}{\partial t}\int_{\partial V_B} \frac{\rho_\infty \mathbf{v}\cdot\mathbf{n}}{r|1-M_r|} dS \tag{2.60}$$

The derivation begins by considering a volume integral representation and applying far-field approximations, leading to the following expression for the thickness noise component in terms of observer time:

$$a_\infty^2 \rho_T'(\mathbf{x},t) = \frac{1}{4\pi a_\infty r_0 t}\frac{\partial^2}{\partial t^2}\int_{V_B} \frac{\rho_\infty \mathbf{v}\cdot\mathbf{e}_{r_0}}{|1-M_r|} dV \tag{2.61}$$

where the integral is now taken over the body volume $V_B$, and $\mathbf{e}_{r_0}$ represents the constant radiation direction in the far-field. To analytically evaluate the time derivatives, we perform differentiation with respect to the source time $\tau$ (as before, the time derivatives are in terms of the retarded (or emission) time) by using this relations: $\frac{\partial}{\partial t} = \frac{1}{1-M_r}\frac{\partial}{\partial \tau}$. After performing the first and second time derivatives using calculus rules, we arrive at the alternative far-field thickness noise formulation for rigid bodies:

$$\rho_T'(\mathbf{x},t) = \frac{\rho_\infty}{4\pi r_0 t}\int_{V_B}\left[\frac{\ddot{M}_r}{(1-M_r)^4} + \frac{3\dot{M}_r^2}{(1-M_r)^5}\right] dV \tag{2.62}$$

This formulation is particularly useful for simulations because, when modeling the thickness noise of a blade, it requires only the blade's volume as a parameter. In contrast, the previous formulation relied on the mass flow displacement, which is significantly more challenging to compute.

### 2.3.4 Discretized Formulations

For simulations purposes we can discretize the Farassat 1A formulation so that we can model the blade as a distrubution of point sources. That can be done if the following assumptions are adopted:

- The velocity of the noise source is subsonic
- The noise source is much faster than the observer
- The propeller's rotational speed and the velocity of the air vehicle do not vary with time

In the literature, various formulations exist due to the different ways these equations can be manipulated, as previously mentioned. The formulation taken as a reference for this work is the one described by Jan Delfs in [11]:

$$p_i'(x,t) = \frac{1}{4\pi}\left\{\frac{\frac{\partial\theta_p}{\partial\tau} + \mathbf{e}_R \cdot \frac{\partial \mathbf{M}_q}{\partial\tau}(1-M_{qR})^{-1}\theta_p}{R_i(1-M_{qR})^2} + \frac{a_\infty(M_{qR}-M_q^2)\theta_p}{R_i^2(1-M_{qR})^3}\right\} \tag{2.63}$$

$$\begin{aligned} p_i'(x,t) = \frac{1}{4\pi}\Bigg\{&\frac{\frac{\partial f_p}{\partial\tau}\cdot\mathbf{e}_R + (f_p\cdot\mathbf{e}_R)\frac{\partial\mathbf{M}_q}{\partial\tau}\cdot\mathbf{e}_R(1-M_{qR})^{-1}}{a_\infty R_i(1-M_{qR})^2} \\ &+\frac{-f_p\cdot\mathbf{M}_q + (1-M_q^2)f_p\cdot\mathbf{e}_R(1-M_{qR})^{-1}}{R_i^2(1-M_{qR})^2}\Bigg\} \end{aligned} \tag{2.64}$$

where $\theta_p$ is the mass source term ($m^3/s$) and $f_p$ is the point force (N). The mass source term accounts for the volume of flow displaced by the corresponding portion of the body considered in the discretization as it moves. In the case of a rotating blade, this can be computed by considering the displacement of the blade over one second, requiring only the blade's volume and its angular velocity.

The point force is directly related to the lift distribution over the blade. Therefore, when evaluating the loading noise produced by a rotor blade, we can utilize results from Blade Element Theory (BEM).

Since this study focuses on the sound emission from a multicopter in hover, it is important to note that, in this case, we have $\frac{\partial\theta_p}{\partial\tau} = 0$ and $\frac{\partial f_p}{\partial\tau} = 0$.

Another formulation, which follows the alternative approach for thickness noise derived earlier, is proposed in a work by Ohad Gur [12]:

$$\begin{aligned} \Delta p_{\text{loading}}(\mathbf{x},t) = \frac{1}{4\cdot\pi}\sum_k\Bigg\{&\underbrace{\frac{\dot{\mathbf{F}}\cdot\hat{\mathbf{r}}_{rel} + \mathbf{F}\cdot\hat{\mathbf{r}}_{rel}\cdot[(\dot{\mathbf{M}}\cdot\hat{\mathbf{r}}_{rel})/(1-M_r)]}{r_{rel}\cdot a\cdot(1-M_r)^2}}_{\text{far field}} \\ &+\underbrace{\frac{\mathbf{F}\cdot\hat{\mathbf{r}}_{rel}\cdot[(1-\mathbf{M}\cdot\mathbf{M})/(1-M_r)] - \mathbf{F}\cdot\mathbf{M}}{r_{rel}^2\cdot(1-M_r)^2}}_{\text{near field}}\Bigg\}_k \end{aligned} \tag{2.65}$$

$$\begin{aligned} \Delta p_{\text{thick}}(\tilde{\mathbf{x}},t) = \frac{\rho}{4\cdot\pi}\sum_k\Bigg\{&\frac{\Psi_0}{r_{rel}\cdot(1-M_r)^3}\cdot\left[\frac{\ddot{\mathbf{M}}_r}{1-M_r} + 3\left(\frac{\dot{\mathbf{M}}_r}{1-M_r}\right)^2\right] \\ &+\frac{\dot{\mathbf{M}}_r\cdot a\cdot(1+2\cdot M_r)}{r_{rel}\cdot(1-M_r)} + 2\left(\frac{M_r\cdot a}{r_{rel}}\right)^2\Bigg]\Bigg\}_k \end{aligned}$$

where $\Delta p_{\text{loading}}$ is the pressure fluctuation due to the loading noise, $\Delta p_{\text{thick}}$ is the pressure fluctuation due to the thickness noise, $\mathbf{F}$ is the aerodynamic force, $\Psi_0$ is the volume of the blade element, $r_{rel}$ is the relative distance between the source and the microphone and $k$ represents the blade element considered. In both the formulations we can distinguish between near and farfield contributions. At large distances from the noise source, the near-field contribution diminishes significantly, leaving the far-field term as the dominant component.

This dicretized version of the Farassat 1A formulation is thought for a distribution of sources that are located on the blade. This will give use good results compared to more sofisticated simulations (as CFD, mid-fidelity etc...) but the purpose now was to check if with a single point source located at the blade tip we can have a good approximation of the sound pressure level directivity with the advantage of lower computational costs.

### 2.3.5 UPM and APSIM

**UPM**[13], [14]

Unsteady Panel Method (UPM) is a software tool developed by the DLR Institute of Aerodynamics and Flow Technology, designed for the analysis of rotor and wing aerodynamics. UPM is built upon a 3D unsteady free wake panel method, capable of simulating aerodynamic characteristics of rotors and wings with complex geometries and motions in a nonlinear 3D unsteady free wake environment. It is primarily designed for rotorcraft applications, particularly in analyzing main/tail rotor interactions and incorporating rotor thrust and hub moment trimming, but its applicability extends to propellers and wings as well. UPM is verified and validated using experimental data, such as HeliNovi test data.

The core methodology of UPM revolves around solving potential flow problems using numerical panel methods. It models lifting surfaces, like rotor blades and wings, with source/sink distributions and bound vorticity to simulate displacement and lift, respectively. A key feature is its free wake generation, where wake panels are shed from the trailing edges and convected with the flow, enabling the simulation of wake roll-up and complex wake interactions. UPM offers two Kutta condition implementations: a classical tangential flow condition for linear problems and a pressure Kutta condition for unsteady flows requiring equal pressure at trailing edges.

UPM implements numerical algorithms for both rotating and non-rotating surfaces. It offers various vortex core models and vortex core growth models to handle viscous effects in the wake. To manage computational cost, UPM incorporates techniques like wake coarsening, fixed wake length, and adaptive core radius. It supports parallel execution using OpenMP and includes a Fast Multipole Method (FMM) for efficient computation.

UPM is versatile in terms of input and output data. It can use various coordinate systems and accepts input data in APSIM native format, NETCDF format, and TECPLOT-ASCII format. It also generates output files in TECPLOT and custom ASCII formats, providing data on surface pressure, section loads, wake geometry, and more.

**APSIM**[15], [16]

APSIM, Acoustic Prediction System based on Integral Methods, is a software tool developed at the DLR Institute of Aerodynamics and Flow Technology. Its primary function is to predict rotor and propeller noise radiated into the far-field, particularly for helicopter applications. APSIM's methodology is grounded in the Ffowcs Williams–Hawkings (FW-H) formulations, focusing solely on linear sound propagation and designed for wave propagation calculations over long distances in uniform flows.

The software is modular, offering a basis for numerical simulations in aeroacoustics. It incorporates various acoustic methods tailored for noise prediction of helicopter rotors and propellers, including integral formulations for both impermeable and permeable surfaces.

APSIM's theoretical foundation is based on the FW-H equation, making it specialized for aeroacoustics. It implements different integral formulations derived from the FW-H equation, including those based on blade surface pressure, blade section lift, and permeable FW-H surfaces. These formulations allow for the computation of thickness noise, loading noise, and quadrupole noise.

For numerical computations, APSIM offers rotating and non-rotating surface algorithms, adapting to different system definitions. It also supports reception time and emission time dominant algorithms for acoustic integral calculations. The program is structured into modules like BASE (general routines),

AERO (aerodynamic data processing), SURF (integration surfaces), ALGO (integral evaluation), and FORM (integral method specific routines).

APSIM accepts input data in various coordinate systems (flower, heliflow, windtunnel/DNW, apsim inertial) and supports different input file formats (APSIM native, NETCDF, TECPLOT-ASCII). Input data includes program control parameters, geometric information of the integral surface, and physical quantities on the panel center points. Output files include signature files with time and pressure data, spectrum files, and sound pressure level files.

In practice, APSIM is designed to work in conjunction with aerodynamic solvers. It is intended to be used in a two-step approach: first, aerodynamic flow field data is generated by solvers like FLOWer, TAU, or UPM, and then this data is used by APSIM to calculate sound propagation into the far field. APSIM is designed to be computationally efficient, particularly with its integral methods, and is suitable for use with CFD or CAA codes.

# 3 | Methodology

To develop a fast simulation tool for predicting the sound pressure level directivity of a multicopter configuration, I created a software based on analytical expressions derived from the Ffowcs-Williams equations. To simplify the model—and consequently reduce computational time—I assumed that the sound emission originates from a single point located at the tip of the blade. This point serves as an equivalent representation of the entire blade. Instead of performing computationally intensive CFD simulations or modeling the blade as a distribution of point sources, the blade is represented as a single rotating point.

The purpose of this simplification is to evaluate whether such an approach can provide useful insights for preliminary studies of acoustic emissions from multicopters. This simplified model offers significant advantages, such as enabling rapid simulations of proposed configurations during the design phase and facilitating faster optimization processes to determine the phase shift between rotors for controlling sound directivity.

In this chapter, I will first describe the development of the analytical tool. Next, I will analyze the pressure waves received by virtual microphones, compare the results with those obtained from numerical simulations and experimental studies, and validate the model using data from experiments conducted by NASA and simulations performed using UPM and APSIM.

The analytical tool was developed in Python, a high-level programming language that is widely used in scientific computing. The software was designed to generate configurations of multicopters with different numbers of rotors, rotor diameters, and rotor speeds. The tool calculates the sound pressure level directivity at various distances from the multicopter by positioning virtual microphones on a hemispherical surface around the configuration and later on a plane beneath it.

## 3.1 Development

As said before, the development of the software is based on the assumption that the acoustic emission originates from a single point located at the tip of the blade. In this point are located both the monopole and dipole sources. This position is not the best suited for both sources because their best positions should be computed considering the geometry of the blade and the harmonics decomposition of the sound wave (so the two kind of sources could be located at differently and not at the blade tip). However, considering the kind of simplified approach used in this study this is only a not useful complication of the model that could be considered in further studies. So, after we conceptualize a two-bladed rotor as two points rotating in circles, we can set up a virtual environment where we have an origin different from the center of the rotor but on the same plane so that we can use this model also for multirotor configuarations with a procedural geometry that will be defined later. The distance from the origin to the center of the rotor is a

constant that will be called "offset". Of course we have an offset for each of the three dimensions in space as with all the other geometry considerations that we are going to define.

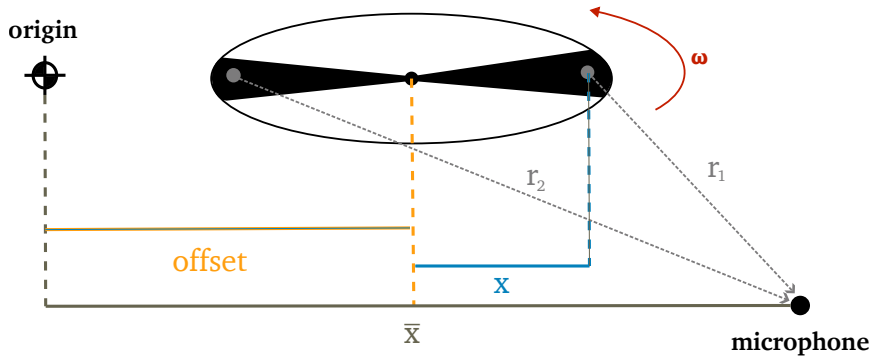


**Figure 3.1.** Geometrical representation of the rotor and the virtual microphones - where $[\bar{x},\bar{y},\bar{z}]$: coordinates of the microphones, $[\text{offeset}_x,\text{offeset}_y,\text{offeset}_z]$: coordinates of the center of the rotor, $[r_{1_x},r_{1_y},r_{1_z}]$: coordinate of the the tip of the first blade relative to the microphones, $[r_{2_x},r_{2_y},r_{2_z}]$: coordinate of the the tip of the second blade relative to the microphones.

Next, the distance from the center of the rotor to the tip of the blade (so to the sources position) is time-dependent and is defined by the following equation:

$$\begin{cases} x = r\cos(\theta_s + \omega\tau_0 + \phi) \\ y = r\sin(\theta_s + \omega\tau_0 + \phi) \\ z = 0 \end{cases} \tag{3.1}$$

where $r$ is the radius of the rotor, $\theta_s$ is the initial position of the blade (in a rotor with two blades we can consider $0^\circ$ and $180^\circ$ form the positive direction of the x-axis), $\omega$ is the angular velocity of the rotor, $\tau_0$ is the time of emission (also called "retarded time" and it's different from the time at which the pressure fluctuations are percivided from the virtual microphones) and $\phi$ is the phase shift from a reference rotor (parameter that will be useful later to study the multirotor configurations). So, given this coordinates that are in the reference frame with the center of the as origin, we can compute the real-time distance from the sources to a fixed microphones as:

$$R_{\text{obs}} = \begin{bmatrix} \bar{x} - x - \text{offeset}_x \\ \bar{y} - y - \text{offeset}_y \\ \bar{z} - z - \text{offeset}_z \end{bmatrix} \tag{3.2}$$

where $\bar{x},\bar{y}$ and $\bar{z}$ are the coordinates of the microphones and $\text{offeset}_x,\text{offeset}_y$ and $\text{offeset}_z$ are the coordinates of the center of the rotor, as shown in 3.1. So this will change dimension based on the number

of microphones that we are going to consider.

From this relations we can compute also the velocity, the acceleration and the jerk of the blade tip :

$$\begin{cases} V_x = -r\omega \sin(\theta_s + \omega\tau_0 + \phi) \\ V_y = r\omega \cos(\theta_s + \omega\tau_0 + \phi) \\ V_z = 0 \end{cases} \tag{3.3}$$

$$\begin{cases} a_x = -r\omega^2 \cos(\theta_s + \omega\tau_0 + \phi) \\ a_y = -r\omega^2 \sin(\theta_s + \omega\tau_0 + \phi) \\ a_z = 0 \end{cases} \tag{3.4}$$

$$\begin{cases} j_x = r\omega^3 \sin(\theta_s + \omega\tau_0 + \phi) \\ j_y = -r\omega^3 \cos(\theta_s + \omega\tau_0 + \phi) \\ j_z = 0 \end{cases} \tag{3.5}$$

The initialized time vector represents the first instant at which all virtual microphones perceive a sound wave for the first time. The values in this time vector differ from those of the emission time, which is needed to determine the source positions. Subsequently, these emission times are used to compute various time derivatives required for calculating pressure fluctuations. If $t$ is the time in the microphone's frame of reference, the retarded time $\tau$, which corresponds to when the pressure wave left the noise source, can be defined as:

$$\tau = t - \frac{r_{rel}(\tau)}{c} \tag{3.6}$$

where $c$ is the speed of sound and $r_{\text{rel}}(\tau)$ is the distance from the source to the microphone at time $\tau$. It is important to note that, due to the nature of this relationship, we need to solve it iteratively because the distance from the source to the microphone is time-dependent.

To perform this task we can use a classical iterative method based on the Newton-Raphson method. The Newton-Raphson method is a root-finding algorithm that uses the first few terms of the Taylor series of a function to approximate the root. A criterion for convergence should be added because in some circumnstances could happen that method is not able to converge to a good solution. In most cases this issues are easily solvable just checking all conditions.

Before any kind of computation we need to define both the geometry of the configuration and the virtual microphones. For this purpose I wrote an algorithm that, given the number of rotors plus radius and resolution of the microphones' hemishpere, computes all the necessary parameters for the simulation such as the coordinates of each rotor and the microphones coordinates over the hemisphere in grid coordinates (throuh the meshgrid function of numpy).

Now we can compute the pressure fluctuations perceived by the microphones. The pressure fluctuations are the sum of the contributions from the loading noise and the thickness noise. As already explained before the two kind of sources are located at the tip of the blade and are modeled as a dipole and a monopole respectively. The aeroacoustics formulations that I used in this work are the one derived in the works of Jan Delfs[11] and Ohad Gur[12].

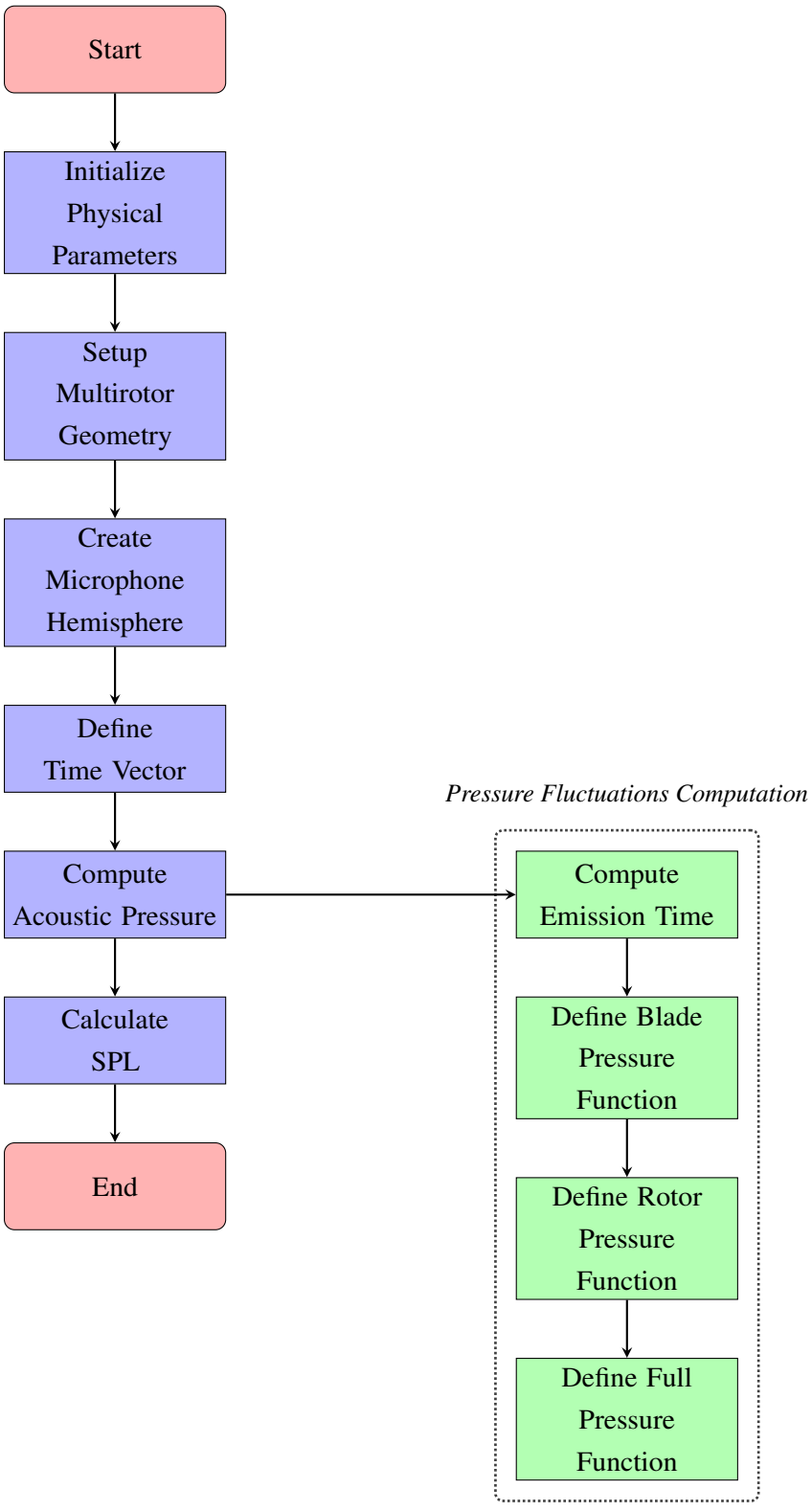


**Figure 3.2.** Block diagram describing the main steps for the computation of the sound pressure level perceived by the virtual microphones on the hemisphere sorrounding the multicopter. The secondary process (in green) describes the computation of the pressure fluctuations by superimposition of pressure fluctuations emitted from the various rotating blades of the multicopter.

## 3.2 Sources Modeling

As already stated, thanks to these formulations, to model the noise emitted by a rotating blade, we need to know only the mass flow displacement over one second due to the rotation of the blade (or only its volume in the second formulation) and the lift distribution over the blade. For the first one, we can use the following approximation:

$$\dot{m} = \frac{\pi(R_t^2 - R_h^2)t}{T} = \frac{\omega(R_t^2 - R_h^2)t}{2} \tag{3.7}$$

where $R_t$ is the tip radius of the blade, $R_h$ is the hub radius of the blade, $t$ is the thickness of the blade, $T$ is the period of the rotation, and $\omega$ is the angular velocity of the rotor.

Computing the lift distribution over a rotor blade is a complex task, typically requiring computational fluid dynamics (CFD) simulations to capture intricate flow phenomena. In this work, however, a simplified model is adopted, assuming small angles of attack and blades with a rectangular planform, providing a practical approximation for initial analysis. The lift distribution is expressed as:

$$L = \frac{1}{2}\rho V^2 c_l c \tag{3.8}$$

where $\rho$ represents the air density, $V$ is the local velocity, $c_l$ denotes the lift coefficient, and $c$ is the chord length. Although $c$ may vary in general, it is assumed constant in this simplified approach.

The best approach, particularly if we want to model the blade as a distribution of sources, is to use Blade Element Theory (BET). BET is used to evaluate the aerodynamic performance of a rotor by discretizing the blade into elements along its span and calculating the forces on each element based on local airfoil properties and flow conditions. These forces are then integrated to determine the total thrust. The blade is first discretized into $N$ elements, spanning from $r_h$ to $R$, where $R$ is the rotor radius and $r_h$ is the offset from the hub. $c$ is the chord length, and the step size is defined as $dr = \frac{(R-r_h)}{N}$.

For each element at radius $r$, the local pitch angle is given by:

$$\theta(r) = \theta_0 + \theta_1 \left(\frac{r}{R}\right) \tag{3.9}$$

where $\theta_0$ is the root pitch angle, and $\theta_1$ is the twist angle, indicating a linear pitch reduction toward the tip. In BET, the inflow is typically computed from the blade's kinematics and geometric considerations; however, it does not inherently solve for the induced velocity $v_i$, usually assuming it constant along the blade. This simplification can limit the accuracy when induced flow effects are significant. Blade Element Momentum Theory (BEMT), which combines BET with momentum theory, is more comprehensive for calculating the lift distribution. It accounts for varying induced velocities along the blade, which is crucial for accuracy in helicopter applications. This method iteratively solves for local forces and global rotor performance, ensuring a detailed lift distribution.

The induced velocity equation is derived by equating the BET thrust, given by

$$dT = b \cdot \frac{1}{2}\rho(\omega r)^2 ca \left(\theta - \frac{v_i}{\omega r}\right) dr$$

to the momentum theory thrust in hover,

$$dT = 4\pi r \rho v_i^2 dr.$$

This equality produces a quadratic equation:

$$4\pi v_i^2 + \left(\frac{b\omega ca}{2}\right) v_i - \left(\frac{b\omega^2 rca\theta}{2}\right) = 0 \tag{3.10}$$

The induced velocity $v_i(r)$ is then calculated using:

$$v_i(r) = \frac{1}{8\pi}\left(-\frac{\omega}{2}abc + \sqrt{\left(\frac{\omega}{2}abc\right)^2 + 8\pi b\omega^2 ac\theta(r)r}\right) \tag{3.11}$$

In this expression, $\omega$ (in radians per second) denotes the rotational speed, $a$ is the lift curve slope (in radians), $b$ is the number of blades, and $c$ is the chord length.

Next, the local angle of attack is determined as:

$$\alpha(r) = \theta(r) - \frac{v_i(r)}{\omega r} \tag{3.12}$$

where the term $\frac{v_i(r)}{\omega r}$ approximates the inflow angle, an assumption suitable for small induced velocities.

The differential thrust per element is expressed as:

$$dT(r) = \frac{1}{2}\rho c(\omega r)^2 a\alpha(r)\, dr \tag{3.13}$$

This represents the thrust per blade, based on a linear lift coefficient $C_l = a\alpha$.

Finally, the total thrust $T_{\text{tot}}$ is obtained by integrating $dT(r)$ over the span using Simpson's rule:

$$T_{\text{tot}} = \int_{r_h}^{R} dT(r) \tag{3.14}$$

For a rotor with $b$ blades, the total thrust should be adjusted to:

$$T_{\text{tot}} = b \int dT(r).$$

# 4 | Validation of the Analytical Tool

After developing the analytical tool, the next step is to validate it using both simulation and experimental data. This step is crucial to assess whether the tool can reliably predict the noise generated by a rotorcraft. Given the low-order fidelity of this model, perfect accuracy is not expected, particularly in matching the absolute values of sound pressure levels (SPL). However, the tool should be capable of capturing the overall trends in rotorcraft noise generation. The validation process will focus on comparing the model's results with experimental data from a prevoius work from NASA[17] and numerical simulations conducted using APSIM. Specifically, the comparison will analyze SPL directivity around the rotorcraft, visualized in polar plots. This approach serves as an effective way to evaluate the model's ability to qualitatively capture sound directionality. Initially, tests will be conducted with various phase shifts to evaluate whether the model accurately captures the influence of rotor phase shift control on sound directionality. This validation is essential to determine the model's reliability before using it in optimization procedures aimed at identifying the optimal phase shift sequence for minimizing noise emission in a given direction.

The first step will be to compare the pressure fluctuation results with those expected from experimental and typical numerical results. Then, experimental results from NASA experiments will be used to perform an initial validation regarding sound directivity. Finally, using an upscaled version of the blades from the NASA experiments and the three different multicopter configurations (4, 6, and 8 rotors), the tool will be validated against APSIM simulations.

## 4.1 Time Series for Pressure Fluctuations

As a first trial we can evaluate the pressure fluctuations in the time domain perceived by the virtual microphones. Given the two kind of sources, the monopole and the dipole, we can evaluate it as the sum of the two contributions. The monopole, which models the thickness noise of the blade, propagates isotropically in the domain while the dipole, which models the loading noise of the blade, has the maximum intensity in the direction orthogonal to the dipole axis, in this case out of the plane of the rotor. So we will have that on the rotor's plane the only contribution to the pressure fluctiation will be from the monopole source while out of plane, as we are going further and further from the rotor's plane, we will have an increasing of the relative contribution of the dipole source. Another intersting parameters to test is blade tip velocity (paramterized as Tip Mach Number: $M_t$). We can notice that with a low $M_t$, around 0.2, we have a more sinous shape of the pressure fluctuations while with a higher $M_t$, around 0.8, we have an "heart-beat" shape of the pressure fluctuations. That's due to the harmonic compositions of the sound wave. With low $M_t$ we have that amplitudes drops sharply with harmonic order while with high $M_t$ we have that amplitudes drops more slowly with harmonic order (with very high $M_t$, but still subsonics, we have an initial increase of the amplitudes with harmonic order)[18].

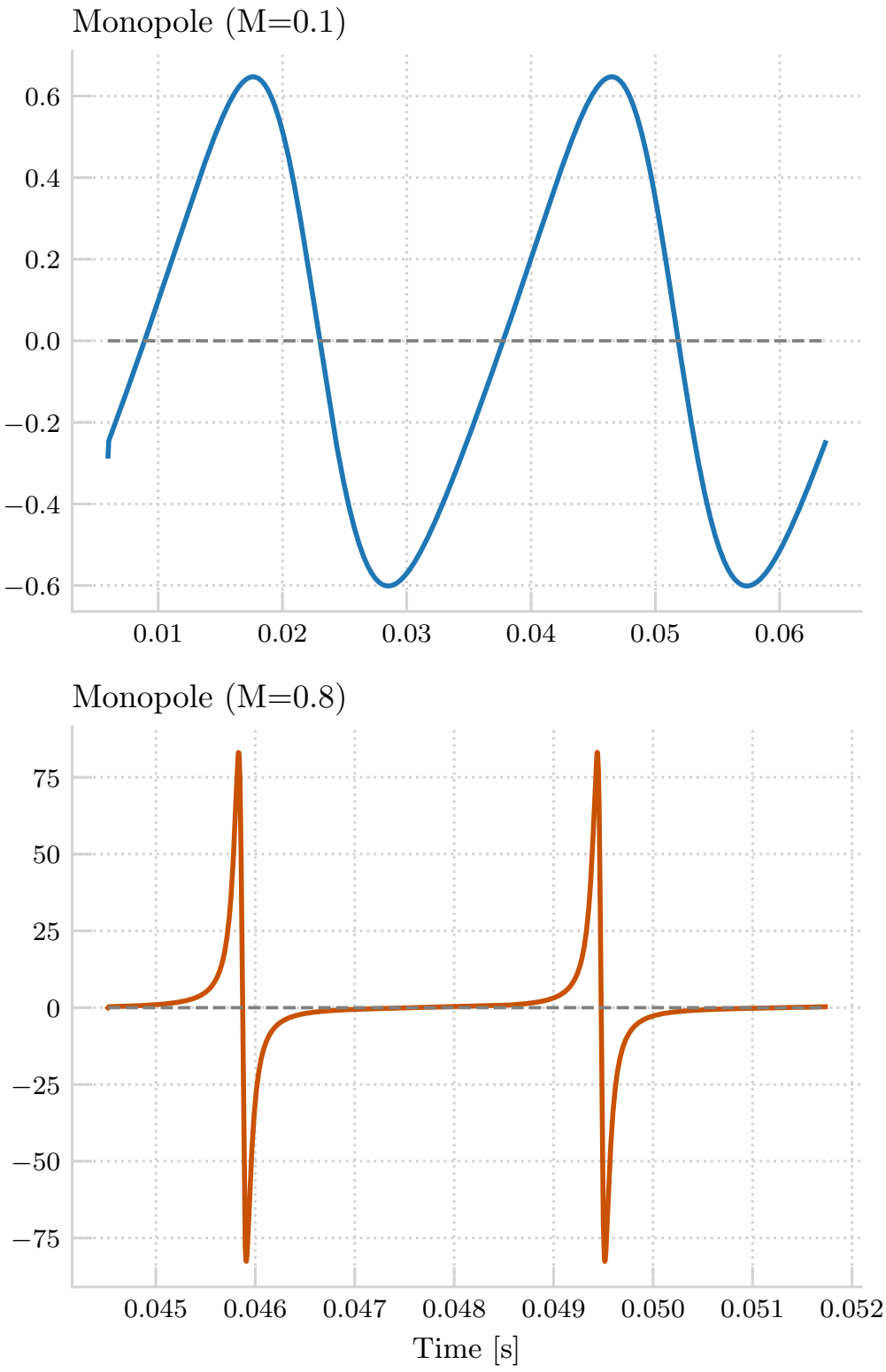


**Figure 4.1.** Pressure fluctuations generated by a rotating monopole, perceived by a virtual microphone on the hemisphere positioned at 45° below the rotor's plane. This plot highlights the different shapes of the pressure fluctuations with different Tip Mach Numbers (in the image referenced as M).

## 4.2 Validation by NASA paper

After checking that the generation of pressure fluctuations behaves as expected, we should validate the model using both simulation and experimental data. For initial validation, I compared the results from this tool with those obtained from a set of experiments and simulations conducted at NASA laboratories, as described in a paper [17]. From this experimental work, we also obtained the blade geometry (from files kindly provided by our tutors at DLR) to perform more accurate simulations using UPM and APSIM. This will allow us to compare the results from these simulations with those provided by the NASA paper and my tool. As will be shown, the analytical tool demonstrated its ability to accurately predict the sound directivity for the majority of cases, with higher accuracy for measurements taken at the rotor plane, where the dipole effect is null. This is relevant because it demonstrates that, even with a low-order accuracy model that doesn't account for aerodynamic interference and models the entire blade as a noise point source, we are able to match the trend of sound emission captured by real experiments quite accurately.

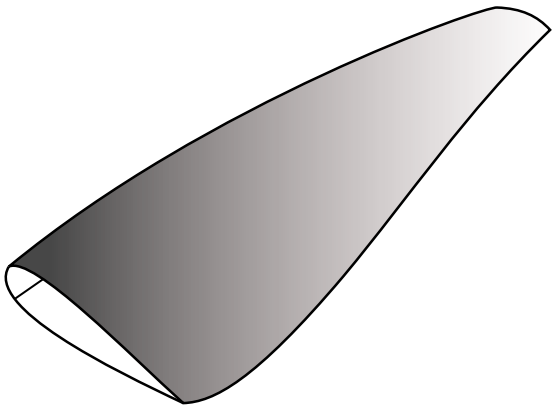

**Figure 4.2.** Sketch of the blade geometry from NASA paper. CF125 designed by KDE Direct[17].

| | |
|---|---|
| $c_{75}$ | $0.024\,\mathrm{m}$ |
| $R$ | $6.25 \cdot c_{75}$ |
| Root cut-out | $1.95 \cdot c_{75}$ |
| $\theta_0$ | $15°$ |
| $\theta_1$ | $6.5°$ |
| $\omega$ | $534\,\mathrm{rad\,s^{-1}}$ |

**Table 4.1.** Blade parameters from NASA paper. CF125 designed by KDE Direct. From the table: $c_{75}$ is the chord at 75% of radius, $\theta_0$ is the twist angle of the blade at the root of the blade, $\theta_1$ is the parameter for the linear twist.

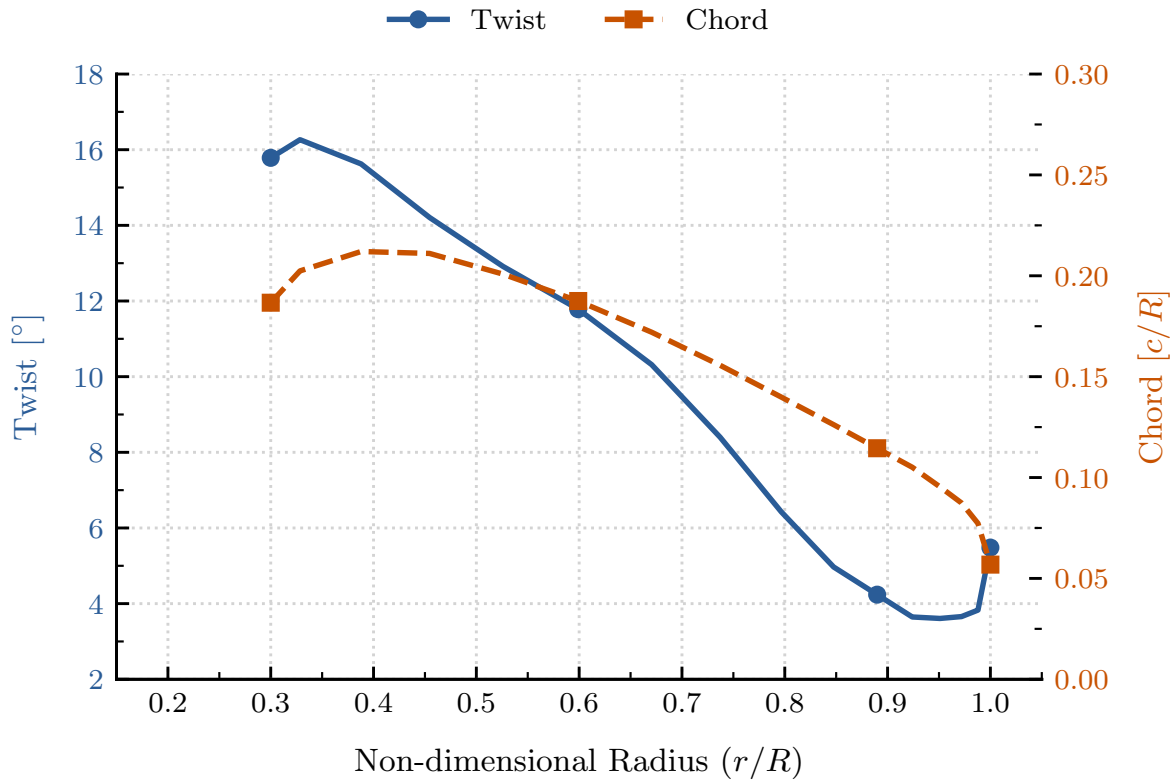


**Figure 4.3.** Radial distributions of the rotor blade chord and twist (pitch) angle. The chord is expressed as a fraction of tip radius. Kindly provided by Sessini[19]

.

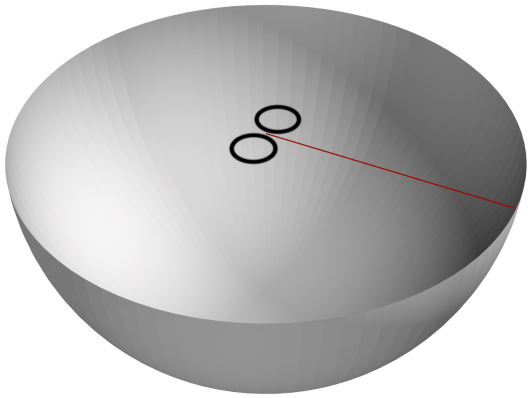

**Figure 4.4.** Geometrical set-up reproducing the experiments performed in [17]. The radius of the hemishpere is 1.9 m, the red line is the x-axis (corresponding to the 0° direction in the polar diagram). The hub-to-hub separation is of 0.4 m along the y-axix (rotors are aligned at the y-axis and the configuration is symmetrical with respect to the x-axis).

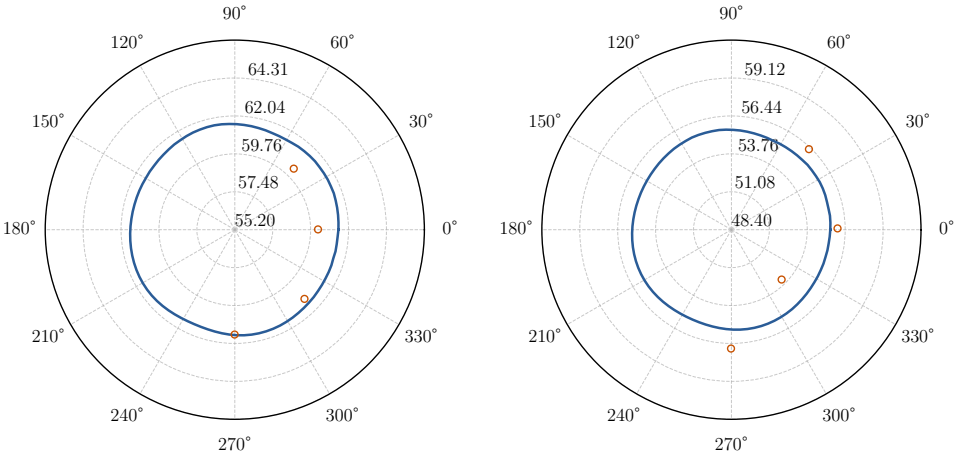


**(a)** single rotor at the origin

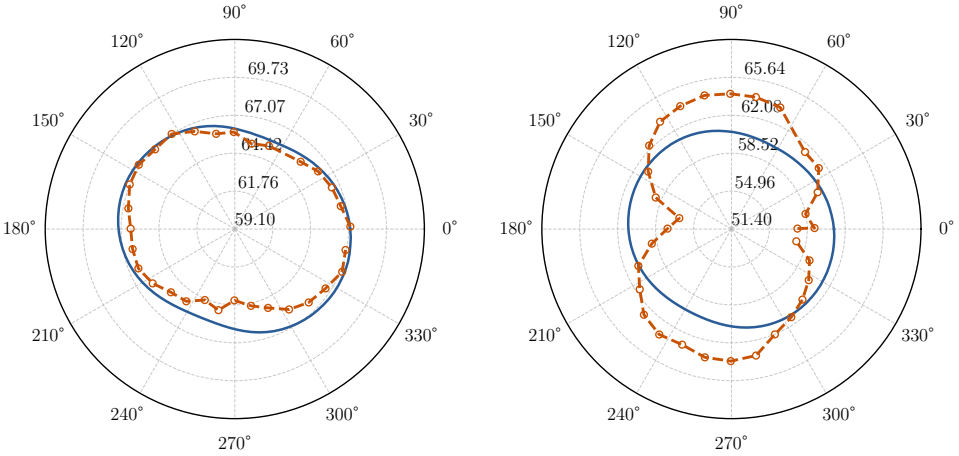


**(b)** co-rotating, 0° phase shift

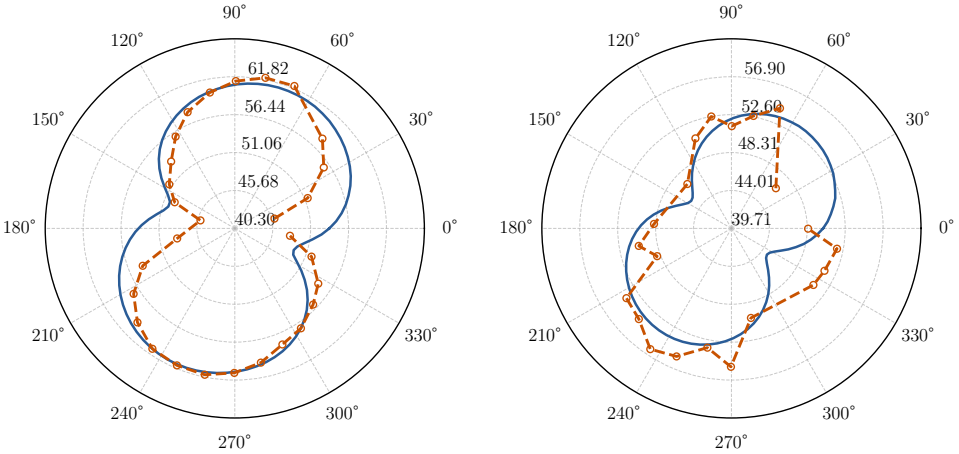


**(c)** co-rotating, 90° phase shift

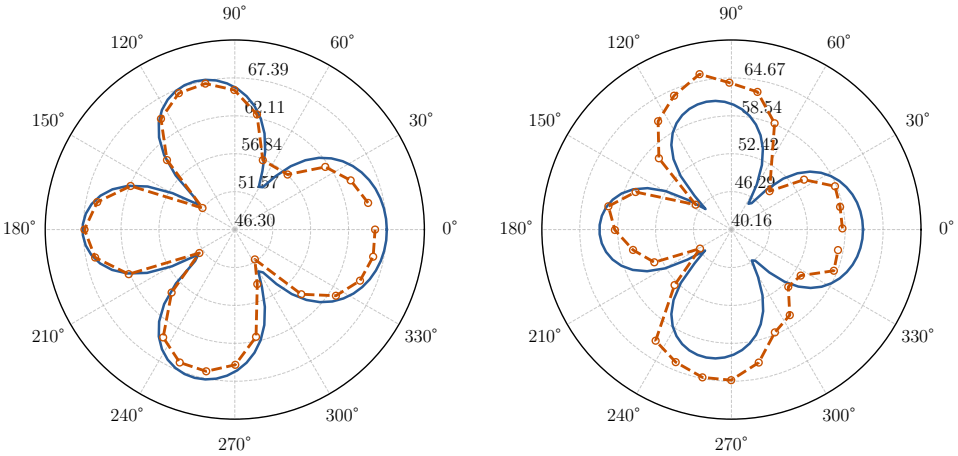


**(d)** counter-rotating, 0° phase shift

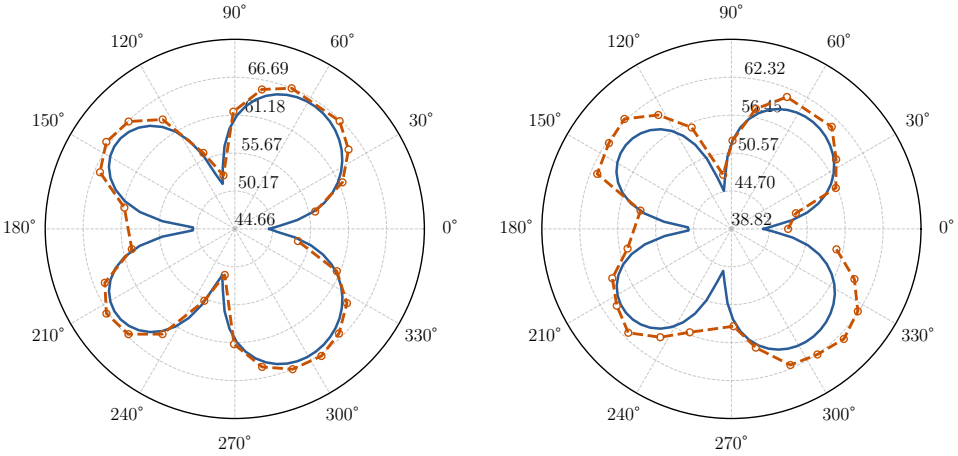


**(e)** counter-rotating, 90° phase shift

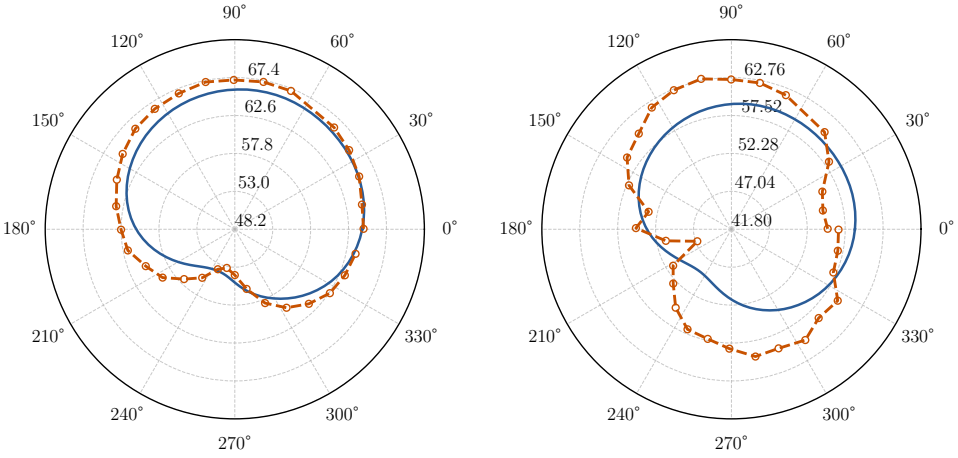


**(f)** co-rotating, 45° phase shift

**Figure 4.5.** Comparison between experimental data obtained in [17] and results of simulations performed by the simplified model. For any case at the left there are the results for the slice of the hemisphere at the rotor's plane while at the right for the slice at 45° below.

## 4.3 Validation by APSIM

Following the validation of APSIM and the analytical tool using the results from the NASA paper, I can now proceed to validate other rotorcraft configurations by comparing the results from my tool with those from APSIM. For the APSIM simulations, I will utilize an upscaled version of the blades used in the NASA paper. For future development, a new blade design optimized for this purpose will be a better choice.

| | |
|---|---|
| $c_{75}$ | 0.168 m |
| $R$ | 1.1 m |
| $\theta_0$ | 15° |
| $\theta_1$ | 6.5° |
| $\omega$ | 110 rad s$^{-1}$ |

**Table 4.2.** Upscaled blade parameters for APSIM simulations. Kindly provided by Donnini[20]

To expedite the simulation process, instead of conducting full simulations in UPM before inputting the results into APSIM, I will employ a simulation performed on a single rotor. Subsequently, I will sum up this pressure field multiple times, corresponding to the number of rotors, by simply translating and rotating it based on their respective positions. This approach is also preferable in the initial stages compared to a full simulation because it does not account for aerodynamic interference between the various rotors, an aspect that the analytical tool inherently does not consider. For this script, now referred to as the 'fast tool,' I would like to express my gratitude to my colleague, Francesco Sessini, who developed it as a tool for his research[19].

For this task, three kinds of configurations will be used: the quadrotor, the hexarotor, and the octarotor. They will be generated using the following scheme:

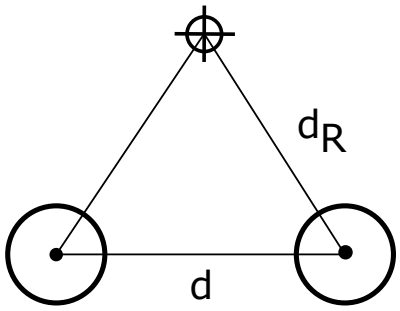


**Figure 4.6.** Scheme for the definition of the various geometries (quadrotor, hexarotor and octarotor).

$$
\begin{aligned}
d_R &= 3.5 \cdot \frac{N}{6} \\
d &= d_R \cdot 2 \cdot \sin\left(\frac{360 \cdot \pi}{N \cdot 180}\right)
\end{aligned}
\tag{4.1}
$$

where $N$ is the number of rotors, $d$ is the hub-to-hub distance and $d_R$ is the distance of each rotor's hub from the origin of the configuration.

Below are the three kinds of configurations that I will use for the validation of the analytical tool with the fast tool. The first is the quadrotor, which is the simplest configuration and the one I will use for the first validation. The second is the hexarotor, which is a configuration with six rotors, and the third is the octarotor, which is a configuration with eight rotors.

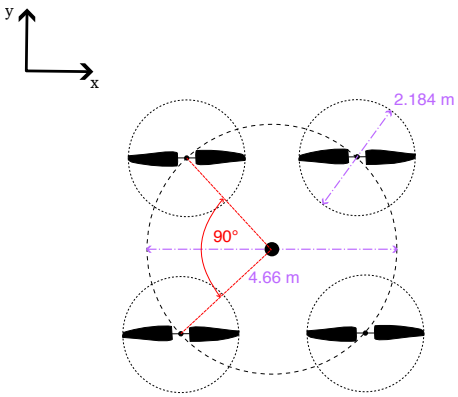


**(a)** quadrotor

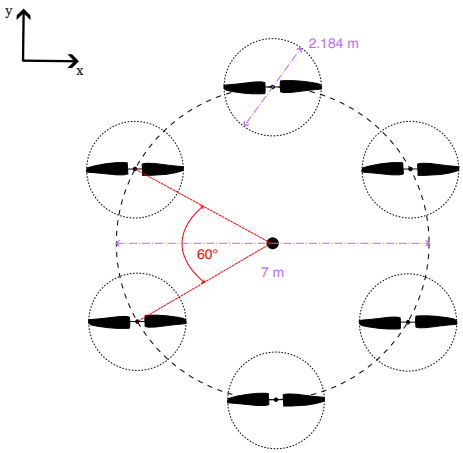


**(b)** hexarotor

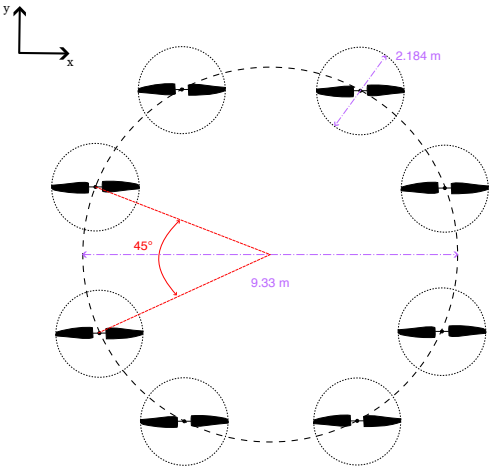


**(c)** octarotor

**Figure 4.7.** Geometrical data of the 3 multicopter typologies used for the test.

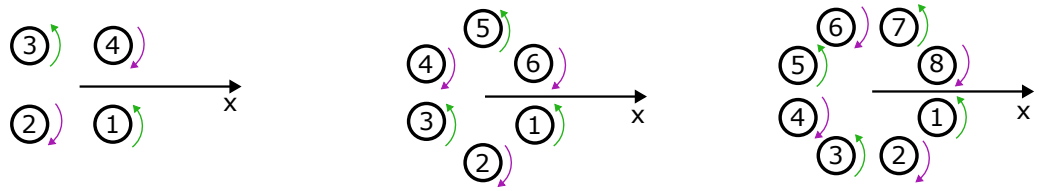


**(a)** quadrotor **(b)** exarotor **(c)** octarotor

**Figure 4.8.** Rotors are alternated in counter-clockwise (green arrow) and clockwise (purple arrow) directions. The numbering of the rotors here will serve as the reference for the structure of the phase vector that will be used later. Rotor 1 will always be the reference for the phase shift of the other rotors and, for convenience, will always be set to 0°.

| | Quad | Exa | Octa |
|---|---|---|---|
| Weight [kg] | 300 | 300 | 300 |
| Diameter [m] | 4.66 | 7 | 9.33 |
| Hub-hub distance [m] | 3.3 | 3.5 | 4.66 |
| Rotor diameter [m] | 2.184 | 2.184 | 2.184 |
| Disc Loading [$\mathrm{N\,m^{-2}}$] | 735.75 | 735.75 | 735.75 |

**Table 4.3.** Design characteristics of the multicopter configurations.

These configurations will be positioned in a virtual environment surrounded by virtual microphones. These virtual microphones will be placed, as in the previous test, in the shape of a hemisphere with a radius of 14.5 meters.

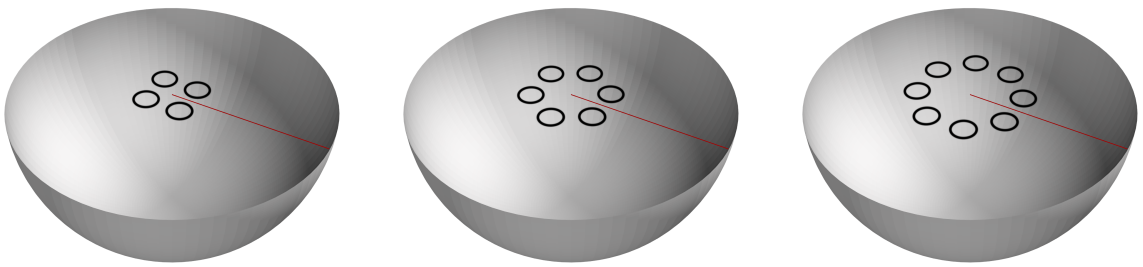

**(a)** quadrotor **(b)** exarotor **(c)** octarotor

**Figure 4.9.** Multicopter configurations represented in the testing setup with the hemisphere of virtual microphones. For all three configurations, the hemisphere will have a radius of 14.5 m.

For the test, I will use the hexarotor configuration with three different phase sequences to compare the APSIM results (fast tool) with the analytical tool. As will be shown, the accuracy will be very good because, in this case, we are neglecting aerodynamic interferences even in the numerical simulations.

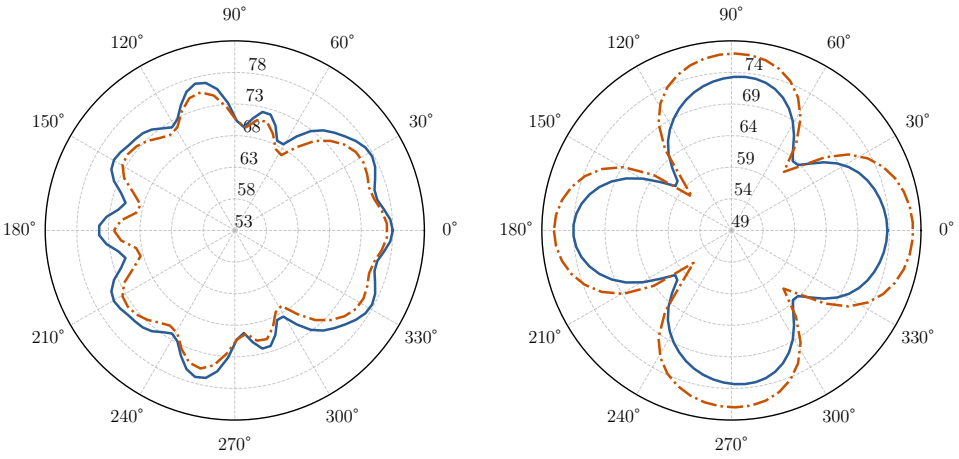


**(a)** phases : [0,0,0,0,0,0]°

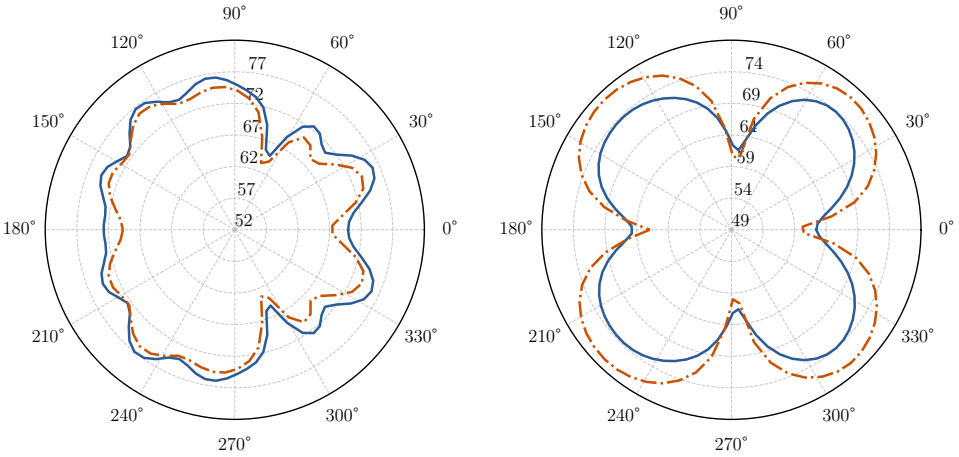


**(b)** phases : [0,90,0,90,0,90]°

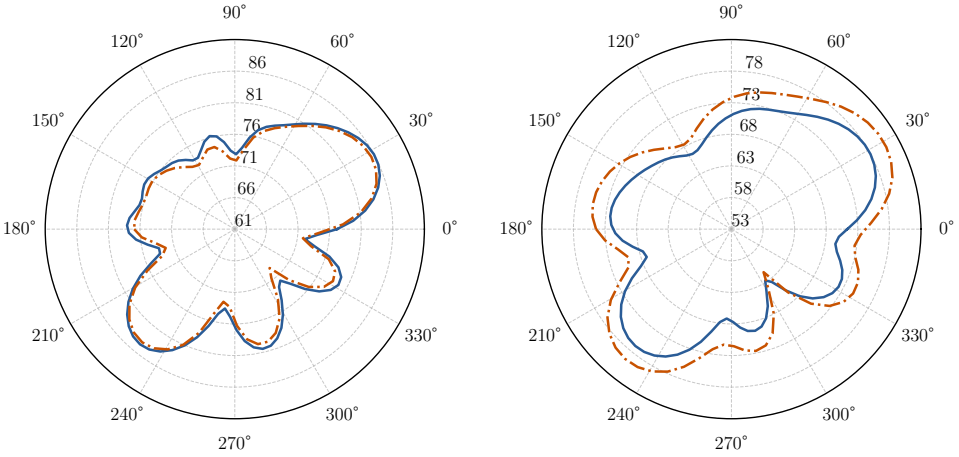


**(c)** phases : [0,0,90,0,0,90]°

**Figure 4.10.** Comparisons of the results obtained in APSIM (orange dotted line) and with the analytical tool for the exarotor configuration. left: rotor's plane, right: 45° below.

# 5 | Active Noise Canceling by Phase Shift Control

## 5.1 Introduction

In this chapter, the application of the previously developed analytical tool will be described to minimize the Sound Pressure Level (SPL) in a specified region of a hemisphere or a plane below it, using phase shift control. This minimization is achieved through the use of a Genetic Algorithm, which optimizes the mean SPL values measured by a set of virtual microphones positioned within the target region.

Results from the analytical tool will be compared with those obtained from the complete simulation chain conducted by Donnini[20], using the same phase shifts computed by my optimization procedure. These numerical results—which account for aerodynamic interference—will serve as an important testbench for the model if it can quickly compute the optimal phase shift sequence for sound minimization in a given direction and apply it effectively in a realistic scenario to achieve favorable outcomes. This comparison aims to assess whether applying the optimized phase values to each method produces consistent, reliable, and meaningful results.

### 5.1.1 Strategy

For this analysis, I defined a hemispherical region with a radius of 14.5 meters centered on the multicopter configuration, along with a horizontal plane positioned 25 meters below the center to simulate the ground. The plane represents the surface where sound would be perceived by people as the eVTOL flies overhead, while the hemisphere captures the acoustic directivity of the sound in the air. This setup enables a detailed assessment of the Sound Pressure Level (SPL) both in the surrounding airspace and at ground level, offering valuable insights into how the noise generated by the eVTOL impacts observers on the ground.

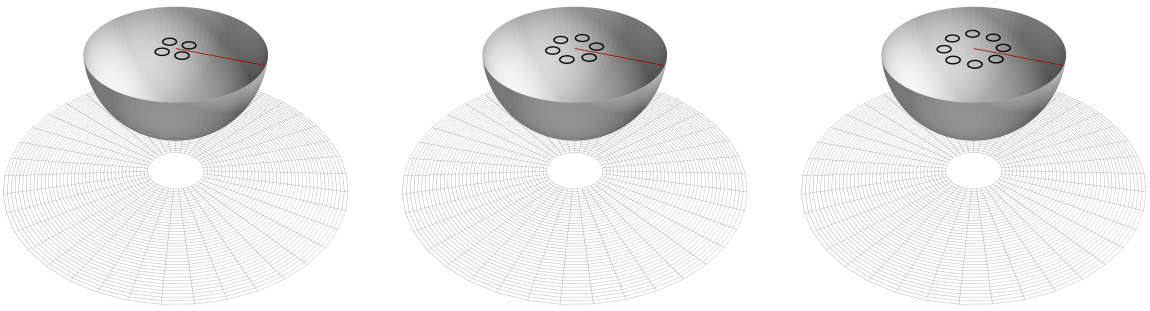

**(a)** quadrotor **(b)** exarotor **(c)** octarotor

**Figure 5.1.** Hemisphere and plane for each configuration

I divided both the hemisphere and the plane into nine regions, each spanning 40 degrees, to enable the algorithms to minimize the mean SPL within these specific areas. For the hemisphere, the optimization targeted the section located 45 degrees below the rotor plane, where virtual microphones were placed at 4-degree intervals to capture detailed acoustic data. On the plane, the region of interest extended radially from 5 to 30 meters from the projection of the configuration center onto the ground. Virtual microphones were positioned at 1-meter intervals within this range to accurately simulate sound perception at ground level.

The image below illustrates the microphone configuration for one of the nine regions, providing a clear visualization of their placement and coverage.

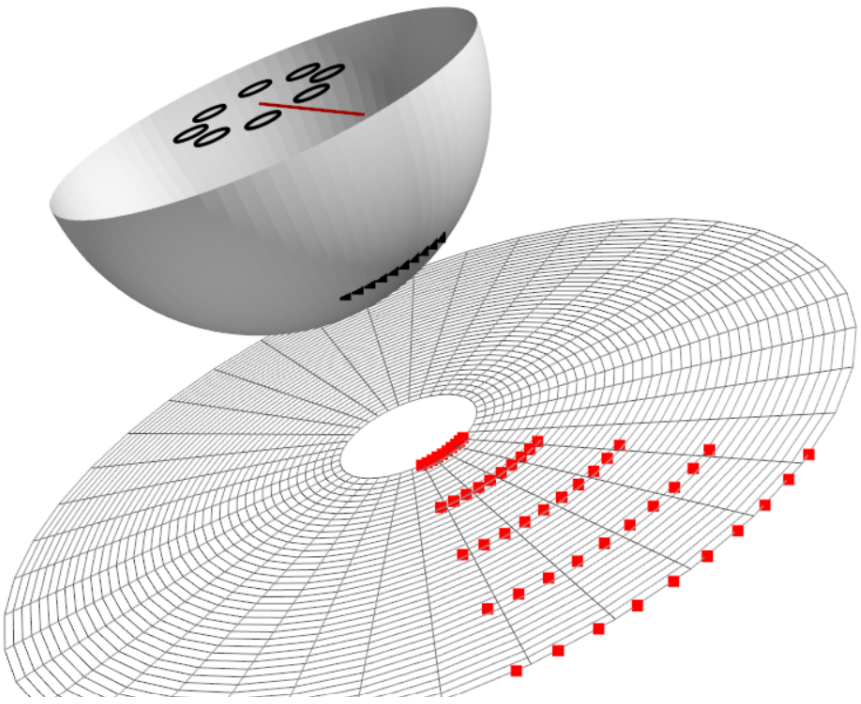

**Figure 5.2.** Microphone positions on the hemisphere and plane in one of the sections considered for optimization. The same arrangement applies to all other sections.

Below is a table showing the different portions considered for minimization.

| Section | Ranges |
|---|---|
| 1 | -20 \| 20 |
| 2 | 20 \| 60 |
| 3 | 60 \| 100 |
| 4 | 100 \| 140 |
| 5 | 140 \| 180 |
| 6 | 180 \| 220 |
| 7 | 220 \| 260 |
| 8 | 260 \| 300 |
| 9 | 300 \| 340 |

**Table 5.1.** Sections for minimization (in degrees with respect to x-axis)

### 5.1.2 Optimizer

The optimization process is designed to minimize noise by adjusting the phase of each rotor relative to a fixed reference rotor. One rotor is assigned a constant phase of $0^\circ$ with respect to its standard initial position, serving as the reference point, while the phases of the remaining rotors are optimized within a range of $\pm 90^\circ$. These continuous phase shifts serve as the key parameters in the optimization.

For a system with $N$ rotors, the problem involves optimizing $N-1$ variables. For example, a quadrotor system requires optimizing three variables, a hexarotor system five, and an octarotor system seven.

The objective function to be minimized is the mean Sound Pressure Level (SPL) measured at virtual microphones positioned within the designated noise reduction area. By minimizing this function, the algorithm determines the optimal phase relationships among the rotors, ultimately achieving maximum noise reduction.

## 5.2 Genetic Algorithm

In this work, the optimization of rotor phase shifts is carried out using a *Real-Coded Genetic Algorithm (RCGA)*, a bio-inspired method that mimics natural selection and genetic evolution. The RCGA is particularly well suited for minimizing the mean Sound Pressure Level (SPL) measured by virtual microphones in a specified region. This problem is inherently complex due to its non-linearity and multi-modal nature. Traditional gradient-based methods often struggle with such challenges because the cost function—here, the mean SPL—is prone to discontinuities and multiple local minima. This makes a stochastic, global search method like a Genetic Algorithm (GA) more effective for finding near-optimal solutions.

The problem is defined using the phase shifts of the rotors relative to a fixed reference rotor, whose phase is set at $0^\circ$. The remaining rotors have their phases optimized within a range of $\pm 90^\circ$. For a system with $N$ rotors, there are $N-1$ variables. For example, a quadrotor has three variables, a hexarotor has five, and an octarotor has seven. These phase shifts are represented as real-valued continuous variables.

The implementation, as shown in C.2., begins by generating an initial population of candidate solutions. Each candidate is a vector of phase shifts, randomly initialized within the defined bounds. The cost

function evaluates each candidate by calculating the mean SPL at virtual microphones located in the region of interest. Lower SPL values indicate a better (or "fitter") solution.

The algorithm proceeds iteratively through a series of steps. First, a selection mechanism based on *roulette wheel selection* assigns higher probabilities to candidates with lower SPL values. This probabilistic selection ensures that better-performing solutions have a higher chance of contributing to the next generation. Once parents are selected, a crossover operator creates new offspring by linearly combining the parent phase vectors. This crossover is controlled by a random factor, which allows the offspring to explore new regions of the solution space while still inheriting favorable traits from their parents.

Mutation is then applied to the offspring by adding small, normally distributed random changes to the phase values. This step is crucial for maintaining diversity within the population, helping the algorithm avoid premature convergence on suboptimal solutions. After mutation, boundary conditions are enforced so that all phase shifts remain within the $[-90°, +90°]$ interval. The offspring are then evaluated with the same cost function, and the combined pool of parents and offspring is sorted by performance. The best candidates are selected to form the new population for the next iteration.

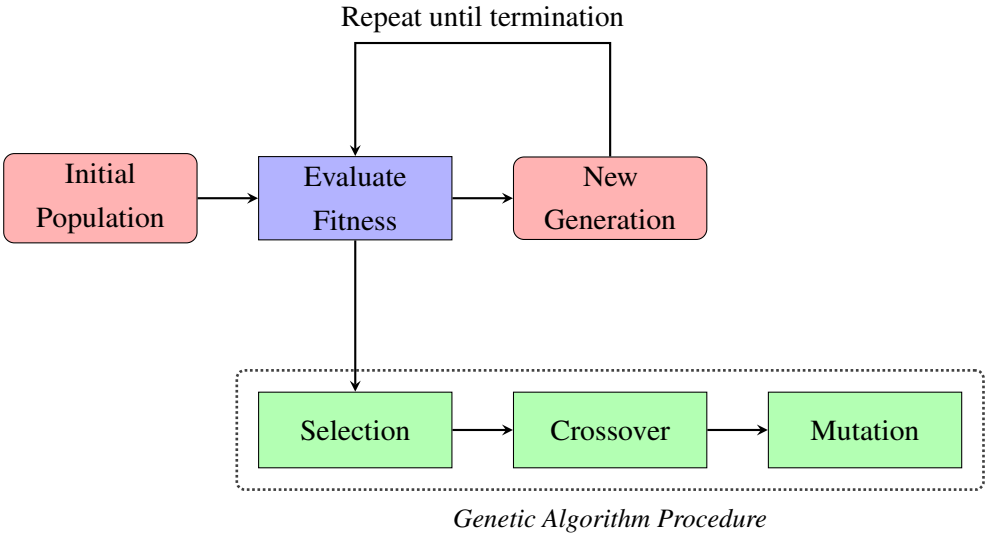


**Figure 5.3.** Genetic algorithm workflow. The cycle continues until termination criteria are met (e.g., optimal solution found or generation limit reached).

The process repeats for a predetermined number of generations, or until improvements in the cost function fall below a specified threshold. Throughout the iterations, the algorithm keeps track of the best solution encountered, which ultimately provides the optimized set of rotor phase shifts that minimizes the mean SPL.

The choice of a GA for this problem is driven by its robustness and flexibility. The algorithm is capable of handling a wide range of variables and constraints, and its stochastic nature allows it to effectively search through a complex optimization landscape. Moreover, by employing a real-coded representation, the algorithm directly works with the continuous nature of the phase shifts, avoiding the complications of binary encoding and decoding. The parameters in the Python implementation—such as the selection pressure factor ($\beta$), crossover probability ($p_c$), mutation probability ($\mu$), and mutation intensity ($\sigma$)—are tuned to balance exploration and exploitation, ensuring a thorough and efficient search. The primary reference for the code is a work by Heris[21].

## 5.3 Results

After completing the previous steps, I applied the optimization procedure to all configurations. Initially, I focused on minimizing the Sound Pressure Level (SPL) in specific portions of the hemisphere, particularly the slice located at 45 degrees below the rotor plane. Subsequently, I extended this procedure to the corresponding portions of the plane below the hemisphere. In this section, I present the results of these two optimization procedures, comparing their outcomes and assessing their relative effectiveness.

The phases calculated through the optimization procedure were then input into Donnini's model[20] to validate whether noise minimization is achieved in a more comprehensive and precise simulation environment. To quantify the actual SPL reduction across the target sections, we compare the SPL values from a case where no control is applied to the effective position of the blades over time with the other results. From now on, these results will be referred to as the 'unsynchronized case,' and I would like to express my gratitude to Sessini for providing this data for my work[19].

The subsequent pages present the computed phase shifts for all cases in this study, along with the results from the complete numerical model. It is important to note that these results were obtained with an emphasis on rapid computation and convergence. More refined outcomes could be achieved by further improving the model's discretization, employing a more robust optimization procedure, and extending the computation sessions. In this work, the full optimization procedure takes on the order of minutes per section, although satisfactory results were sometimes obtained in under one minute, depending on the randomness of the GA's initial population. Notably, beyond a certain increase in population size—and thus computational effort—there is no significant improvement in performance. For future developments, a more advanced optimization software should be used to enhance both computational time and performance; here, this simple algorithm was implemented solely to validate the approach. All results for each section can be found in the appendices. Here, we present only one minimization example for each case, while all data on SPL reduction is reported.

### 5.3.1 Hemisphere slice minimization

#### 5.3.1.1 Quadrotor

| | Rotors | | | |
|---|---|---|---|---|
| Sects. | 1 | 2 | 3 | 4 |
| 1 | 0 | 45 | -85 | -7 |
| 2 | 0 | -55 | 57 | -83 |
| 3 | 0 | 30 | 30 | -1 |
| 4 | 0 | 27 | 28 | -19 |
| 5 | 0 | 46 | 62 | -61 |
| 6 | 0 | -5 | 72 | 60 |
| 7 | 0 | -10 | -45 | 17 |
| 8 | 0 | -28 | -32 | 1 |
| 9 | 0 | 29 | -28 | 85 |

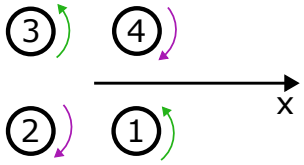


**Table 5.2.** Phase shifts for sound minimization in each section (Quadrotor, hemisphere slice)

| Section | 1 | 2 | 3 | 4 | 5 | 6 | 7 | 8 | 9 |
|---|---|---|---|---|---|---|---|---|---|
| UNSYNC | 76.9 | 76.9 | 76.9 | 76.9 | 76.9 | 76.9 | 76.9 | 76.9 | 76.9 |
| CHAIN | 66.2 | 74.38 | 66.75 | 68.71 | 65.83 | 67.88 | 74.55 | 71.05 | 69.22 |

**Table 5.3.** Mean SPL over sections (Unsynchronized Rotors, Complete Chain)

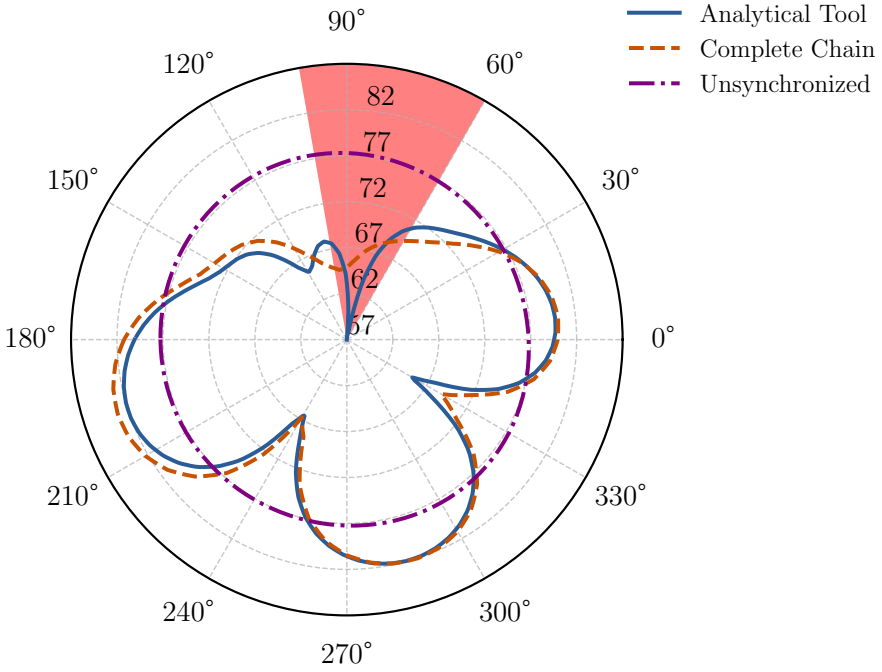


**Figure 5.4.** Comparison of optimization results from the Analytical Tool and Complete Chain against the Unsynchronized case for the Quadrotor configuration. Here, the case for section 3 is shown. The light red wedge highlights the section affected by the minimization.

#### 5.3.1.2 Hexarotor

| | Rotors | | | | | |
|---|---|---|---|---|---|---|
| Sects. | 1 | 2 | 3 | 4 | 5 | 6 |
| 1 | 0 | -37 | -28 | 25 | -32 | 5 |
| 2 | 0 | -8 | -26 | 39 | 3 | -6 |
| 3 | 0 | 17 | 39 | -8 | 28 | -31 |
| 4 | 0 | -27 | -17 | -54 | 27 | -12 |
| 5 | 0 | 67 | 29 | 20 | 22 | 22 |
| 6 | 0 | -45 | 1 | -53 | -44 | -23 |
| 7 | 0 | -13 | 41 | 29 | 16 | 12 |
| 8 | 0 | -53 | -4 | -57 | -32 | -6 |
| 9 | 0 | -4 | -44 | 26 | 4 | -2 |

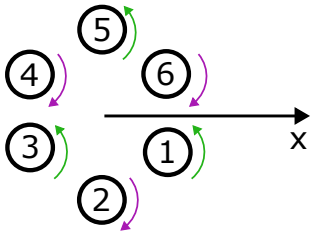


**Table 5.4.** Phase shifts for sound minimization in each section (Hexarotor, hemisphere slice)

| Section | 1 | 2 | 3 | 4 | 5 | 6 | 7 | 8 | 9 |
|---|---|---|---|---|---|---|---|---|---|
| UNSYNC | 78.92 | 78.92 | 78.92 | 78.92 | 78.92 | 78.92 | 78.92 | 78.92 | 78.92 |
| CHAIN | 70.9 | 68.38 | 69.87 | 66.9 | 66.45 | 67.2 | 68.37 | 69.34 | 67.1 |

**Table 5.5.** Mean SPL over sections (Unsynchronized Rotors, Complete Chain)

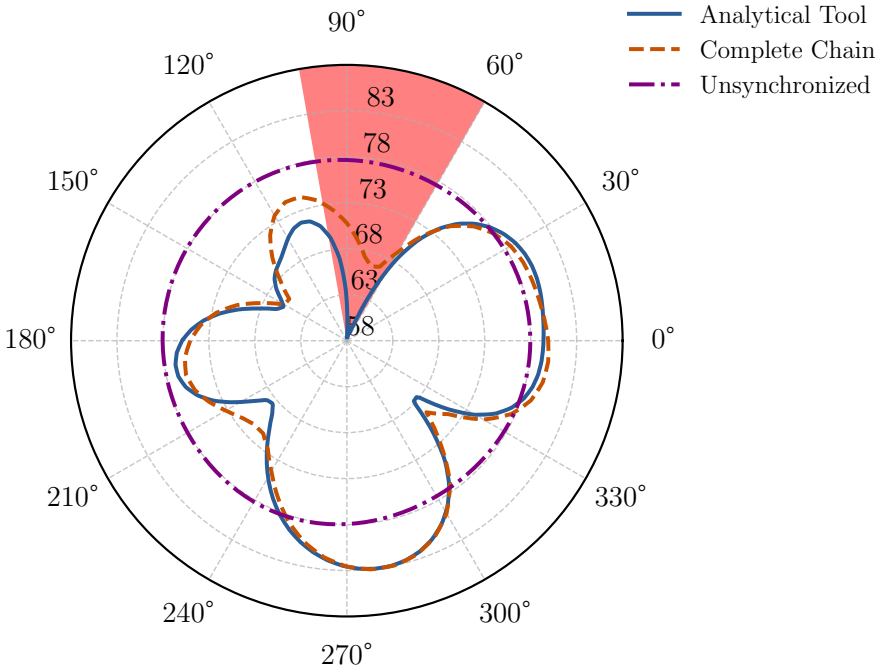


**Figure 5.5.** Comparison of optimization results from the Analytical Tool and Complete Chain against the Unsynchronized case for the Hexarotor configuration. Here, the case for section 3 is shown.

#### 5.3.1.3 Octarotor

| | Rotors | | | | | | | |
|---|---|---|---|---|---|---|---|---|
| Sects. | 1 | 2 | 3 | 4 | 5 | 6 | 7 | 8 |
| 1 | 0 | -14 | -6 | 22 | 43 | -15 | 18 | -3 |
| 2 | 0 | 28 | -13 | 2 | -15 | -18 | 15 | -3 |
| 3 | 0 | 22 | 50 | -22 | 14 | -5 | 1 | -37 |
| 4 | 0 | -33 | 11 | 56 | 5 | 13 | 3 | -13 |
| 5 | 0 | 0 | 0 | 8 | 20 | 10 | 12 | 45 |
| 6 | 0 | 23 | 1 | 0 | 2 | -19 | -4 | -44 |
| 7 | 0 | 0 | -1 | 18 | -3 | 28 | -9 | 15 |
| 8 | 0 | 12 | -16 | -23 | -27 | -39 | 9 | 27 |
| 9 | 0 | -14 | 1 | 2 | 6 | -14 | 18 | -39 |

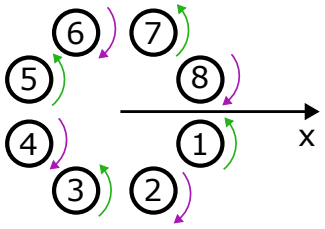


**Table 5.6.** Phase shifts for sound minimization in each section (Octarotor, hemisphere slice)

| Section | 1 | 2 | 3 | 4 | 5 | 6 | 7 | 8 | 9 |
|---|---|---|---|---|---|---|---|---|---|
| UNSYNC | 80.57 | 80.57 | 80.57 | 80.57 | 80.57 | 80.57 | 80.57 | 80.57 | 80.57 |
| CHAIN | 74.01 | 69.87 | 74.26 | 71.37 | 66.14 | 69.56 | 69.27 | 73.81 | 67,32 |

**Table 5.7.** Mean SPL over sections (Unsynchronized Rotors, Complete Chain)

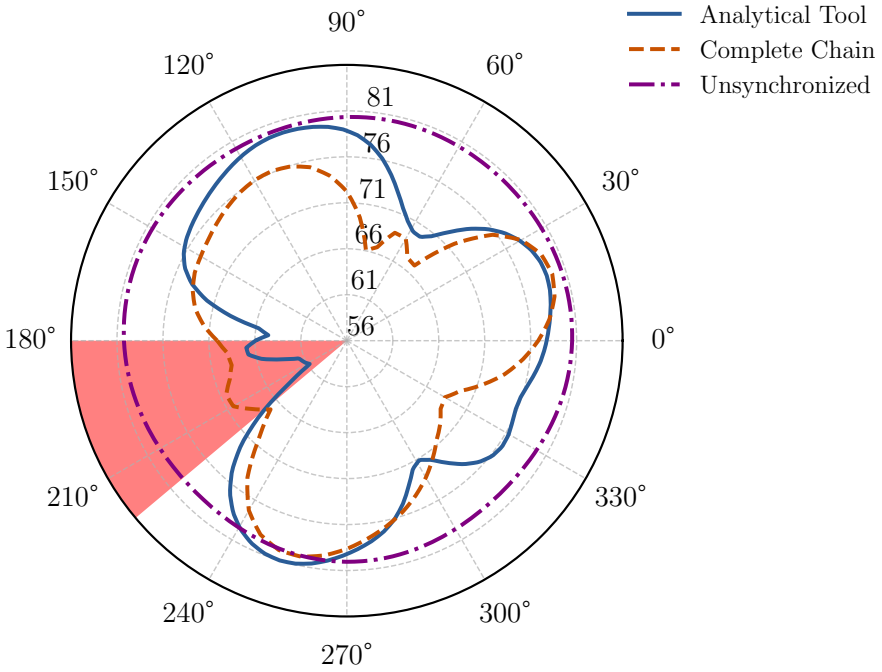


**Figure 5.6.** Comparison of optimization results from the Analytical Tool and Complete Chain against the Unsynchronized case for the Octarotor configuration. Here, the case for section 6 is shown. The light red wedge highlights the section affected by the minimization.

### 5.3.2 Plane portion minimization

#### 5.3.2.1 Quadrotor

| | Rotors | | | |
|---|---|---|---|---|
| Sects. | 1 | 2 | 3 | 4 |
| 1 | 0 | 14 | -86 | -57 |
| 2 | 0 | 37 | 81 | -11 |
| 3 | 0 | -67 | 48 | 75 |
| 4 | 0 | -66 | 42 | 45 |
| 5 | 0 | -24 | 62 | 65 |
| 6 | 0 | 38 | -87 | -75 |
| 7 | 0 | -82 | -66 | -41 |
| 8 | 0 | 63 | -38 | -61 |
| 9 | 0 | -68 | -48 | 12 |

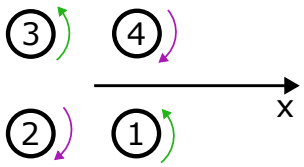


**Table 5.8.** Phase shifts for sound minimization in each section (Quadrotor, plane)

| Section | 1 | 2 | 3 | 4 | 5 | 6 | 7 | 8 | 9 |
|---|---|---|---|---|---|---|---|---|---|
| UNSYNC | 68.5 | 68.5 | 68.5 | 68.5 | 68.5 | 68.5 | 68.5 | 68.5 | 68.5 |
| CHAIN | 60.44 | 62.41 | 57.85 | 59.58 | 61.34 | 62.36 | 58.12 | 57.22 | 59.44 |

**Table 5.9.** Mean SPL over sections (Unsynchronized Rotors, Complete Chain)

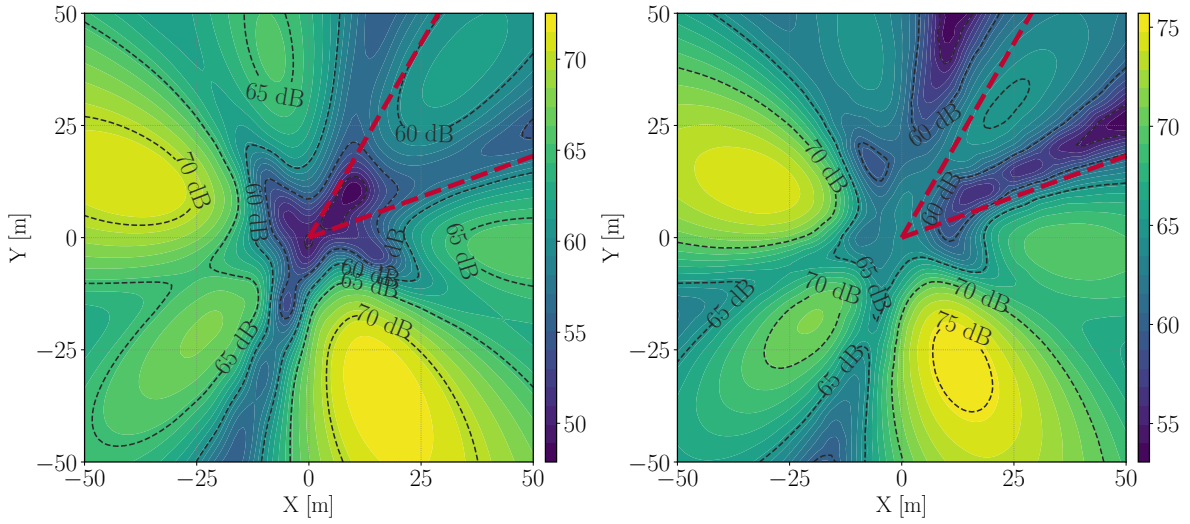


**(a)** Analytical Tool results

**(b)** Complete simulation results

**Figure 5.7.** Comparison of optimization results from the Analytical Tool (a) and the Complete Chain (b) over the plane for the Quadrotor configuration, presenting results for Section 2.

#### 5.3.2.2 Hexarotor

| | Rotors | | | | | |
|---|---|---|---|---|---|---|
| Sects. | 1 | 2 | 3 | 4 | 5 | 6 |
| 1 | 0 | -40 | -41 | -34 | -42 | -70 |
| 2 | 0 | 56 | -28 | -11 | 41 | -23 |
| 3 | 0 | 27 | 41 | 16 | 45 | -29 |
| 4 | 0 | -50 | 22 | -34 | 48 | 69 |
| 5 | 0 | 7 | -27 | -2 | 76 | 64 |
| 6 | 0 | 70 | -2 | -19 | -48 | -37 |
| 7 | 0 | 40 | 19 | -26 | -29 | 29 |
| 8 | 0 | -15 | -40 | -8 | -59 | 36 |
| 9 | 0 | -16 | -51 | -44 | 29 | 54 |

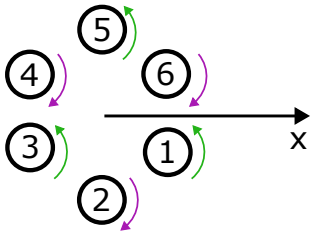


**Table 5.10.** Phase shifts for sound minimization in each section (Hexarotor, plane)

| Section | 1 | 2 | 3 | 4 | 5 | 6 | 7 | 8 | 9 |
|---|---|---|---|---|---|---|---|---|---|
| UNSYNC | 70.78 | 70.78 | 70.78 | 70.78 | 70.78 | 70.78 | 70.78 | 70.78 | 70.78 |
| CHAIN | 63.41 | 59.74 | 61.7 | 60.35 | 61.53 | 62.87 | 60.7 | 60.05 | 60.9 |

**Table 5.11.** Mean SPL over sections (Unsynchronized Rotors, Complete Chain)

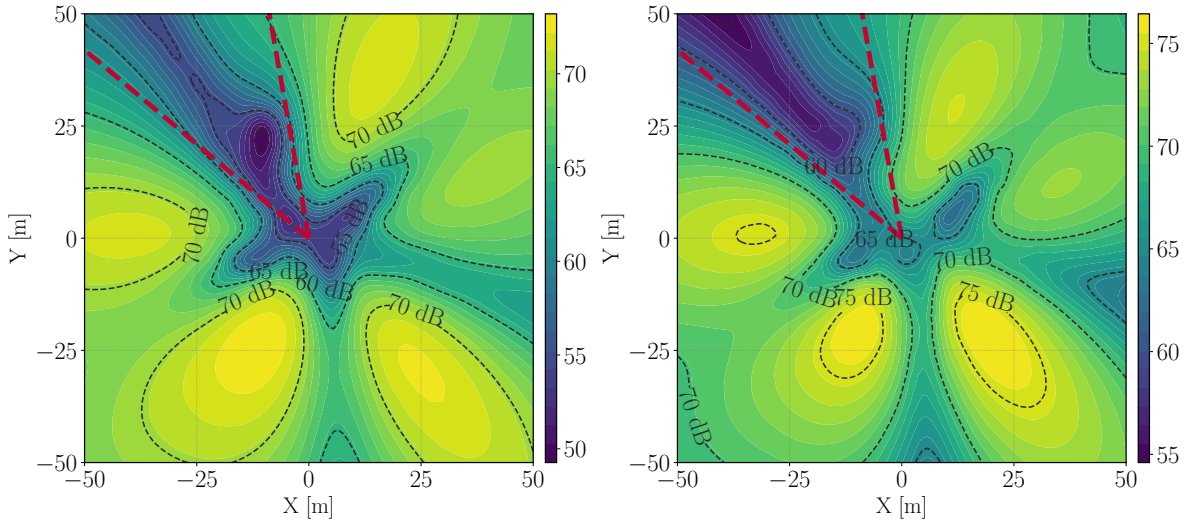


**(a)** Analytical Tool results

**(b)** Complete simulation results

**Figure 5.8.** Comparison of optimization results from the Analytical Tool (a) and the Complete Chain (b) over the plane for the Hexarotor configuration, presenting results for Section 4.

#### 5.3.2.3 Octarotor

| | Rotors | | | | | | | |
|---|---|---|---|---|---|---|---|---|
| Sects. | 1 | 2 | 3 | 4 | 5 | 6 | 7 | 8 |
| 1 | 0 | -13 | -47 | 17 | 45 | 62 | -62 | 25 |
| 2 | 0 | -44 | -60 | 2 | -13 | 16 | 35 | -23 |
| 3 | 0 | -43 | -29 | 35 | 18 | 48 | 26 | -5 |
| 4 | 0 | 23 | 55 | 14 | 27 | -10 | -14 | -20 |
| 5 | 0 | 69 | 33 | 39 | 33 | 23 | 20 | 26 |
| 6 | 0 | 47 | 13 | -9 | -15 | -13 | -26 | -32 |
| 7 | 0 | 48 | 0 | 13 | -24 | -22 | -54 | 41 |
| 8 | 0 | -43 | -52 | -12 | -39 | 44 | 34 | -3 |
| 9 | 0 | 13 | -13 | 15 | -8 | 49 | 37 | 7 |

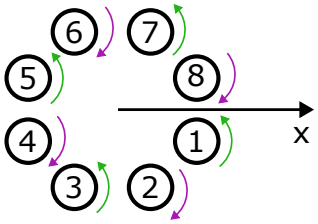


**Table 5.12.** Phase shifts for sound minimization in each section (Octarotor, plane)

| Section | 1 | 2 | 3 | 4 | 5 | 6 | 7 | 8 | 9 |
|---|---|---|---|---|---|---|---|---|---|
| UNSYNC | 70.48 | 70.48 | 70.48 | 70.48 | 70.48 | 70.48 | 70.48 | 70.48 | 70.48 |
| CHAIN | 65.41 | 64.34 | 65.69 | 63.68 | 61.12 | 62.49 | 64.20 | 63.76 | 62.57 |

**Table 5.13.** Mean SPL over sections (Unsynchronized Rotors, Complete Chain)

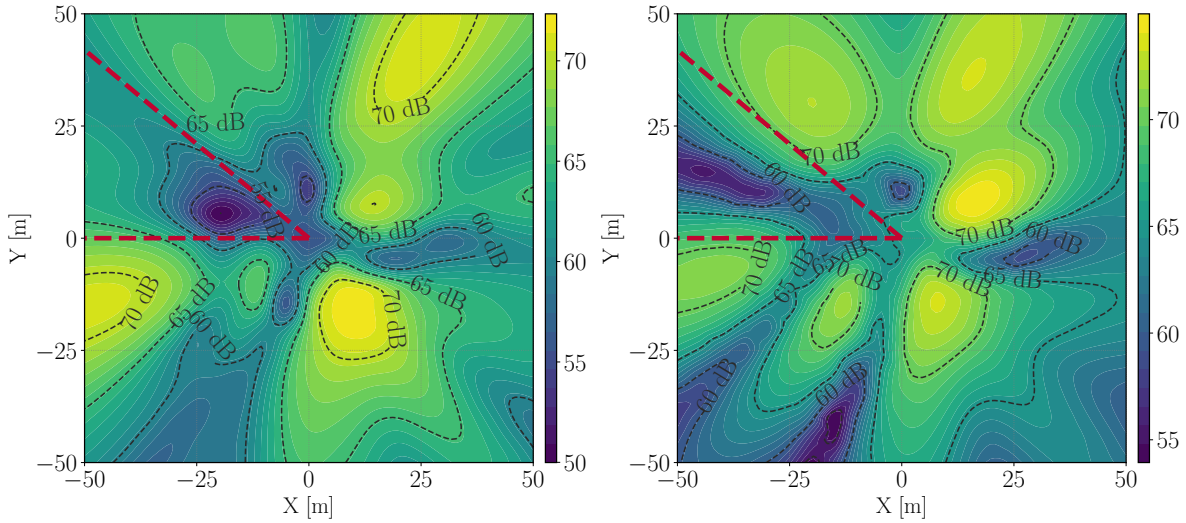


**(a)** Analytical Tool results

**(b)** Complete simulation results

**Figure 5.9.** Comparison of optimization results from the Analytical Tool (a) and the Complete Chain (b) over the plane for the Octarotor configuration, presenting results for Section 5.

# Conclusions

This thesis has presented the development and validation of an analytical tool for the rapid simulation of sound directivity and active noise control strategies for multicopter configurations. Driven by the increasing prominence of Urban Air Mobility (UAM) and Electric Vertical Take-Off and Landing (eVTOL) vehicles, and the critical challenge of noise reduction in urban environments, this work aimed to address the need for computationally efficient methods to predict and mitigate the acoustic impact of these aircraft.

The core of this research lies in the creation of a Python-based analytical tool. Recognizing the time-intensive nature of high-fidelity aeroacoustic simulations, a simplified approach was adopted, leveraging analytical formulations derived from a dicretization of the Ffowcs-Williams-Hawkings (FW-H) equations. A key simplification was the representation of each rotor blade's sound emission as a single point source located at the blade tip. This simplification, while inherently reducing the fidelity of the model compared to distributed source or CFD-based approaches, offers a significant advantage in terms of computational speed. This speed is crucial for enabling rapid design iterations, parametric studies, and the integration with optimization algorithms for active noise control.

The validation of this analytical tool was a very important step in establishing its credibility and range of applicability. The thesis compared the tool's predictions against experimental data from a NASA publication, as well as simulation results from APSIM. This validation approach provides a strong foundation for confidence in the tool's capabilities, at least within the scope of its simplified model. The overall process confirms the tool's ability to capture the fundamental trends in sound directivity for multicopter configurations even if not always matching the real absolute values. But the level of qualitatively agreement observed suggests us that this tool can be used in a profitable manner for the design of noise reduction strategies.

A significant contribution of this thesis is the integration of the analytical tool with a genetic algorithm (GA) for active noise cancellation through rotor phase shift control. Rotor phasing, the relative timing of rotation between rotors, offers a promising possibility for manipulating the overall sound field and achieving targeted noise reduction. The GA, a robust optimization technique inspired by natural selection, was chosen for its ability to explore complex, multi-dimensional parameter spaces and identify optimal solutions, even in the presence of non-linearities and discontinuous behavior. The thesis successfully demonstrates the application of this GA-driven phase shift control strategy to minimize noise in specific target directions, such as downward noise towards the ground or away from sensitive areas.

The results presented in the last chapter and in the appendices show the effectiveness of the developed active noise control strategy for different multicopter configurations (quadrotor, exarotor, octarotor). By optimizing the rotor phases, significant reductions in sound pressure level (SPL) were achieved in the targeted regions, both on a hemispherical slice and a horizontal plane below the multicopter. The comparison between the analytical tool and a "complete" simulation, further reinforces the reliability

and consistency of the analytical tool's predictions. The plots presented in the appendices visually and qualitatively demonstrate the potential of phase shift control to reshape the sound directivity pattern and achieve substantial noise mitigation.

While this thesis successfully demonstrates the capabilities of the developed analytical tool and the effectiveness of the GA-based phase shift control strategy, it is important to acknowledge the inherent limitations of the simplified model. The point source representation of rotor blades neglects complex aerodynamic phenomena and distributed noise sources. Furthermore, the analytical tool, in its current form, does not account for aerodynamic interferences between rotors, which can become significant in not classical multicopter configurations or in operational condition different from the hover, such as in forward flight.

Future work should focus on addressing these limitations and further expanding the capabilities of the analytical tool. Incorporating more sophisticated aeroacoustic models, potentially including distributed source representations or hybrid analytical-numerical approaches, could enhance the accuracy of the predictions. Investigating the impact of aerodynamic rotor-rotor interactions and incorporating these effects into the model would improve its fidelity for complex multicopter designs. Experimental validation of the phase shift control strategies, using physical prototypes and acoustic measurements, is a crucial next step to translate the simulation results into real-world noise reduction benefits.

Furthermore, the computational efficiency of the analytical tool opens up possibilities for real-time noise control applications. Future research could explore the development of adaptive control systems that dynamically adjust rotor phases based on real-time noise measurements and environmental conditions. This could lead to even more effective and adaptable noise mitigation strategies for eVTOLs and other multicopter applications.

In conclusion, I hope that the findings of this thesis could contribute to the growing body of knowledge in UAM technology and pave the way for quieter and more socially acceptable urban air mobility vehicles.

# Bibliography


[1] "Multirotor drone flying experience | lift aircraft — liftaircraft.com. "[Online]. Available: https://www.liftaircraft.com.

[2] T. Dolzall. "Uam snapshot - beta technologies alia - flight plan — flightplan.forecastinternational.com. "[Online]. Available: https://flightplan.forecastinternational.com/2024/06/25/uam-snapshot-beta-technologies-alia/.

[3] "Jaunt air mobility plans to fly electric demonstrator in 2023 — aerospaceamerica.aiaa.org. "[Online]. Available: https://aerospaceamerica.aiaa.org/jaunt-air-mobility-plans-to-fly-electric-demonstrator-in-2025/.

[4] "Vertical's vx4 evtol prototype crashes during test flight — verticalmag.com. "[Online]. Available: https://verticalmag.com/news/verticals-vx4-evtol-prototype-crashes-during-test-flight/.

[5] E. Greenwood, "Fundamental rotorcraft acoustic modeling from experiments (frame)," Jan. 2011.

[6] J. D. D. Boyd, "Discussion of rotorcraft and evtol noise," Mar. 2022. [Online]. Available: https://ntrs.nasa.gov/citations/20220003126.

[7] "Ascendance | where innovation takes flight — ascendance-ft.com." [Accessed 27-02-2025]. [Online]. Available: https://www.ascendance-ft.com.

[8] P. Beaumier et al., "From erato basic research to the blue edge™ rotor blade: An example of virtual engineering," in *Rotorcraft Virtual Engineering Conference*, Liverpool, United Kingdom, Nov. 2016. [Online]. Available: https://hal.science/hal-01413109v1/file/DAAP16048.1477058023.pdf.

[9] "Volocopter volocity - evtol design and development." [Accessed 27-02-2025]. [Online]. Available: https://evtol.news/volocopter-volocity/.

[10] V. T. Valente, E. Greenwood, and E. N. Johnson, "An experimental evaluation of an electronic rotor phase synchronization system for multirotor aircraft noise control," in *Vertical Flight Society 80th Annual Forum & Technology Display*, Montreal, Quebec, Canada, May 2024. [Online]. Available: https://proceedings.vtol.org/80/acoustics/an-experimental-evaluation-of-an-electronic-rotor-phase-synchronization-system-for-multirotor-aircraft-noise-control.

[11] J. Delfs, "Grundlagen der aeroakustik (basics of aeroacoustics)," Technische Universität Braunschweig, Institut für Aerodynamik und Strömungstechnik, Abteilung Technische Akustik, DLR – Deutsches Zentrum für Luft- und Raumfahrt e.V., Lilienthalplatz 7, 38108 Braunschweig, Germany, Lecture Notes WiS 2022/2023, Oct. 2022, Lecture notes for Grundlagen der Aeroakustik (Basics of Aeroacoustics) course at Technische Universität Braunschweig.

[12] O. Gur and A. Rosen, "Design of quiet propeller for an electric mini unmanned air vehicle," *Journal of Propulsion and Power*, vol. 25, no. 3, pp. 717–728, May 2009. DOI: 10.2514/1.38814. [Online]. Available: https://arc.aiaa.org/doi/10.2514/1.38814.

[13] P. Kunze, K.-S. Rossignol, L. Rottmann, and T. Schwarz, "A panel free-wake code with boundary layer method for helicopter simulations," in *45th European Rotorcraft Forum*, ERF2019-0114, Accessed via OCR from uploaded PDF, European Rotorcraft Forum (ERF), Warsaw, Poland, Sep. 2019.

[14] J. Yin, F. Le Chuiton, M. Schmid, and T. Schwarz, "Dlr free wake unsteady panel method (upm) user guide," Institute of Aerodynamics and Flow Technology, DLR, User Guide, version DRAFT, n.d., Accessed via OCR from uploaded PDF, publication year not explicitly stated.

[15] J. Yin, *Apsim training – part 1: Theory and application*, Online Session, DLR-AS, Accessed via OCR from uploaded PDF, Mar. 2022.

[16] G. Wilke, H. Lüdeke, J. Yin, and J. Delfs, "Prediction of acoustic far field with dlr's acoustic code apsim+," DLR, User Handbook, Apr. 2021, Accessed via OCR from uploaded PDF.

[17] N. H. Schiller, K. A. Pascioni, and N. S. Zawodny, "Tonal noise control using rotor phase synchronization," in *Vertical Flight Society Annual Forum and Technology Display (VFS Forum 75)*, 2019.

[18] P. D.-I. J. Delfs, *Gliederung der vorlesung „methoden der aeroakustik"*, https://www.tu-braunschweig.de/, Sommersemester 2022, TU Braunschweig, 2022.

[19] F. Sessini, *Numerical aeroacoustic investigation of the phase shift method for multirotor directional noise reduction*, Alma Mater Studiorum Università di Bologna, a.y. 2023/24, 2023.

[20] D. Donnini, *Vtol directional noise reduction via rotor phase synchronization: A numerical trim procedure and flight mechanics investigation*, Alma Mater Studiorum Università di Bologna, a.y. 2023/24, 2023.

[21] M. K. Heris, *Practical genetic algorithms in python and matlab – video tutorial*, https://yarpiz.com/632/ypga191215-practical-genetic-algorithms-in-python-and-matlab, Yarpiz, 2020.

[22] V. Ahuja, D. S. Little, J. Majdalani, and R. J. Hartfield, "On the prediction of noise generated by urban air mobility (uam) vehicles. ii. implementation of the farassat f1a formulation into a modern surface-vorticity panel solver," *Physics of Fluids*, vol. 34, no. 11, p. 116 118, 2022. DOI: 10.1063/5.0105002.

[23] D. S. Little, J. Majdalani, R. J. Hartfield, and V. Ahuja, "On the prediction of noise generated by urban air mobility (uam) vehicles. i. integration of fundamental acoustic metrics," *Physics of Fluids*, vol. 34, no. 11, p. 116 117, 2022. DOI: 10.1063/5.0124134.

[24] I. M. Gregory, "Urban air mobility: A control-centric approach to addressing technical challenges," in *FORCE Seminar (Forum On Robotic and Control Engineering)*, Presentation slides, NASA, May 2021.

[25] P. C. Murphy, P. G. Buning, and B. M. Simmons, "Rapid aero modeling for urban air mobility aircraft in computational experiments," in *AIAA SciTech 2021 Forum*, Jan. 2021.

[26] K. A. Ackerman and A. M. Patterson, "Acoustically-aware vehicles: Control driven noise reduction for urban air mobility," in *Aerospace Control and Guidance Systems Committee Meeting*, Mar. 2021.

[27] K. S. Brentner, "Modeling aerodynamically generated sound: Recent advances in rotor noise prediction," in *38th Aerospace Sciences Meeting & Exhibit*, AIAA 2000-0345, American Institute of Aeronautics and Astronautics, Reston, VA, Jan. 2000. [Online]. Available: https://arc.aiaa.org/doi/10.2514/6.2000-345.

[28] C. L. Morfey, "Rotating blades and aerodynamic sound," *Journal of Sound and Vibration*, vol. 28, no. 3, pp. 587–617, 1973.

[29] M. V. Lowson, "The sound field for singularities in motion," Wyle Laboratories, Huntsville Facility, Tech. Rep. WR 64-10, Dec. 1964, Also includes results of research conducted at the Institute of Sound and Vibration, Southampton, England, and research under Contract NAS 8-5384 and NAS 8-11308.

[30] J. E. Ffowcs Williams and D. L. Hawkings, "Sound generated by turbulence and surfaces in arbitrary motion," *Philosophical Transactions of the Royal Society of London*, A, vol. 264, pp. 321–342, 1969.

[31] P. M. Morse and K. U. Ingard, *Theoretical Acoustics*. New York: McGraw-Hill Book Co., 1968.

[32] F. Farassat, "The acoustic far-field of rigid bodies in arbitrary motion," *Journal of Sound and Vibration*, vol. 32, no. 3, pp. 387–405, 1974. DOI: 10.1016/S0022-460X(74)80159-4.

[33] F. Farassat, "Discontinuities in aerodynamics and aeroacoustics: The concept and application of generalized derivatives," *Journal of Sound and Vibration*, vol. 55, pp. 165–193, 1977.

[34] F. Farassat, "Theory of noise generation from moving bodies with an application to helicopter rotors," NASA, Tech. Rep. TR R-451, 1975.

[35] D. L. Hawkings and M. V. Lowson, "Theory of open supersonic rotor noise," *Journal of Sound and Vibration*, vol. 36, pp. 1–20, 1974.

[36] D. B. Hanson, "Near field noise of high tip speed propellers in forward flight," in *AIAA Paper 76-565*, 1976.

[37] F. Farassat and T. J. Brown, "A new capability for predicting helicopter rotor and propeller noise including the effect of forward motion," NASA, Tech. Rep. TM X-74037, 1977.

[38] F. Farassat and G. P. Succi, "A review of propeller discrete frequency noise prediction technology with emphasis on two current methods for time domain calculations," *Journal of Sound and Vibration*, vol. 71, no. 3, pp. 399–419, 1980.

[39] F. Farassat, "Introduction to generalized functions with applications in aerodynamics and aeroacoustics," NASA Langley Research Center, Tech. Rep. NASA Technical Paper 3428, May 1994, Corrected Copy (April 1996). [Online]. Available: https://ntrs.nasa.gov/citations/19940024546.

[40] P. A. Nystrom and F. Farassat, "A numerical technique for calculation of the noise of high speed propellers with advanced geometry," NASA, Tech. Rep. TP 1662, 1980.

[41] C. J. Woan and G. M. Gregorek, "The exact numerical calculation of propeller noise," in *AIAA Paper 78-1122*, 1978.

[42] M. P. Isom, "The theory of sound radiated by a hovering transonic helicopter blade," Polytechnic Institute of New York, Tech. Rep. Poly-AE/AM No. 75-4, 1975.

[43] F. Farassat, "The derivation of a thickness noise formula for the far-field by isom," *Journal of Sound and Vibration*, vol. 64, no. 1, pp. 159–160, 1979.

[44] F. Farassat, "Extension of isom's thickness noise formula to the near field," *Journal of Sound and Vibration*, vol. 67, no. 2, pp. 280–281, 1979.

[45] F. Farassat and P. A. Nystrom, "Isom's thickness noise formula for rotating blades with finite thickness at the tip," *Journal of Sound and Vibration*, vol. 72, pp. 550–553, 1980.

[46] G. P. Succi, "Design of quiet efficient propellers," in *SAE Paper 790584*, 1979.

[47] M. V. Lowson, "The sound field of singularities in motion," *Proceedings of the Royal Society of London*, A, vol. 286, pp. 559–572, 1965.

[48] R. A. Arnoldi, "Propeller noise caused by blade thickness," United Aircraft Corp. Research Department Rept. R-0896-1, Tech. Rep., 1956.

[49] D. B. Hanson, "The influence of propeller design parameters on far-field harmonic noise in forward flight," in *AIAA Paper 79-0609*, 1979.

[50] W.-H. Jou, "Supersonic propeller noise in a uniform flow," in *AIAA Paper 79-0348*, 1979.

[51] I. E. Garrick and C. E. Watkins, "A theoretical study of the effects of forward speed on the free-space sound-pressure field around propellers," NACA, Tech. Rep. TR 1198, 1954.

[52] G. Mall and F. Farassat, "A computer program for the determination of the acoustic pressure signature of helicopter rotors due to blade thickness," NASA, Tech. Rep. TM X-3323, 1976.

[53] H. Hubbard, "Propeller noise charts for transport airplanes," NACA, Tech. Rep. TN 2968, 1953.

[54] D. A. Russell, J. P. Titlow, and Y.-J. Bemmen, "Acoustic monopoles, dipoles, and quadrupoles: An experiment revisited," *American Journal of Physics*, vol. 67, no. 8, pp. 660–664, Aug. 1999. DOI: 10.1119/1.19349.

[55] F. Farassat, "Linear acoustic formulas for calculation of rotating blade noise," *AIAA Journal*, vol. 19, no. 9, pp. 1122–1130, 1981.

[56] K. S. Brentner, *A superior kirchhoff method for aeroacoustic noise prediction: The ffowcs williams–hawkings equation*, Conference Paper, San Diego, CA, Dec. 1997.

[57] Wikibooks, *Aeroacoustics/acoustic sources*, Accessed: 2023-10-27, 2020. [Online]. Available: https://en.wikibooks.org/wiki/Aeroacoustics/Acoustic_Sources.

[58] S. Rienstra and A. Hirschberg, "An introduction to acoustics," Eindhoven University of Technology, Tech. Rep., Aug. 2018, Extended and revised edition of IWDE 92-06.

[59] M. Shao, Y. Lu, X. Xu, S. Guan, and J. Lu, "Experimental study on noise reduction of multi-rotor by phase synchronization," *Journal of Sound and Vibration*, vol. 539, p. 117 199, 2022. DOI: 10.1016/j.jsv.2022.117199.

[60] H. H. Hubbard, Ed., *Aeroacoustics of Flight Vehicles: Theory and Practice. Volume 1: Noise Sources*. NASA, 1991, NASA Reference Publication 1258, Volume 1.

[61] H. H. Hubbard, Ed., *Aeroacoustics of Flight Vehicles: Theory and Practice. Volume 2: Noise Control*. NASA, 1991, NASA Reference Publication 1258, Volume 2.

[62] A. Patterson, A. Gahlawat, and N. Hovakimyan, "Propeller phase synchronization for small distributed electric vehicles," in *AIAA Scitech 2019 Forum*, American Institute of Aeronautics and Astronautics, 2019. DOI: 10.2514/6.2019-1458.

[63] A. Patterson, K. A. Ackerman, A. Gahlawat, N. Hovakimyan, N. H. Schiller, and I. Gregory, "Controller design for propeller phase synchronization with aeroacoustic performance metrics," in *AIAA Scitech 2020 Forum*, American Institute of Aeronautics and Astronautics, vol. 1.F, 2020. DOI: 10.2514/6.2020-1494.

[64] V. T. Valente, E. Johnson, and E. Greenwood, "Implementation of a phase synchronization algorithm for multirotors uavs," in *2022 IEEE/AIAA 41st Digital Avionics Systems Conference (DASC)*, IEEE, 2022, pp. 1–8. DOI: 10.1109/DASC55683.2022.9925771.

[65] E. Alvarez, A. Schenk, T. Critchfield, and A. Ning, "Rotor-on-rotor aeroacoustic interactions of multirotor in hover," in *AIAA Scitech 2020 Forum*, American Institute of Aeronautics and Astronautics, 2020. DOI: 10.2514/6.2020-2832.

[66] G. Sinibaldi and L. Marino, "Experimental analysis on the noise of propellers for small UAV," *Applied Acoustics*, vol. 74, no. 1, pp. 79–88, 2013. DOI: 10.1016/j.apacoust.2012.06.011.

# A Hemisphere Minimization

## A.1 Quadrotor

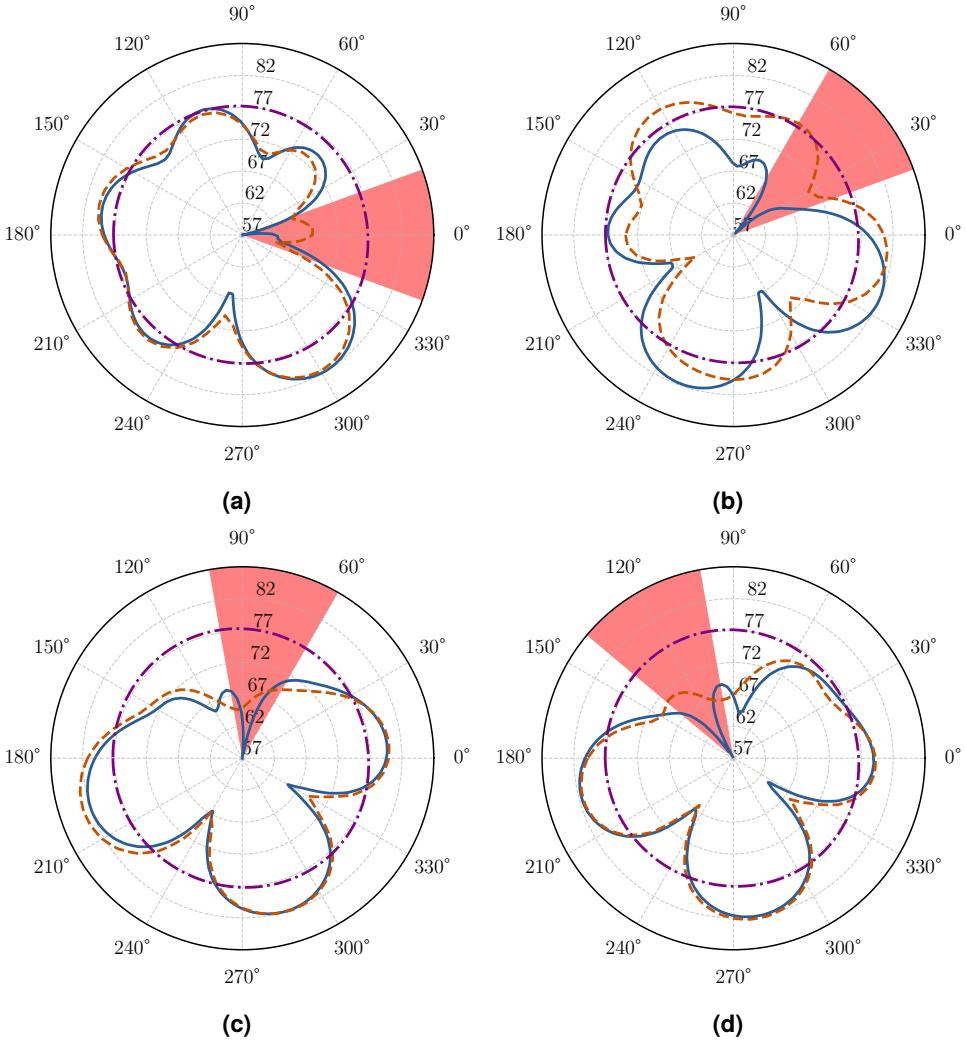

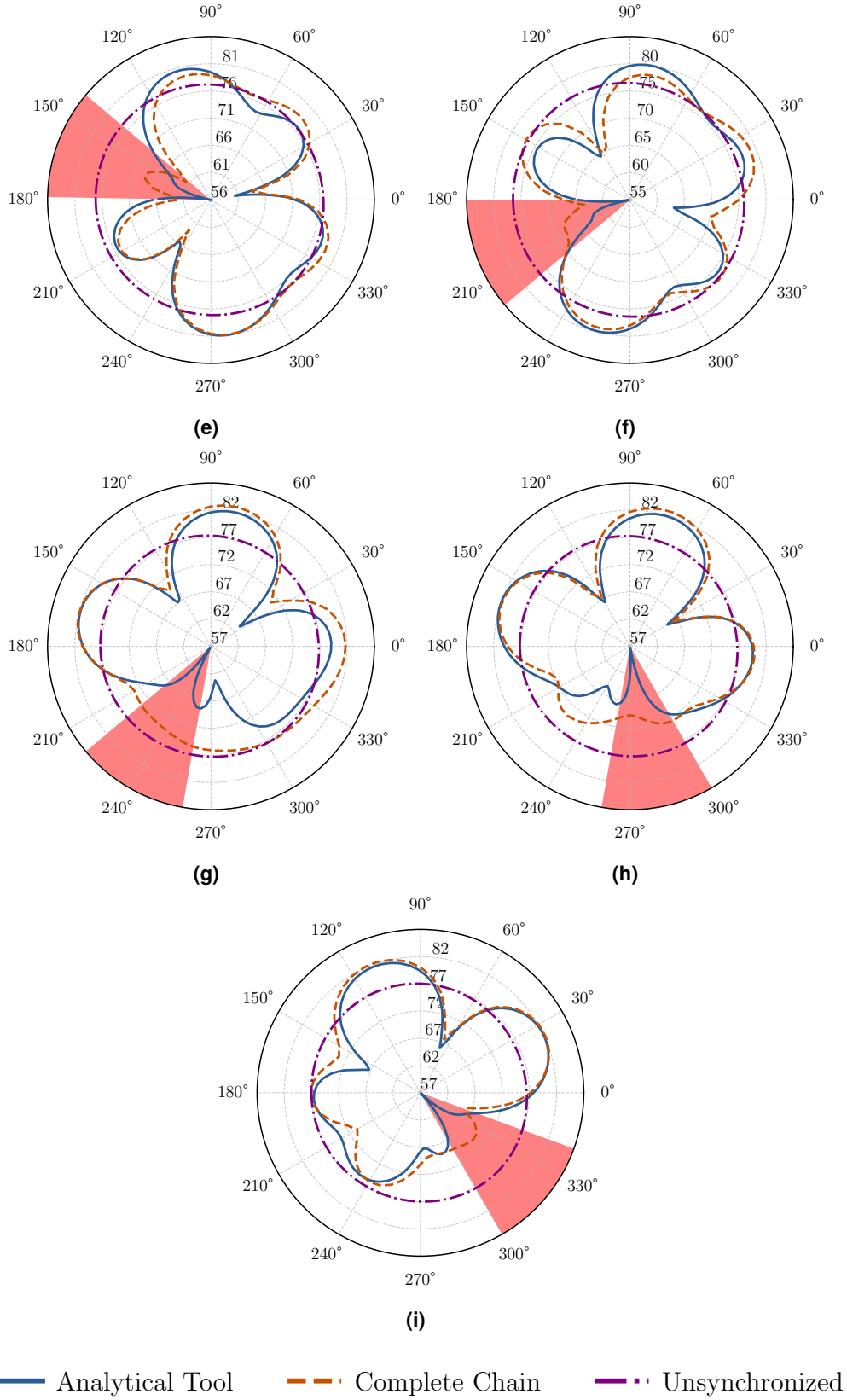


**Figure A.1.** Comparison of optimization results from the Analytical Tool and Complete Chain against the Unsynchronized case for the Quadrotor configuration. Each image represents the optimization results for different sections around the multirotor. The light red wedge highlights the section affected by the minimization.

## A.2 Hexarotor

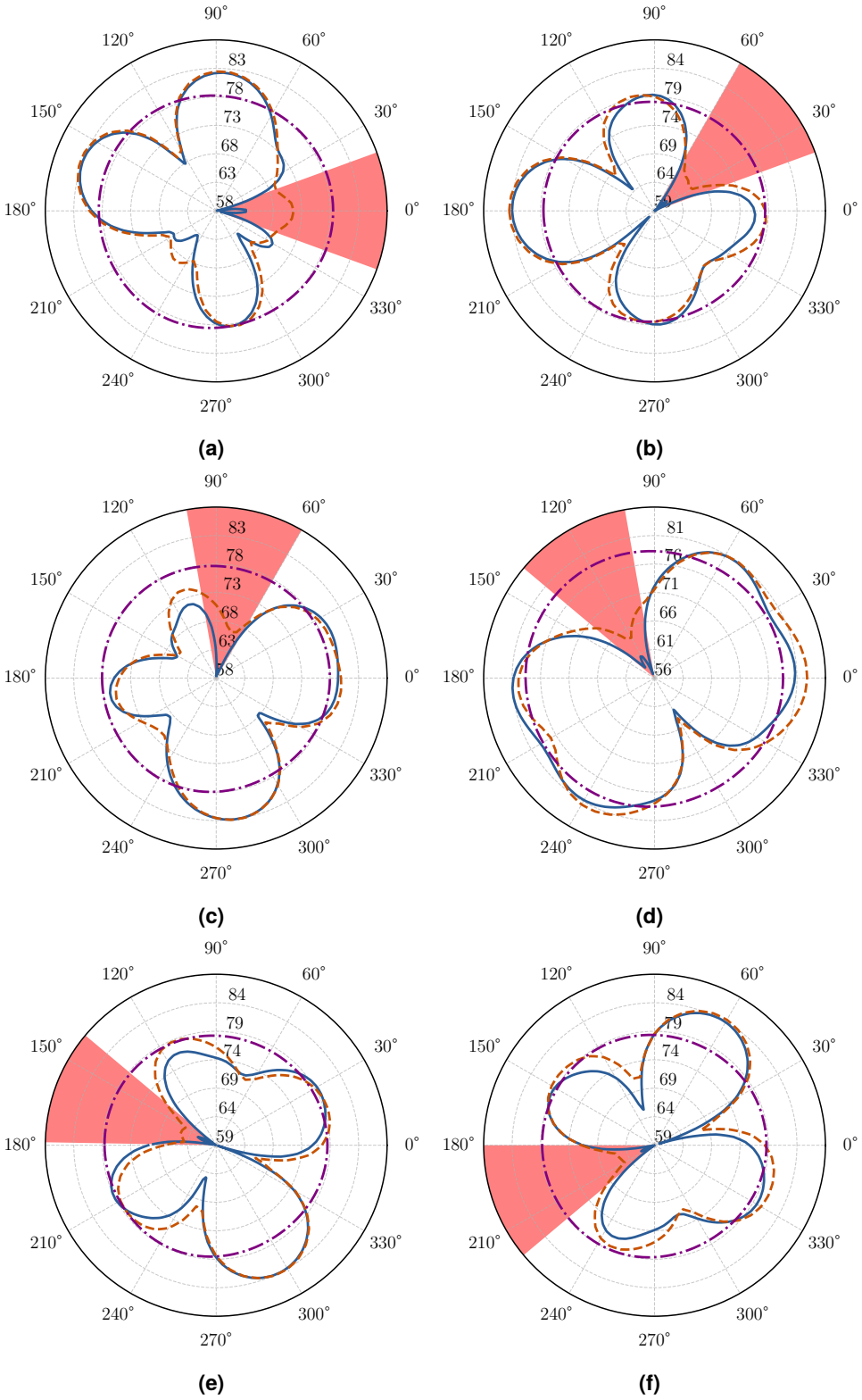

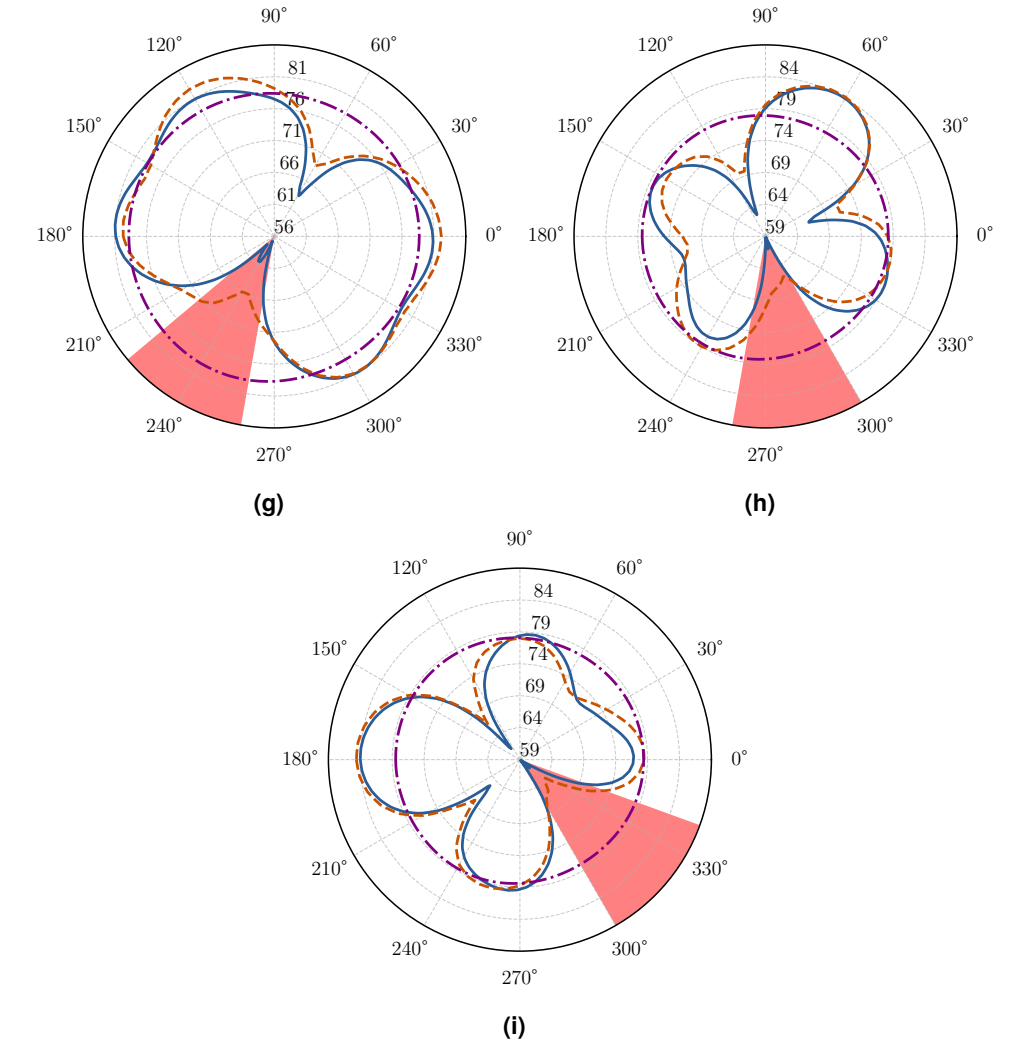


**Figure A.2.** Comparison of optimization results from the Analytical Tool and Complete Chain against the Unsynchronized case for the Hexarotor configuration. Each image represents the optimization results for different sections around the multirotor. The light red wedge highlights the section affected by the minimization.

## A.3 Octarotor

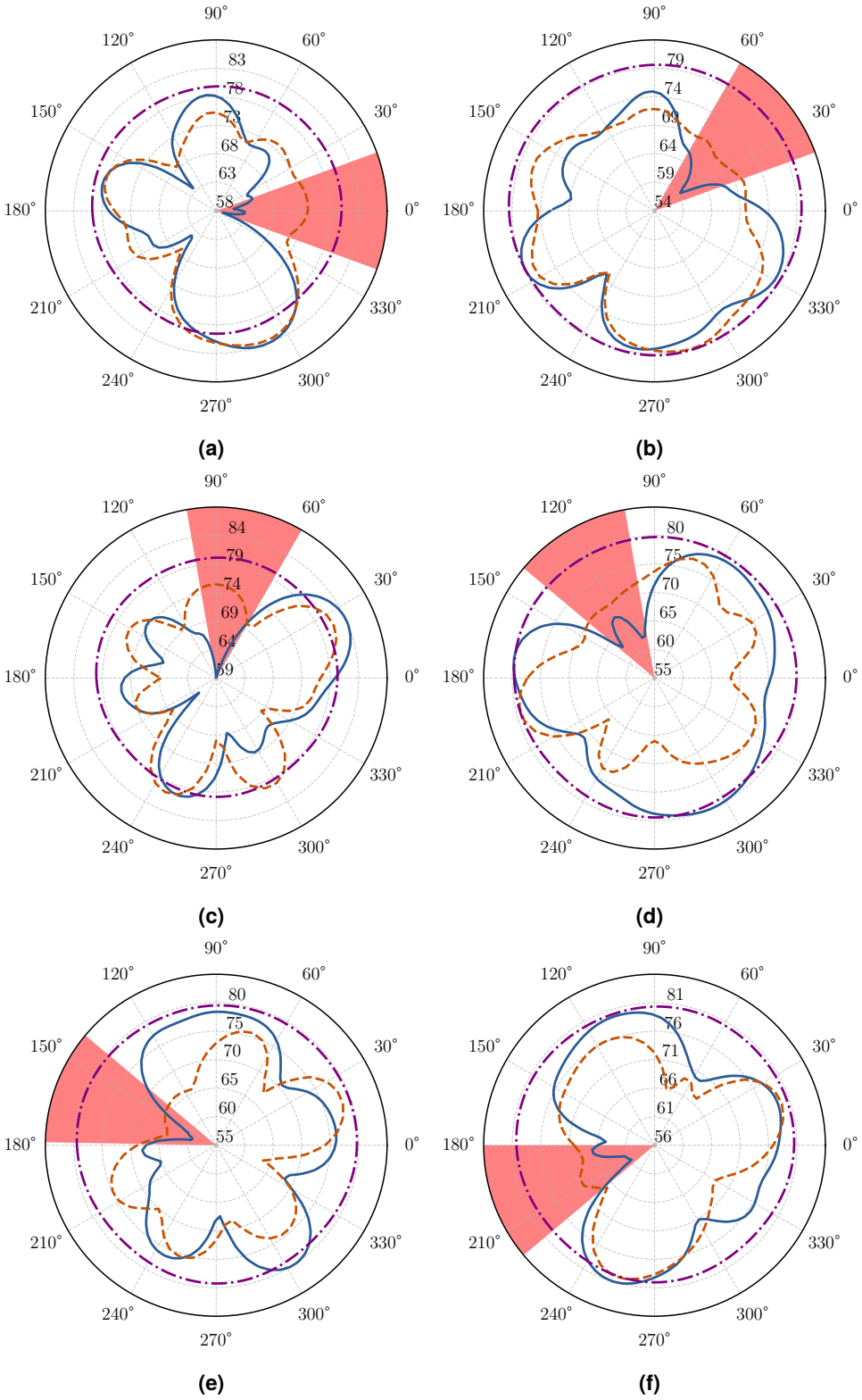

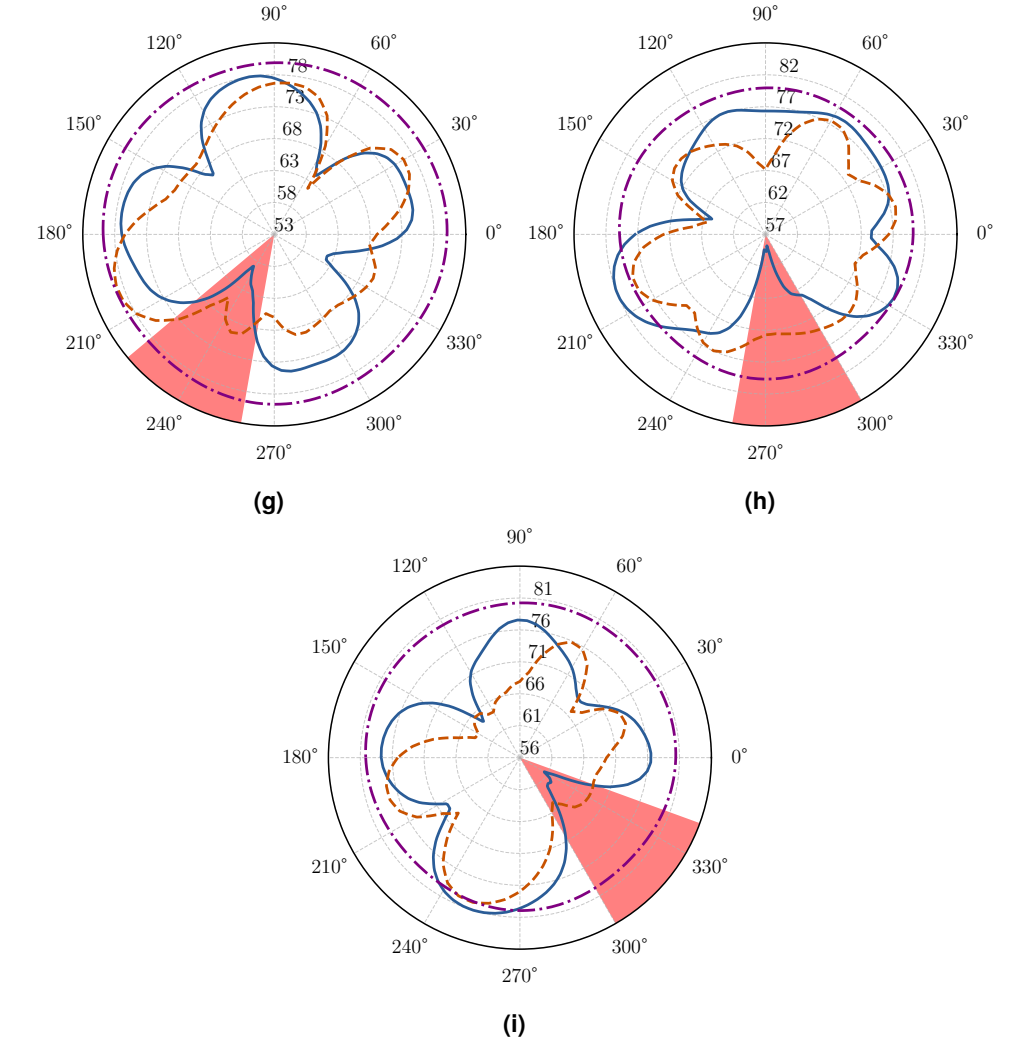


**Figure A.3.** Comparison of optimization results from the Analytical Tool and Complete Chain against the Unsynchronized case for the Octarotor configuration. Each image represents the optimization results for different sections around the multirotor. The light red wedge highlights the section affected by the minimization.

# B | Plane Minimization

## B.1 Quadrotor

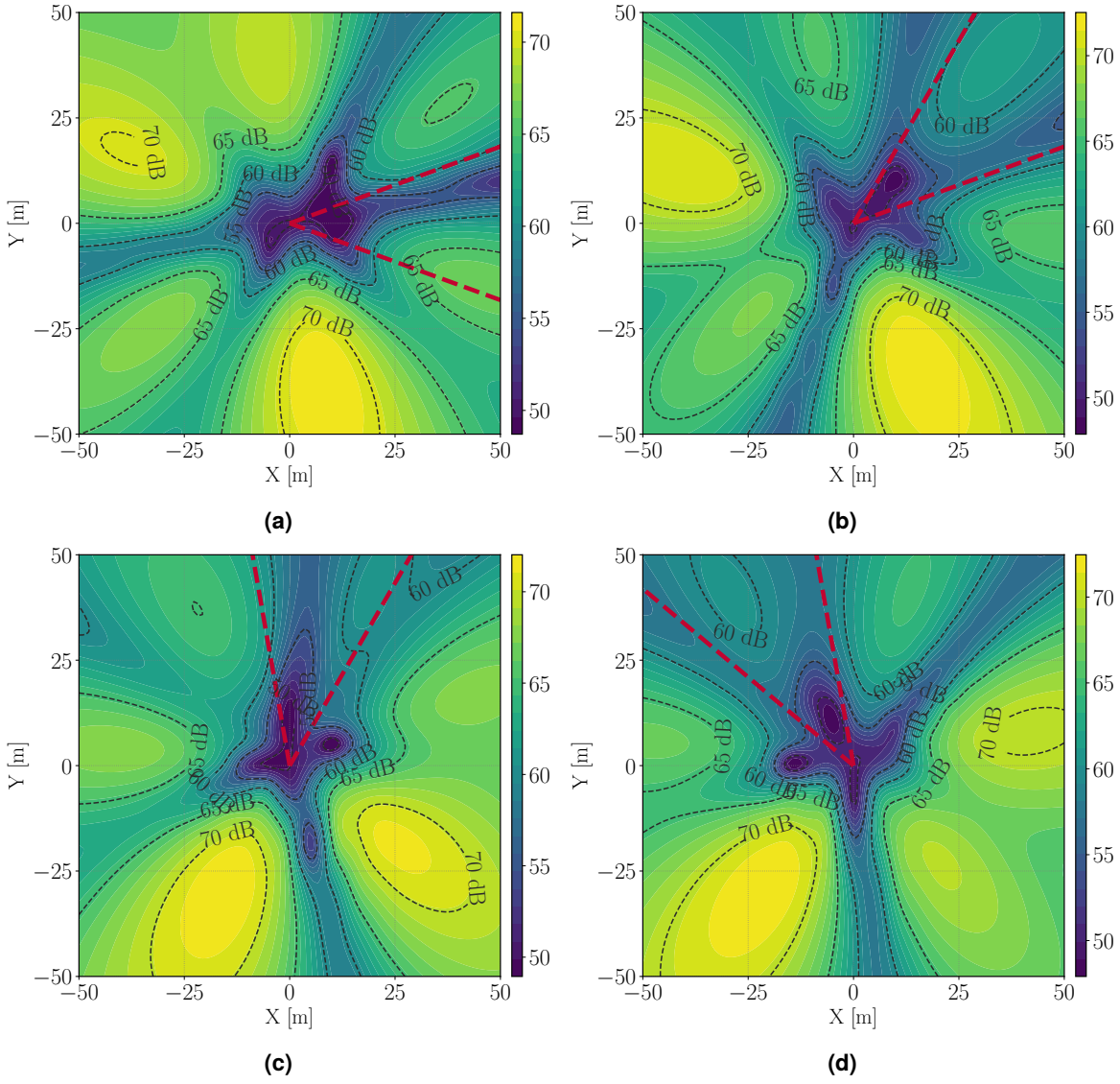

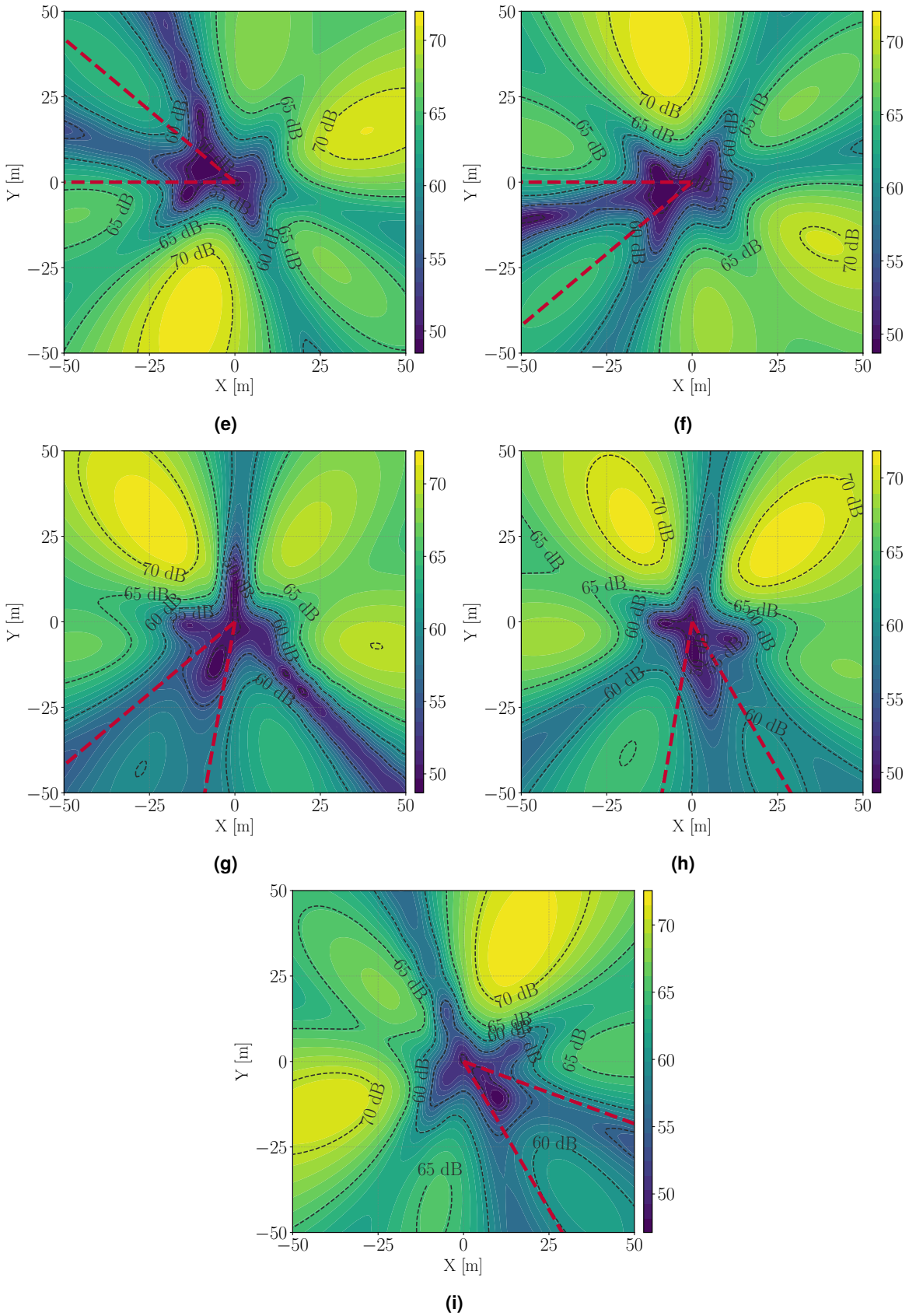


**Figure B.1.** Analytical Tool optimization results over the plane for the Quadrotor configuration, presented for all sections.

## B.2 Hexarotor

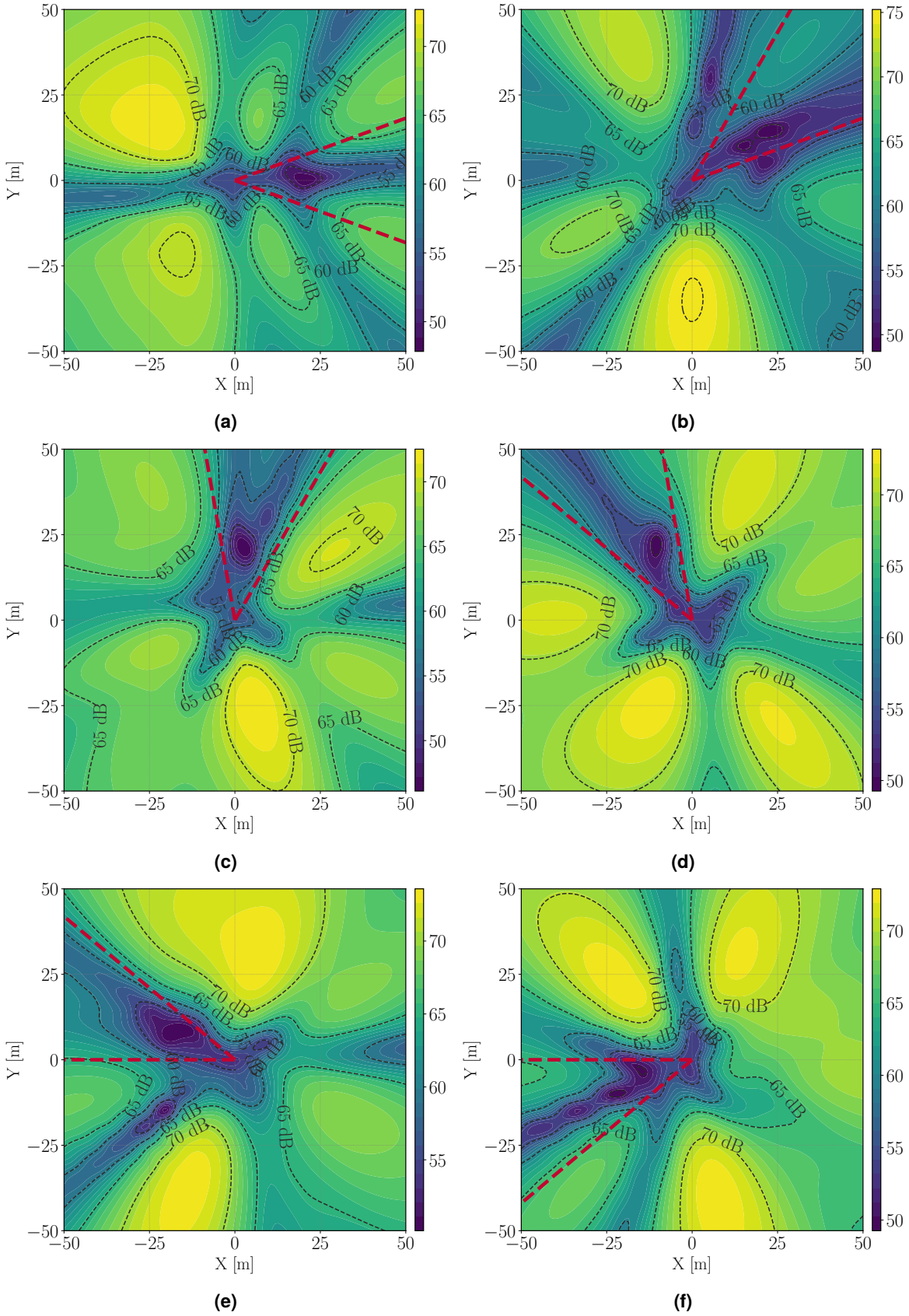

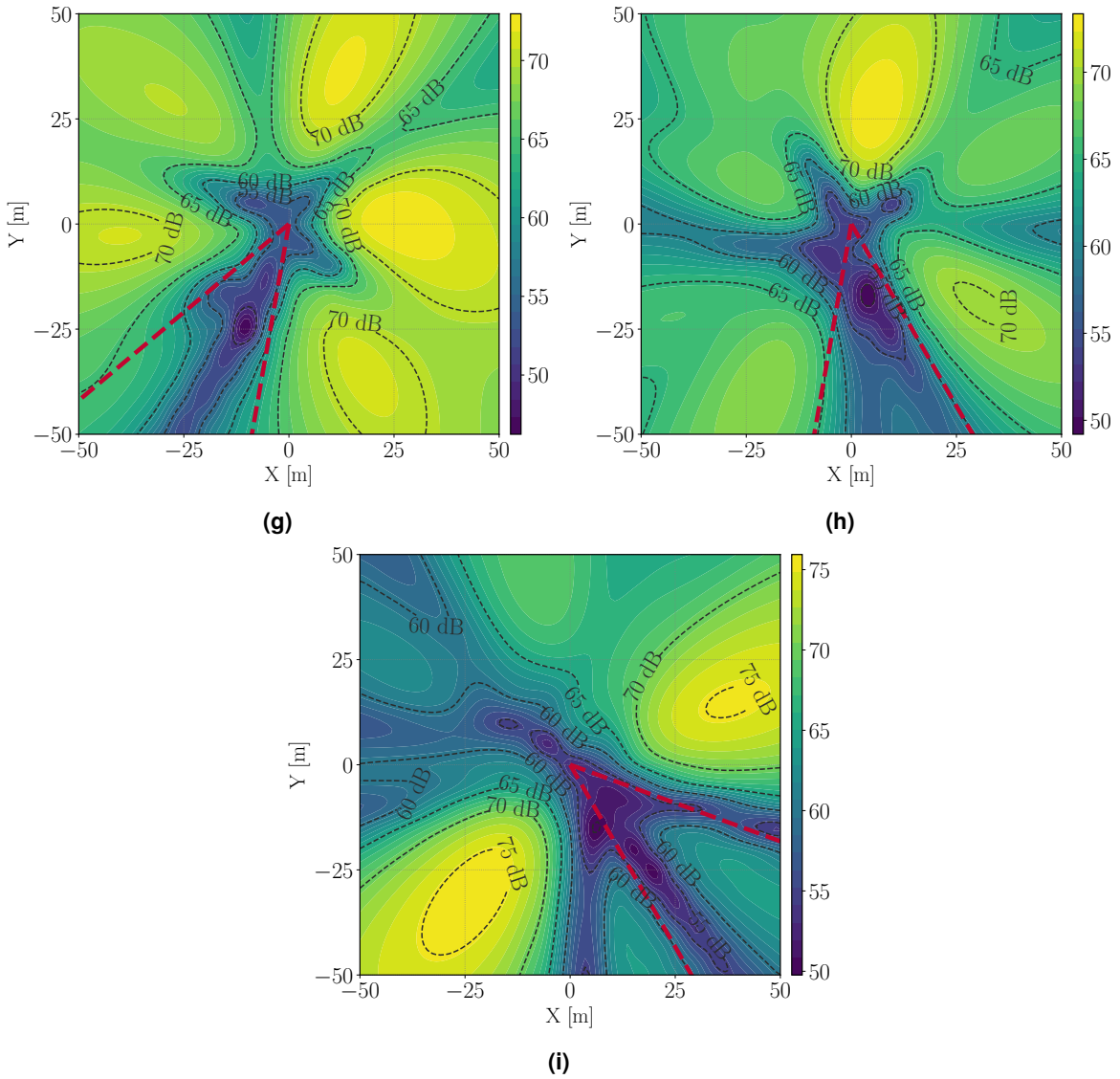


**Figure B.2.** Analytical Tool optimization results over the plane for the Hexarotor configuration, presented for all sections.

## B.3 Octarotor

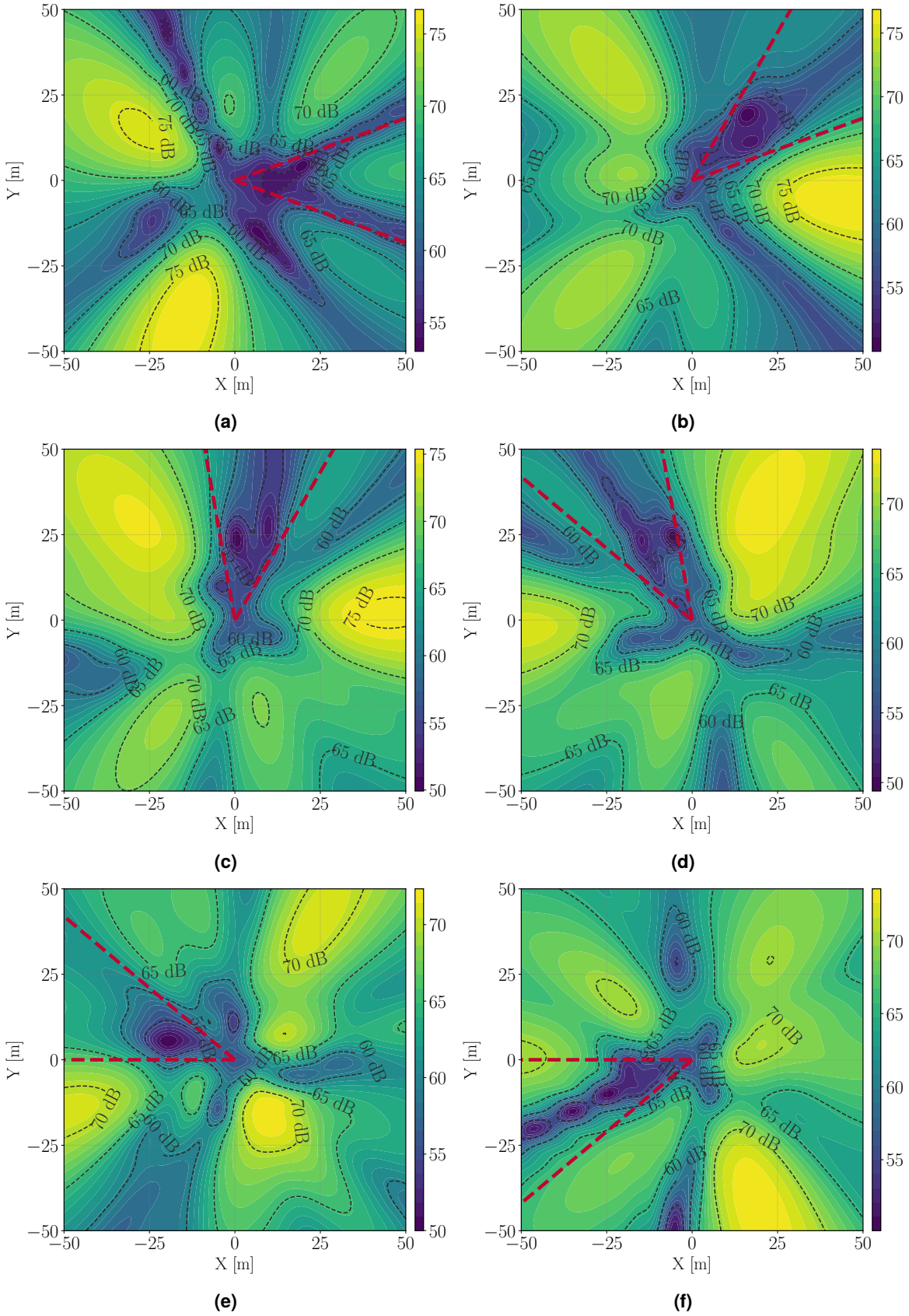

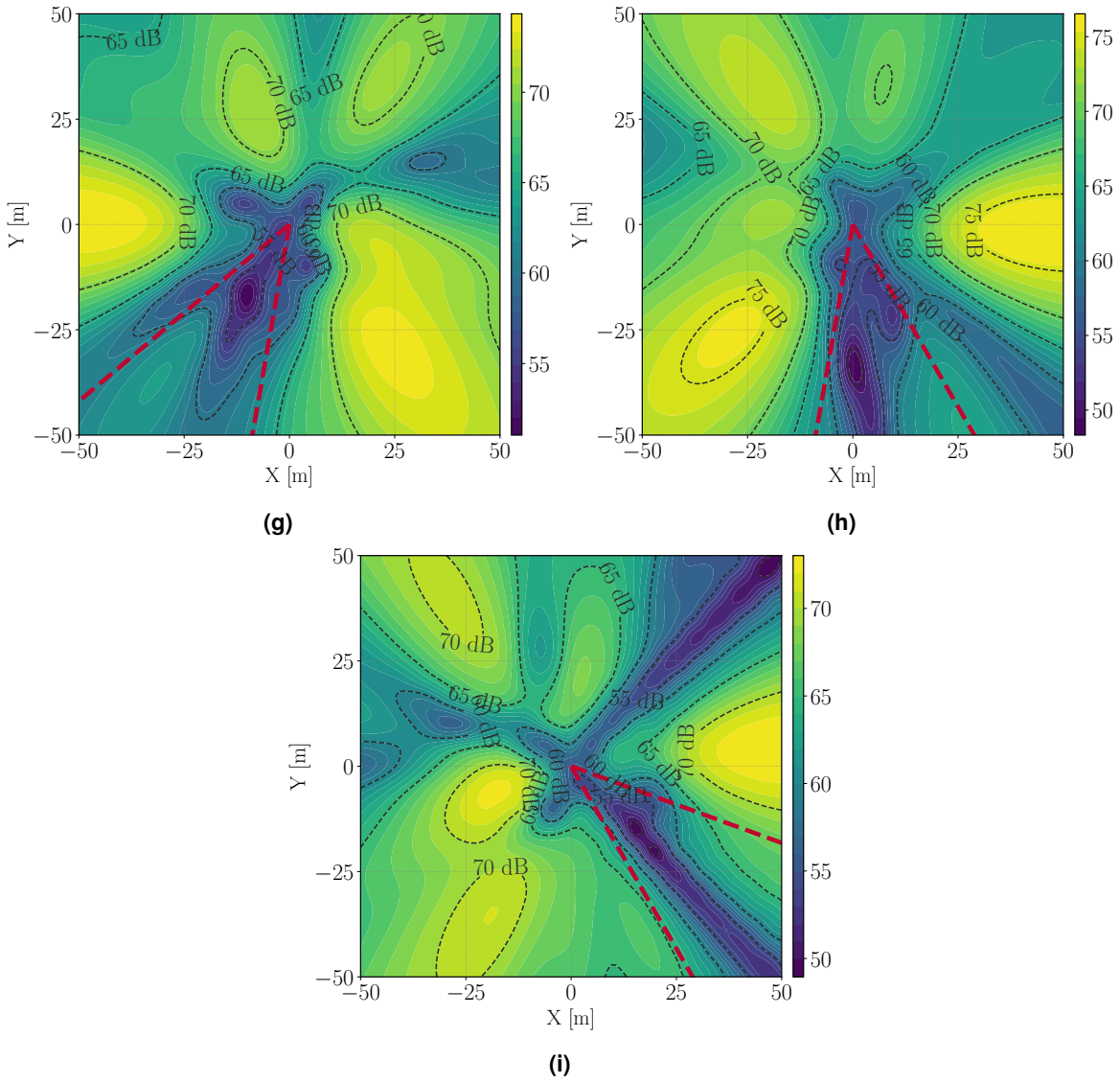


**Figure B.3.** Analytical Tool optimization results over the plane for the Octarotor configuration, presented for all sections.

# C | Code

## C.1 Analytical Tool

```
import numpy as np
import matplotlib.pyplot as plt
from matplotlib.patches import Wedge
from numba import jit, config, prange
from joblib import Parallel, delayed

# Optimize Numba for multi-threading
config.THREADING_LAYER = 'threadsafe'

# Physical constants
RHO = 1.19191  # Air density (kg/m^3)
C = 344.986    # Speed of sound (m/s)
OMEGA_0 = 110  # Angular velocity (rad/s)
EQ_MODEL = 'delfs'  # Choose 'delfs' or 'gur'

# Acoustic model parameters
if EQ_MODEL == 'delfs':
    Q0 = 0.45  # Monopole source strength (m^3/s)
elif EQ_MODEL == 'gur':
    Q0 = 0.0016205  # Blade element volume (m^3)
F0 = np.array([0, 0, 4.13])  # Dipole force (N)

# Rotor configuration
N_ROTORS = 4
PHASES = np.array([0, 90, 0, 90]) * np.pi / 180
OMEGA = np.array([1 if i % 2 == 0 else -1 for i in range(N_ROTORS)]) * OMEGA_0
D_R = 3.5 * (N_ROTORS / 6)
ANG = 2 * np.pi / N_ROTORS
ANG_OFF = np.pi / N_ROTORS
ROTS = np.array([[D_R * np.cos(-ANG_OFF - ANG * n), D_R * np.sin(-ANG_OFF - ANG *
 ↪  n), 0] for n in range(N_ROTORS)])
R_ROTOR = 1.092
```

```
R_SPH = 14.5
THETA_B = np.array([0, np.pi])

# Microphone grid (hemisphere)
THETA = np.arange(-90, 0, 1) * np.pi / 180
RES_SPH = len(THETA)
PHI = np.linspace(0, 2 * np.pi, RES_SPH)
THETA_GRID, PHI_GRID = np.meshgrid(THETA, PHI)
X = R_SPH * np.cos(THETA_GRID) * np.cos(PHI_GRID)
Y = R_SPH * np.cos(THETA_GRID) * np.sin(PHI_GRID)
Z = R_SPH * np.sin(THETA_GRID)

# Time vector (Receiving Time)
T = 2 * np.pi / OMEGA_0
NR = 2
T_START = (R_SPH + R_ROTOR + ROTS[0][0]) / C
T_END = NR * T + T_START
T_POINTS = 24 * NR
T = np.linspace(T_START, T_END, T_POINTS)

# Acoustic model functions
@jit(nopython=True)
def blade_pressure(t_array, theta_s, offset, phase, omega, q0, f0, x, y, z,
↪   eq_model):
    """Compute pressure contribution from a single blade with emission time
    ↪  correction."""
    pm = np.zeros(len(t_array))
    pd = np.zeros(len(t_array))
    tau_0 = 0.0

    for j in range(len(t_array)):
        t_i = t_array[j]
        k = 0
        tol = 1e-3
        x_init = R_ROTOR * np.cos(theta_s + omega * tau_0 + phase)
        y_init = R_ROTOR * np.sin(theta_s + omega * tau_0 + phase)
        r_vec_init = np.array([x - x_init - offset[0], y - y_init - offset[1], z -
        ↪  offset[2]])
        norm_r_init = np.sqrt(r_vec_init[0]**2 + r_vec_init[1]**2 +
        ↪  r_vec_init[2]**2)
        if norm_r_init == 0:
            continue
        d = (tau_0 - t_i + norm_r_init / C) / (
```

```
    1 + (1 / (norm_r_init * C)) * (
        -R_ROTOR * omega * np.sin(theta_s + omega * tau_0 + phase) +
        R_ROTOR * omega * np.cos(theta_s + omega * tau_0 + phase)
    )
)
tau = tau_0 - d

while np.abs(tau - tau_0) >= tol * np.abs(tau):
    tau_0 = tau
    x_it = R_ROTOR * np.cos(theta_s + omega * tau_0 + phase)
    y_it = R_ROTOR * np.sin(theta_s + omega * tau_0 + phase)
    r_vec_it = np.array([x - x_it - offset[0], y - y_it - offset[1], z -
    ↪  offset[2]])
    norm_r_it = np.sqrt(r_vec_it[0]**2 + r_vec_it[1]**2 + r_vec_it[2]**2)
    if norm_r_it == 0:
        break
    d = (tau_0 - t_i + norm_r_it / C) / (
        1 + (1 / (norm_r_it * C)) * (
            -R_ROTOR * omega * np.sin(theta_s + omega * tau_0 + phase) +
            R_ROTOR * omega * np.cos(theta_s + omega * tau_0 + phase)
        )
    )
    tau = tau_0 - d
    k += 1
    if k > 100:
        break

x_blade = R_ROTOR * np.cos(theta_s + omega * tau + phase)
y_blade = R_ROTOR * np.sin(theta_s + omega * tau + phase)
z_blade = 0
r_vec = np.array([x - x_blade - offset[0], y - y_blade - offset[1], z -
↪  z_blade - offset[2]])
r_norm = np.sqrt(r_vec[0]**2 + r_vec[1]**2 + r_vec[2]**2)
if r_norm == 0:
    pm[j] = 0.0
    pd[j] = 0.0
    continue
r_vers = r_vec / r_norm

v_x = -R_ROTOR * omega * np.sin(theta_s + omega * tau + phase)
v_y = R_ROTOR * omega * np.cos(theta_s + omega * tau + phase)
v_source = np.array([v_x, v_y, 0])
m_q = v_source / C
```

```
a_x = -R_ROTOR * (omega**2) * np.cos(theta_s + omega * tau + phase)
a_y = -R_ROTOR * (omega**2) * np.sin(theta_s + omega * tau + phase)
a_source = np.array([a_x, a_y, 0])
m_q_acc = a_source / C

j_x = R_ROTOR * (omega**3) * np.sin(theta_s + omega * tau + phase)
j_y = -R_ROTOR * (omega**3) * np.cos(theta_s + omega * tau + phase)
j_source = np.array([j_x, j_y, 0])
m_q_jerk = j_source / C

m_q_r = np.dot(m_q, r_vers)
m_q_acc_r = np.dot(m_q_acc, r_vers)
m_q_jerk_r = np.dot(m_q_jerk, r_vers)

if eq_model == 'delfs':
    ppm = (1 / (4 * np.pi)) * (
        (q0 * m_q_acc_r / (1 - m_q_r)) / (r_norm * (1 - m_q_r)**2) +
        C * q0 * (m_q_r - np.dot(m_q, m_q)) / (r_norm**2 * (1 - m_q_r)**3)
    )
    ppd = (1 / (4 * np.pi)) * (
        (np.dot(f0, r_vers) * m_q_acc_r / (1 - m_q_r)) / (C * r_norm * (1 -
        ↪  m_q_r)**2) +
        (np.dot(-f0, m_q) + (1 - np.dot(m_q, m_q)) * np.dot(f0, r_vers) / (1
        ↪  - m_q_r)) / (r_norm**2 * (1 - m_q_r)**2)
    )
else:  # 'gur'
    ppm = (RHO / (4 * np.pi)) * (
        (q0 / (r_norm * (1 - m_q_r)**3)) * (
            m_q_jerk_r / (1 - m_q_r) +
            3 * (m_q_acc_r / (1 - m_q_r))**2 +
            (m_q_acc_r * C * (1 + 2 * m_q_r)) / (r_norm * (1 - m_q_r)) +
            2 * ((m_q_r * C) / r_norm)**2
        )
    )
    ppd = (1 / (4 * np.pi)) * (
        (np.dot(f0, r_vers) * (m_q_acc_r / (1 - m_q_r))) / (r_norm * C * (1 -
        ↪  m_q_r)**2) +
        (np.dot(f0, r_vers) * ((1 - np.dot(m_q, m_q)) / (1 - m_q_r)) -
        ↪  np.dot(f0, m_q)) / (r_norm**2 * (1 - m_q_r)**2)
    )
pm[j] = ppm
pd[j] = ppd
```

```
    return pm + pd

@jit(nopython=True, parallel=True)
def rotor_pressure(t_array, offset, phase, omega, q0, f0, x, y, z, theta_b,
↪   eq_model):
    """Sum pressure contributions from all blades in a rotor with
    ↪  parallelization."""
    p_tot = np.zeros(len(t_array))
    for i in prange(len(theta_b)):
        p_tot += blade_pressure(t_array, theta_b[i], offset, phase, omega, q0, f0,
        ↪  x, y, z, eq_model)
    return p_tot

@jit(nopython=True, parallel=True)
def compute_pressure(t_array, rots, phases, omega, q0, f0, x, y, z, theta_b,
↪   eq_model):
    """Compute total pressure at a point over time from all rotors with
    ↪  parallelization."""
    p_tot = np.zeros(len(t_array))
    for i in prange(len(rots)):
        p_tot += rotor_pressure(t_array, rots[i], phases[i], omega[i], q0, f0, x, y,
        ↪  z, theta_b, eq_model)
    return p_tot

@jit(nopython=True)
def compute_spl(p):
    """Compute Sound Pressure Level (SPL) from pressure time series."""
    p_cycle = p[-24:]
    rms = np.sqrt(np.mean(p_cycle**2))
    return 20 * np.log10(rms / 2e-5) if rms > 0 else 0.0

# --- Parallelized Pressure Field Computation ---
def compute_pressure_field_parallel(X, Y, Z, t, rots, phases, omega, q0, f0,
↪   theta_b, eq_model):
    """Compute SPL across the grid"""
    def process_point(i, k):
        p = compute_pressure(t, rots, phases, omega, q0, f0, X[i, k], Y[i, k], Z[i,
        ↪  k], theta_b, eq_model)
        return compute_spl(p)

    results = Parallel(n_jobs=-1)(
        delayed(process_point)(i, k) for i in range(RES_SPH) for k in range(RES_SPH)
```

```
    )
    return np.array(results).reshape(RES_SPH, RES_SPH)

# --- Compute SPL ---
DB_TOT = compute_pressure_field_parallel(X, Y, Z, T, ROTS, PHASES, OMEGA, Q0, F0,
 ↪  THETA_B, EQ_MODEL)
```

## C.2 Genetic Algorithm

```python
import numpy as np
from ypstruct import structure

def run(problem, params):

    # Problem Information
    costfunc = problem.costfunc
    nvar = problem.nvar
    varmin = problem.varmin
    varmax = problem.varmax

    # Parameters
    maxit = params.maxit
    npop = params.npop
    beta = params.beta
    pc = params.pc
    nc = int(np.round(pc*npop/2)*2)
    gamma = params.gamma
    mu = params.mu
    sigma = params.sigma

    # Empty Individual Template
    empty_individual = structure()
    empty_individual.position = None
    empty_individual.cost = None

    # Best Solution Ever Found
    bestsol = empty_individual.deepcopy()
    bestsol.cost = np.inf

    # Initialize Population
    pop = empty_individual.repeat(npop)
    for i in range(npop):
        pop[i].position = np.random.uniform(varmin, varmax, nvar)
        pop[i].cost = costfunc(pop[i].position)
        if pop[i].cost < bestsol.cost:
            bestsol = pop[i].deepcopy()

    # Best Cost of Iterations
    bestcost = np.empty(maxit)
```

```
# Main Loop
for it in range(maxit):
    costs = np.array([x.cost for x in pop])
    avg_cost = np.mean(costs)
    if avg_cost != 0:
        costs = costs/avg_cost
    probs = np.exp(-beta*costs)

    popc = []
    for _ in range(nc//2):

        # Select Parents
        #q = np.random.permutation(npop)
        #p1 = pop[q[0]]
        #p2 = pop[q[1]]

        # Perform Roulette Wheel Selection
        p1 = pop[roulette_wheel_selection(probs)]
        p2 = pop[roulette_wheel_selection(probs)]

        # Perform Crossover
        c1, c2 = crossover(p1, p2, gamma)

        # Perform Mutation
        c1 = mutate(c1, mu, sigma)
        c2 = mutate(c2, mu, sigma)

        # Apply Bounds
        apply_bound(c1, varmin, varmax)
        apply_bound(c2, varmin, varmax)

        # Evaluate First Offspring
        c1.cost = costfunc(c1.position)
        if c1.cost < bestsol.cost:
            bestsol = c1.deepcopy()

        # Evaluate Second Offspring
        c2.cost = costfunc(c2.position)
        if c2.cost < bestsol.cost:
            bestsol = c2.deepcopy()

        # Add Offsprings to popc
        popc.append(c1)
```

```
            popc.append(c2)


        # Merge, Sort and Select
        pop += popc
        pop = sorted(pop, key=lambda x: x.cost)
        pop = pop[0:npop]

        # Store Best Cost
        bestcost[it] = bestsol.cost

        # Show Iteration Information
        print(f"Iteration {it}: Best Cost = {f'{bestcost[it]:.4f}':<10} Best Sol =
        ↪  {np.intc(bestsol.position)}")

    # Output
    out = structure()
    out.pop = pop
    out.bestsol = bestsol
    out.bestcost = bestcost
    return out

def crossover(p1, p2, gamma=0.1):
    c1 = p1.deepcopy()
    c2 = p1.deepcopy()
    alpha = np.random.uniform(-gamma, 1+gamma, *c1.position.shape)
    c1.position = alpha*p1.position + (1-alpha)*p2.position
    c2.position = alpha*p2.position + (1-alpha)*p1.position
    return c1, c2

def mutate(x, mu, sigma):
    y = x.deepcopy()
    flag = np.random.rand(*x.position.shape) <= mu
    ind = np.argwhere(flag)
    y.position[ind] += sigma*np.random.randn(*ind.shape)
    return y

def apply_bound(x, varmin, varmax):
    x.position = np.maximum(x.position, varmin)
    x.position = np.minimum(x.position, varmax)

def roulette_wheel_selection(p):
    c = np.cumsum(p)
```

```
r = sum(p)*np.random.rand()
ind = np.argwhere(r <= c)
return ind[0][0]
```